Imperial College London
Department of Mechanical Engineering

Probabilistic Approach to Structural Integrity Assessment of Fatigue Damage using Permanently Installed Monitoring Systems

by

Leung, Siu Hey Michael

A thesis submitted to Imperial College London for the degree of
Doctor of Philosophy

Non-destructive Evaluation Group
Department of Mechanical Engineering
Imperial College London
London SW7 2AZ

Oct 2020

Declaration of originality

The work contained in this thesis is entirely my own and completed under the supervision of Dr. Joseph Corcoran and Prof. Peter Cawley. Appropriate references are given wherever the work of others has been used.

Leung, Siu Hey Michael
Oct 2020

Copyright declaration

Abstract

This thesis aims to develop strategies for integrating frequent onload data obtained from permanently installed monitoring systems with probabilistic structural integrity methods in order to produce real-time, uncertainty-quantified diagnostics and prognostics for fatigue damage. The proposed strategy is broadly divided into two phases: defect detection, and defect growth monitoring.

For the defect detection phase, a framework for evaluating the detection capabilities of PIMS is first proposed. This is essential to qualifying PIMS for industrial applications, and forms the basis of quantifying its value for structural integrity assessment. The framework is then utilised to address the well-recognised compromise between area coverage and sensitivity of PIMS. By combining information on the spatial sensitivity of PIMS and the spatial uncertainty of defect location, the detection capabilities of specific combinations of monitoring systems and components can be quantitatively compared.

A novel approach to incorporate measurements from PIMS into structural integrity assessment is subsequently proposed. The ability of PIMS to recursively eliminate the possibility of there being substantial damage in the monitored component is demonstrated, which proves to be an effective way of maintaining confidence in its structural integrity. This framework will therefore help promote the adoption of PIMS for damage detection in suitable engineering applications.

For the defect growth monitoring phase, the ability of PIMS to produce accurate rate measurements is exploited to perform remnant life predictions using the Failure Forecast Method (FFM). A statistical analysis comparing the conventional inspection-based approach to the FFM approach is performed, demonstrating the ability of the FFM approach to estimate more accurately the remnant life of the monitored component. A novel method for using the FFM under non-constant amplitude loading conditions is also developed and validated. This enables the use of the FFM in more complex loading conditions, thereby advancing its potential uses in real-life applications.

Acknowledgements

I am grateful for the amount of support and guidance that I have received throughout this research degree. First and foremost, I would have to thank my supervisors, Dr. Joseph Corcoran and Prof. Peter Cawley, for the patience and effort they have dedicated to guide me through this research degree; what is achieved here would never have been possible without their support and encouragement.

I would like to thank Prof. Michael Todd for his contribution in developing the probabilistic models for the Failure Forecast Method, as well as his advices on the use of particle filtering methods.

I would like to thank Dr. Catrin Davies for her help in conducting fatigue experiments, her advices on the topic of fatigue and fracture mechanics, and also her support since my undergraduate studies as a personal tutor.

I would like to thank Prof. Peter Nagy for his help with using the potential drop monitoring system, which eventually led to new discoveries and the publication of a journal paper.

I would like to thank Dr. Pouyan Khalili for his contribution in developing the finite element simulations for the ultrasonic sensor.

It has been a pleasure to work within the Imperial College Non-Destructive Evaluation Research Group. I am thankful for the friendly and supportive vibe of the research group that everyone has positively contributed to.

I would also like to thank the Engineering and Physical Sciences Research Council for funding this research through the UK Research Centre in Nondestructive Evaluation. In particular, I would like to thank Prof. Keith Newton for regularly keeping in touch with me and other students to make sure things are going smoothly for us.

Finally, I would like to thank my parents Alec Leung and Dorothy Yu, brothers and sisters in Chinese Church in London, and Sally Lee for being loving and supportive throughout the years of my studies.

"If I have the gift of prophecy and can fathom all mysteries and all knowledge,
and if I have a faith that can move mountains, but do not have love, I am nothing."
1 Corinthians 13:2, NIV

Table of Contents

1 Introduction

1.1 Background and motivation of research

Fatigue damage is one of the leading causes of failure in engineering structures [1], [2]. Components subjected to repeated loading are prone to the initiation and propagation of fatigue cracks, which can potentially lead to catastrophic failures that are costly and hazardous to repair [3]–[5]. Thus, assessing and managing the structural integrity of such components in real-life engineering applications is of great importance.

A significant amount of research is conducted in attempt to understand and predict the accumulation of fatigue damage. This ranges from fundamental understanding of the physical phenomenon for various materials [6], [7] to the development of empirical models and computational simulations that are used for the analysis of complex geometries and loading conditions [8], [9]. Despite such efforts, accurately predicting the fatigue life of an in-service engineering component still remains a difficult task. The progression of fatigue damage is strongly dependent on microstructural imperfections, loading conditions and environmental factors which are often not precisely known in advance. This results in significant uncertainties when predicting the progression of fatigue damage, making it very challenging to accurately estimate the fatigue life of a specific component.

Conventionally, conservative estimates have been used to overcome uncertainties in fatigue damage progression when managing engineering structures. In order to provide confidence that the possibility of failure is sufficiently low, conservatism in input parameters based on standardised factors of safety are used. Such conservatism in input parameters aggregates and ultimately results in largely conservative estimates in the life estimate. Standards and procedures on how to obtain sufficiently conservative estimates has been well established in multiple industries [10]–[12].

As industries strive to continually improve and optimise the life-cycle management of engineering structures, moving towards probabilistic approaches in structural integrity assessment becomes increasingly necessary. While conservative estimates provide confidence in structural integrity, the level of conservatism is based on engineering judgement, therefore making the level of confidence in the estimate difficult to quantify. In comparison, the use of probabilistic methods makes it possible to quantify the margins of safety and thus confidence in the estimates produced, which in turn would allow for better-informed decisions in the management of engineering structures. Consequently, research and developments in implementing probabilistic approaches in structural integrity assessment and life estimates has become increasingly prevalent [13]–[15].

In addition to initial estimates of fatigue life, regular in-service inspections using non-destructive evaluation (NDE) techniques are also typically performed for critical engineering components in order to be confident of its structural integrity. Results from an inspection can be used to assess and update the prior estimates of the structural integrity of the component. This would ultimately inform the decision on whether any remedial actions are required and timing of the next inspection. Procedures of doing so in a consistent and thorough manner have been developed worldwide and in use for multiple engineering applications [16]–[18].

With advances in technology, it is becoming increasingly viable and of commercial interest to use permanently installed monitoring systems (PIMS) to monitor engineering components in real-time; this is commonly referred to as structural health monitoring (SHM). Near-continuous data collected by PIMS has the potential to provide information on the damage state of the monitored component while it is in operation. Notably, incorporating SHM has the potential benefit of reducing the need of in-service inspections while assuring the structural integrity of the monitored component to the same confidence level. This is especially valuable for components that are difficult and hazardous to access and inspect.

In order to implement PIMS for detecting and monitoring fatigue damage in real-life applications, frameworks for interpreting data collected from PIMS for use in probabilistic structural integrity assessment needs to be developed. Given the fundamental differences between data obtained from in-service inspections and data obtained in real-time from PIMS, there are both great challenges and promising opportunities in using PIMS for localised defect detection and monitoring to provide better-informed estimates in structural integrity and remaining life.

1.2 Project aims and thesis outline

The overall aim of this research project is to develop strategies for integrating frequent onload data obtained from PIMS with probabilistic structural integrity methods in order to produce real-time, uncertainty-quantified diagnostics and prognostics for fatigue damage. This research will seek to investigate the use of PIMS for localised defect monitoring in two main phases of fatigue damage. First is the use of PIMS for detecting the initiation of a macroscopic defect; second is the use of PIMS to track and monitor the growth of an identified defect. The frameworks and methods developed in this research can be deployed in a wide range of applications to provide valuable understanding on the feasibility and quantified benefits of using PIMS for localised defect monitoring from the perspective of managing the lifecycle of engineering components.

This thesis will be structured as follows:

In Chapter 2, the background theory of the fundamental mechanisms of fatigue damage is introduced, followed by a review of engineering approaches to modelling and quantifying fatigue damage. Subsequently, a review of the current state-of-the-art in non-destructive techniques that are suitable for SHM is provided.

Chapter 3 proposes a framework to quantify the detection capabilities of PIMS. The chapter begins by describing the theory of quantifying the detection capability of NDE inspection techniques. The differences in evaluating the uncertainty of monitoring results from PIMS as opposed to NDE inspection will then be discussed. A hypothetical example based on computational simulations is used to demonstrate the proposed framework. This would form the foundations of quantifying the benefits of using PIMS for probabilistic structural integrity assessments.

Having established a framework for quantifying the detection capabilities of PIMS, Chapter 4 then uses the framework to address the well-recognised compromise between area coverage and sensitivity for PIMS, evaluating the probability of detection of PIMS with respect to the spatial uncertainty in defect initiation. Example components with varying degree of confidence in defect location are to be monitored with PIMS with varying degree of area coverage and sensitivity. The results for each sensor-component combination are then compared using quantified performance parameters, thus demonstrating the value of the framework in optimising the design of PIMS and evaluating the efficacy of using PIMS for life-cycle management.

Chapter 5 proceeds to develop a framework for quantifying the value of PIMS when integrated in structural integrity assessment from the point of view of managing the life cycle of a component. Established mathematical tools for probabilistic analysis in structural integrity assessment is first described. A framework for implementing data from PIMS for structural integrity assessment is then proposed. Subsequently, a comparison between managing the life cycle of a component with and without PIMS is made using a simulated example.

With the use of PIMS to detect an initiated defect considered, Chapter 6 proceeds to evaluate the potential of using PIMS to monitor and track the growth of an identified defect. A recently developed approach using rate-based measurements to perform remnant life predictions is first described [19]. This approach will then subsequently be expanded for more complex fatigue loading conditions. To demonstrate the feasibility and benefits of using a rate-based approach to perform remnant life predictions, a statistical analysis based on laboratory experiments is developed and performed. A comparison with the conventional inspection-based approach will also be made.

Finally, Chapter 7 provides the conclusion and summary of main contributions of this research, together with suggestions for future work.

2 Literature review

This chapter provides a theoretical background and literature review on the fields of study that are relevant to the research project. The chapter will be divided into two sections, discussing the background theory of fatigue damage and the state-of-the-art of SHM technologies for monitoring fatigue damage.

2.1 Theory of fatigue damage

As early as the 19th century, it has been observed that materials fail under repeated loading, even if the loading results in stresses below its yield strength [20]. Due to its great implications on engineering design, the phenomenon of fatigue damage has been comprehensively studied across all phases from initiation of microscopic damage to the propagation of macroscopic cracks. This section describes the fundamental mechanisms of metal fatigue damage and the different engineering approaches to evaluating and managing the progression of fatigue damage.

2.1.1 Mechanisms of metal fatigue

As summarised from [7], [21], fatigue damage progression can be divided into 4 phases as shown in Figure 2.1. These phases will be discussed in the following subsections. Note that Phase 3 and 4 are discussed before Phase 2 as it is simpler to introducing key concepts in Phase 3 and 4 before explaining Phase 2.

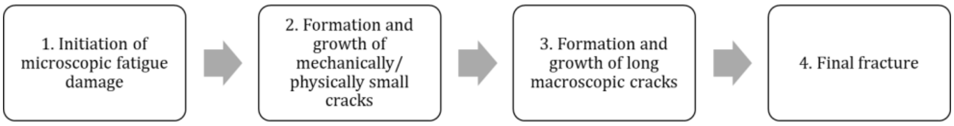

Figure 2.1 Flowchart summarising the progression of fatigue damage.

2.1.1.1 Phase 1: Initiation of microscopic fatigue damage

The initiation of microstructural damage and cracks is a complex problem with great dependence on the microstructure of the specific material of interest. Detailed description and review on the current state-of-the-art can be found in [21], [22]; a brief description sufficient for the scope of this research is given here.

Fatigue damage originates from the accumulation of permanent microscopic changes as a component is repeatedly loaded and unloaded. During the initial loading cycles, surface grains may plastically deform locally even when subjected to nominally elastic loads. This type of deformation is known as microplasticity and is caused by slipping within the grains of the material. Slipping is the movement of dislocations along crystallographic planes of a grain [23]. Slipping can only occur at defined slip planes of a grain, hence it occur favourably at grains where the orientation of grains aligns with the plane of maximum shear stress [24]. Slipping via cyclic loading results in extrusions and intrusions as shown in Figure 2.2. This characteristic form of dislocation structure, known as persistent slip bands, then result in stress concentrators at the surface of the material and therefore become preferential sites for microscopic cracks to form; an example image of this taken with a scanning electron microscope is shown in Figure 2.3. With successive cyclic loading, these microscopic cracks will then continue to coalesce with persistent slip bands formed at neighbouring grains and grow along the grain boundaries of the material.

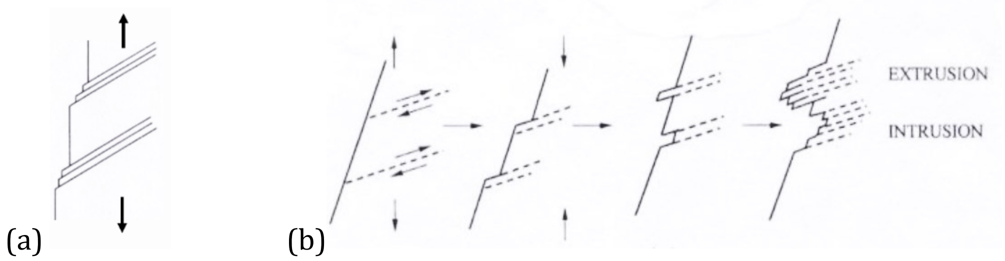

Figure 2.2 Formation of slip lines with (a) monotonic loading, and (b) cyclic loading [23]

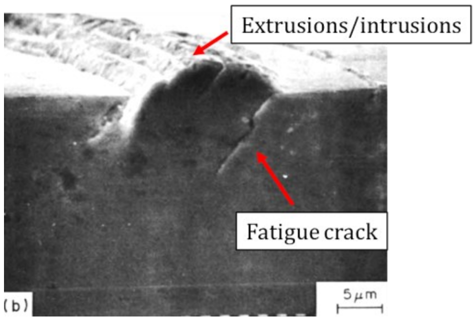

Figure 2.3 Scanning electron microscope image of an initiated fatigue crack from persistent slip bands. Image modified from [25].

2.1.1.2 Phase 3 and 4: Formation and growth of long macroscopic cracks and final fracture

As microscopic defects continue to grow, they eventually become macroscopic in size. At this phase of fatigue damage, global stress-strain field analyses can now be used to evaluate crack growth behaviour. There are multiple modes of loading that will result in crack growth, namely opening (Mode I), shearing (Mode II) and tearing (Mode III) mode. These different modes of crack growth are illustrated in Figure 2.4. The discussion hereon will focus on the most commonly considered Mode I loading.

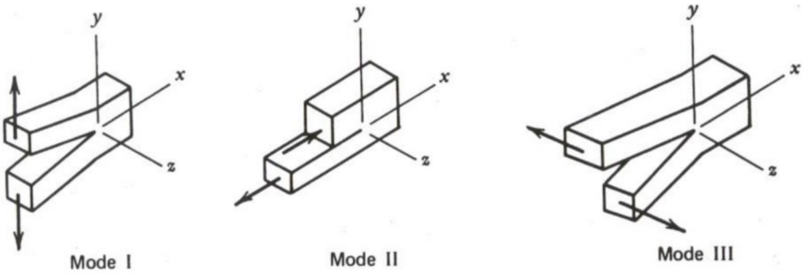

Figure 2.4 Schematic of the different modes of loading resulting in crack growth. [23]

At the stage of long crack growth, crack growth characteristics can simply be described by the stress intensity factor range, ΔK, and maximum stress intensity factor, K_{max}, assuming linear elastic conditions. Stress intensity factor, K is defined as,

$$K = YS\sqrt{a} \quad \text{Eq. 2.1}$$

$S =$ Loading stress perpendicular to direction of crack growth
$Y =$ Geometry factor
$a =$ Crack length

It has been proposed that any combination of loading, crack length and geometry for the same material that results in the same ΔK and K_{max} value would have identical crack growth behaviour. This is known as the similitude hypothesis [26] and it is widely regarded to hold true in the phase of long crack growth.

The phase of long fatigue crack growth is generally divided into three stages as illustrated in Figure 2.5. The differentiation between Stage I and Stage II crack growth is governed by the cyclic plastic zone size (i.e. the volume of the material near the crack tip that is plastically deformed under cyclic loading). The difference in plastic zone size would result in different microscopic failure modes that result in crack growth. Stage I crack growth is when the resulting cyclic plastic zone is smaller than the grain size, resulting in single-shear crack growth as shown in Figure 2.6 (a). This gives a serrated crack surface as crack growth would be parallel to the slip plane of the grain ahead of the crack tip.

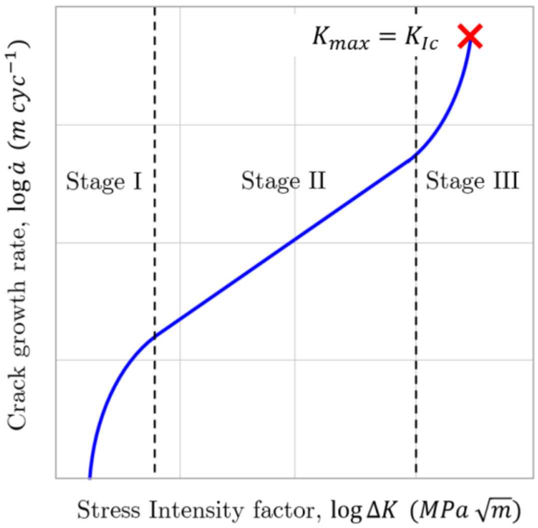

Figure 2.5 Plot of the different stages of linear elastic long fatigue crack growth.

Stage II crack growth is when the resulting cyclic plastic zone is larger than the grain diameter, resulting in duplex slip crack growth where slipping occurs simultaneously across multiple grains, resulting in transgranular crack growth; this is shown in Figure 2.6 (b). Here, crack growth is not governed by the orientation of the grain ahead of the crack tip, hence it grows perpendicular to the direction of applied load. Stage II crack growth can be described by the well-known Paris' Law, as discussed later.

Stage III crack growth is generally of limited interest; the portion of fatigue life spent in this stage of fatigue crack propagation is negligibly small [27]. Ultimately, the size of the fatigue crack increases very rapidly and reaches a point where the component can no longer withstand the loading, reaching the fourth and final stage of defect progression. In engineering applications, failure assessment diagrams (FAD) as discussed later in Section 2.1.2.4 is used to evaluate the final crack length and mode of failure.

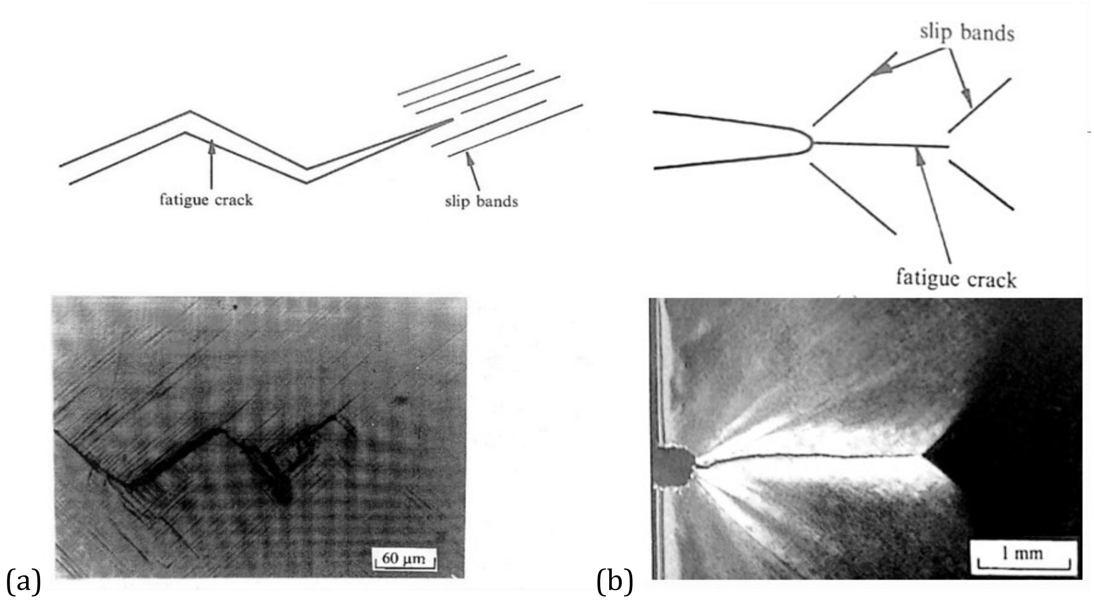

Figure 2.6 Schematic and example of Stage I (left) and Stage II (right) long crack growth [21]. Note the difference in length scales of the two images.

2.1.1.3 Phase 2: Formation and growth of mechanically/physically small cracks

The formation and growth of mechanically/physically small cracks can be seen as a transition between microscopic crack growth and long macroscopic crack growth. While global stress-strain field analyses can still be used to evaluate crack growth at this phase, the similitude hypothesis does not hold. This breakdown of the similitude hypothesis is often attributed to the effect of crack closure, as briefly discussed below; a more detailed review on the topic can be found in [28].

Crack closure is the phenomenon which the crack surfaces remain in contact despite the presence of far-field tensile loading. In the absence of extreme environment effects (e.g. high temperature, presence of corrosive fluids etc.), the most prominent effects are plasticity-induced and roughness-induced crack closure. Plasticity-induced crack closure is a result of plastic deformation of material near the surface of a fatigue crack. As fatigue cracks propagate, a wake of plastic-deformed material is formed as illustrated in Figure 2.7. Depending on the geometry, this deformation can result in the crack surfaces coming into contact before it is fully unloaded, thus reducing the effective tensile loading range at the crack tip. The significance of this effect will also depend on the loading ratio experienced by the component; the effect is much less pronounced when the component remains in tension throughout the loading cycle.

Roughness-induced crack closure originates from the fact that for lower stress intensity crack growth regimes, crack growth results in serrated crack surfaces as detailed in Section 2.1.1.2. Despite under nominally Mode I loading, other modes of loading as defined in the previous section may be present locally near the crack tip. This results in a mismatch between the asperities of the crack surface, which in turn enhances fatigue crack closure [21]. An illustration of this is shown in Figure 2.8.

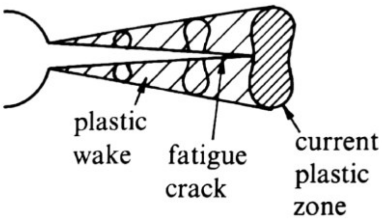

Figure 2.7 Schematic of the plastic zone ahead of the crack tip, and the plastic wake developed due to previous loading cycles. [21]

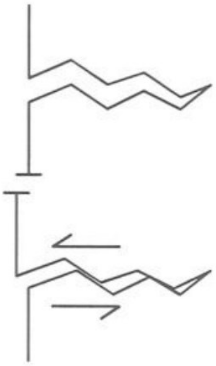

Figure 2.8 Schematic of the mismatch of fracture surface asperity, resulting in crack closure. [29]

For the above crack closure effects described to be apparent, the crack length would have to be sufficiently long to contain a fully developed plastic wake and sufficient crack surfaces. This means that there are smaller resistive forces to crack growth for cracks that are smaller in size. Since the propagation of a fatigue crack is a balance between the driving (i.e. mechanical load) and resistive (i.e. crack closure) forces, small cracks can grow at lower loadings or at greater growth rates for equal loadings compared to long cracks.

Consequently, conventional long crack growth laws cannot be used to predict crack growth behaviour of short cracks, or at least corrections would have to be made. It is therefore important to acknowledge that short cracks can propagate at lower loads, and that it would often be quicker than what is predicted from conventional long crack growth analysis. This can lead to non-conservative estimations, something that is undesirable for engineering applications.

As this mechanically/physically small crack continue to propagate with more loading cycles, the effect of crack closure plateaus and eventually becomes independent of crack length. This is when the concept of similitude hypothesis holds, marking the end of Phase 2 and the beginning of Phase 3 as discussed earlier in Section 2.1.1.2.

2.1.2 Engineering approach to evaluating fatigue damage

From an engineering perspective, it is of great importance to quantitatively correlate the extent of fatigue loading (i.e. stress or strain amplitude) to the number of loading cycles before different phases of fatigue damage as defined earlier is reached. Overall, the total number of loading cycles to failure, N_f, is usually divided into two phases [30],

$$N_f = N_i + N_p \tag{Eq. 2.2}$$

where N_i is the number of cycles before a macroscopic fatigue crack initiates, and N_p is the number of cycles before the initiated crack propagates through the component, resulting in final failure. Note that the definition of an "initiated defect" is ambiguous and has significantly different interpretations across research communities. From an engineering and NDE point of view, this is typically defined as a defect that has reached a detectable size, hence its definition would also depend on the detection capabilities of the NDE technique used.

Depending on the extent of fatigue loading, the proportions of different phases of fatigue damage can vary significantly. For higher loading applications, also known as low cycle fatigue, few cycles are required before a microscopic and subsequently macroscopic crack is initiated, hence its fatigue life is dominated by fatigue crack propagation. On the other hand, for lower loading applications, also known as high cycle fatigue, fatigue life is instead dominated by the initiation of a macroscopic crack. Upwards of 99% of the fatigue life at lower loading applications can be spent at the initiation phase [31].

Given the different proportions of damage phases, there are two main approaches to managing the progression of fatigue damage, namely the safe-life approach and the damage tolerant approach, are typically used. The following is a review of the two approaches.

2.1.2.1 Safe-life approach to fatigue damage

The overall concept of the safe-life (or total-life) approach is to ensure that fatigue cracks would not initiate and propagate to cause catastrophic failure after experiencing a predefined number of loading cycles. The approach assumes that components are nominally defect-free prior to service, thus its resistance to fatigue crack initiation and propagation can be estimated with laboratory tests using nominally defect-free specimens of the same material under representative operating conditions [21].

A further simplification that can be made for certain materials such as steel and titanium would be to design for infinite fatigue life. It is generally accepted that for practical purposes, there exists a limiting loading extent at which a component made of these materials will in theory have infinite fatigue life [32]. While earlier phases of damage may still be reached, there is insufficient driving force for these defects to ultimately cause fracture. This material-dependent loading limit is known as the fatigue limit. A component that will not experience loading amplitudes greater than its fatigue limit is therefore considered to have infinite fatigue life.

Basquin first proposed the relationship between the cyclic load stress amplitude, S_a, and the cycles to failure, N_f for elastic loading as plotted in Figure 2.9 and expressed as [33],

$$S_a = \frac{\Delta S}{2} = S_f'\left(2N_f\right)^b \qquad \text{Eq. 2.3}$$

ΔS = Stress range

S_f' = Fatigue strength coefficient (approximately the fracture strength in a monotonic tensile stress)

b = Fatigue strength exponent

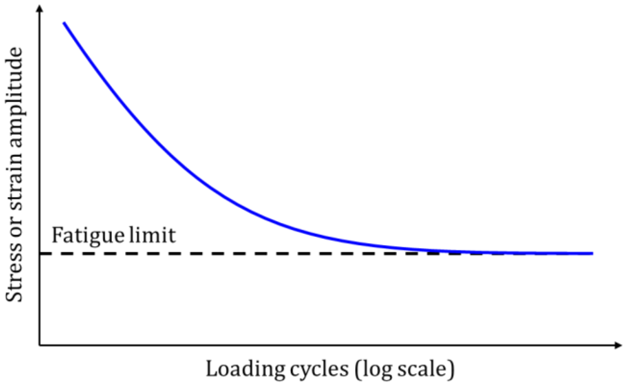

Figure 2.9 Schematic plot of the relationship between loading amplitude and cycles to failure.

Coffin [34] and Manson [35] later independently expanded the characterisation for a strain-life approach, including the effect of plastic strain. This is applicable to low cycle fatigue applications where loading results in stresses close to or above the elastic limit of the component of interest. The relationship is expressed as,

$$\frac{\Delta\epsilon}{2} = \frac{S_f'}{E}\left(2N_f\right)^b + \epsilon_f'\left(2N_f\right)^c \qquad \text{Eq. 2.4}$$

$\Delta\epsilon$ = Strain range

E = Young's modulus of the material

ϵ_f' = Fatigue ductility coefficient (approximately the fracture ductility in a monotonic tensile stress)

b = Fatigue ductility exponent

These models are later expanded for different materials and probabilistic analysis as summarised in [36], but the fundamental concept of plotting loading amplitude with number of loading cycles to failure remains the same.

2.1.2.2 Damage-tolerant approach to fatigue damage

Contrary to the safe-life approach, the damage-tolerant approach uses fracture mechanics and empirical crack growth laws to determine the fatigue life of a component containing a pre-existing defect. There are two ways of implementing the damage-tolerant approach to managing fatigue damage in engineering structures, depending on whether a defect is or is not found after an inspection. When defects are found following an inspection, the size of the defect may be obtained, and empirical crack growth laws may be used to estimate the growth of the identified defect and thus remaining life. Alternatively, when defects are not found, it can be conservatively assumed that the component contains the largest defect that may be missed by the inspection technique, and thus evaluating its remaining life.

There are many empirical crack growth laws that can be used to evaluate the remnant life of a component containing a defect. The most well-known is the Paris' crack growth law which very well describes the Stage II long crack growth regime as discussed in Section 2.1.1.2 [37]. The Paris' law is described as,

$$\frac{da}{dN} = C(\Delta K)^m \qquad \text{Eq. 2.5}$$

$\frac{da}{dN}$ = Crack growth per cycle of loading

ΔK = Stress intensity factor range

C = Paris' constant

m = Paris' exponent

The model has since been adapted in numerous ways to account for Stage I and Stage III crack growth, together with the effect of load ratio, crack closure, fracture toughness of the material and the threshold stress intensity of the material. A commonly-used equation for this is the Forman-Newman (or NASGRO) equation [38], which is,

$$\frac{da}{dN} = C'\left[\left(\frac{1-f(R)}{1-R}\right)\Delta K\right]^{m'} \frac{\left(1-\frac{\Delta K_{th}}{\Delta K}\right)^{p}}{\left(1-\frac{\Delta K}{(1-R)K_c}\right)^{q}} \qquad \text{Eq. 2.6}$$

C', m', p and q = Material constants

R = Load ratio

$f(R)$ = Empirical crack opening polynomial function

ΔK_{th} = Material stress intensity threshold

K_c = Material fracture toughness

The validity of the above theories depends on the validity of the small-scale yielding approximation, which assumes that the plastic zone size as defined in Section 2.1.1.2 is sufficiently small compared to other physical dimensions of the cracked body [39]. Under such conditions, linear elastic stress fields and thus the stress intensity factor can be used for fracture mechanics and crack growth analysis. For applications that result in greater plasticity ahead of the crack tip, more advanced methods such as the J-integral approach would be required [40], [41].

2.1.2.3 Effect of variable amplitude loading

Cyclic loading experienced by engineering structures is rarely of constant amplitude and often varies over time. The simplest way to account for damage accumulation from variable amplitude loading is to assume linear damage accumulation, thus using Miner's rule [42] to sum the contributions of individual loadings to evaluate the fatigue damage accumulated in a component. For a component that experiences cyclic loading of $i = 1, 2, \dots k$ different amplitudes with each loading amplitude denoted as S_i, its damage state, D, is expressed as,

$$D = \sum_{i=1}^{k} \frac{n_i}{N_f(S_i)} \qquad \text{Eq. 2.7}$$

In the equation, n_i is the number of loading cycles with amplitude S_i the component experiences. $N_f(S_i)$ is the number of loading cycles of amplitude S_i the component can withstand before failing; this is typically obtained from the Basquin law. A component is considered to have failed when $D = 1$.

In order for Miner's rule to be used, cycle counting algorithms which enables load cycles to be extracted from load histories are required. The most common cycle counting algorithm is the Rainflow counting method proposed by Endo et al. [43]. Loading sequences are first reduced to relevant peaks and valleys, and the cycles of complete hysteresis loops are counted and recorded as demonstrated in Figure 2.10. A guide to the counting method can be found in [44]. By using a stack-based implementation and recursive algorithm, Musallam [45] was able to further develop the Rainflow counting method for it to be used in real-time applications, which will be useful for SHM conditional monitoring.

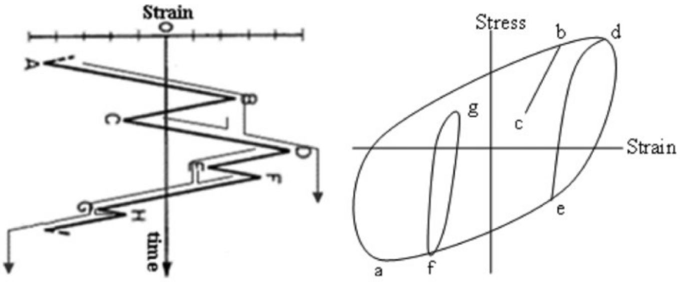

Figure 2.10 Schematic of the Rainflow cycle counting method. [45]

However, it is important to note that the above linear damage accumulation model neglects the effect of load interactions, which can both accelerate or decelerate crack growth under variable loading conditions. It has been well known that the sequence of variable amplitude loading has a significant effect on fatigue life [46], and extensive research has been conducted on model and predict these effects [47]. For instance, a single overload would result in a large plastic zone ahead of the crack and hence blunting the crack tip [48]. This results in a reduction in crack growth rate and hence an increased fatigue life. Moreover, Elber has shown that due to residual stress at the crack tip as a result of plastic deformation, the crack closure effect can play a significant role in the rate of crack propagation even when load cycles are fully in tension, and that it is one of the key contributors to the interaction effects of variable amplitude loading [49].

There are cases of variable amplitude loading when the loading spectrum is stationary, meaning that the distribution of loading amplitudes remains constant over time; an example of this would be the wind loadings of wind turbines [50]. For such cases, it is possible to use the equivalent constant amplitude loading approach to account for the variation in load amplitudes and also load interaction effect as demonstrated in [51], [52] and illustrated in Figure 2.11.

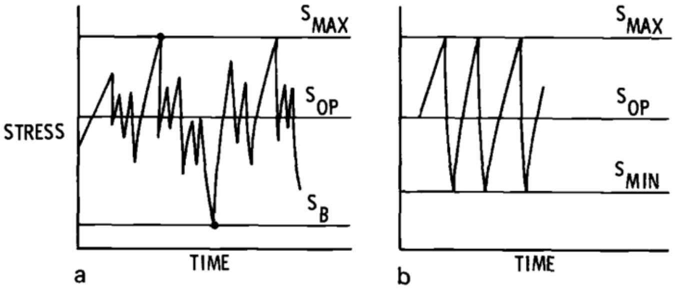

Figure 2.11 Illustration of the equivalent constant amplitude loading approach, showing (a) the real loading, and (b) the equivalent constant amplitude loading. [51]

2.1.2.4 Fitness-for-service criterion for the damage-tolerant approach

When evaluating the remaining life of a defective component using the damage-tolerant approach, it is necessary to define a critical defect size above which the engineering component would no longer be considered fit for service. This is typically defined as either a loss of function or structural failure. An example of a loss of function would be a through-wall crack in a pressure vessel that results in leakage, but the presence of the crack would not cause a structural failure under loading. In this case, the critical defect size would simply be equal to the thickness of the wall. Such a component is said to be designed to leak-before-break, or more generally designed to fail-safe.

For components that are not designed with a fail-safe criterion, a fracture mechanics analysis is conducted to evaluate the critical defect size that would result in structural failure. Of the different methods available, standardised failure assessment diagrams (FAD) are typically used in the industry as schematically shown in Figure 2.12 [16], [53].

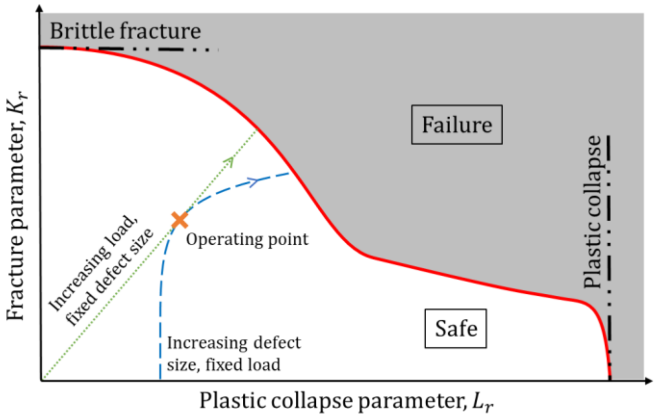

Figure 2.12 Schematic illustration of a failure assessment diagram (FAD).

The FAD plots a graphical relationship between the fracture parameter, K_r, and the plastic collapse parameter, L_r, which are parameters that increases proportionally with increasing loading. The fracture parameter, K_r, is the maximum stress intensity experienced by the component normalised to the fracture toughness of the material. Under linear-elastic conditions, the component would fail by brittle fracture if $K_r \geq 1$.

The plastic collapse parameter, L_r, is the nominal reference stress experienced by the component near the defect normalised to the elastic limit (typically the 0.2% proof stress) of the material. One could imagine that as defect size increases, the amount of material that remains intact decreases, resulting in an increase in the reference stress. Hence, the component would fail by plastic collapse when the combination of defect size and loading results in excessive plastic deformation ($L_r > 1$).

Any combination of defect size and loading for a component can be reduced to an operating point on the FAD; an example operating point is shown as an orange cross on Figure 2.12. The component is considered safe if the resulting operating point lies within the FAD line. The FAD can also be used to evaluate the maximum load which the defective component can withstand (dotted green line on Figure 2.12), as well as the maximum tolerable defect size for a given load (dashed blue line on Figure 2.12). The latter is of great importance to remaining life estimation using the damage-tolerant approach, as a critical defect size may be defined from this analysis. Note that the maximum loading possible that the component may experience should be used in the FAD analysis instead of the nominal load; an example of this would be extreme weather loadings for offshore structures [54].

2.1.2.5 Challenges in evaluating the growth of small defects

To this point, the engineering approaches to fatigue analysis of nominally defect-free component as well as components containing macroscopic defects have been discussed. Clearly there is a transition from which a component goes from being nominally defect free to containing a macroscopic defect. This transition can be illustrated using the Kitagawa-Takahashi diagram as described in [55], [56] and shown schematically in Figure 2.13.

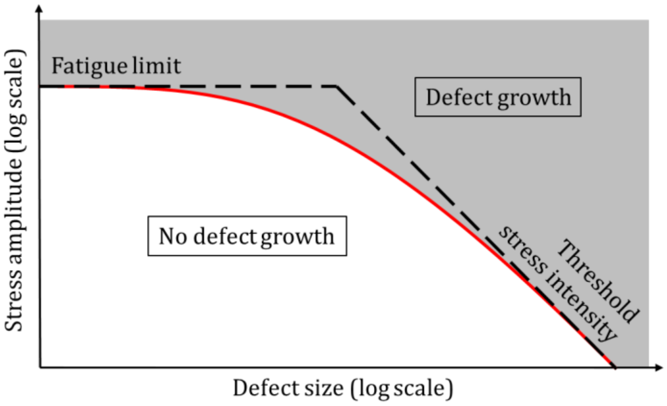

Figure 2.13 Schematic plot of a typical Kitagawa-Takahashi diagram.

The Kitagawa-Takahashi diagram plots, for a range of defect size, the maximum allowable stress amplitude which would in theory result in infinite fatigue life. As seen from the plot, for microscopic defect sizes, the limiting stress amplitude would tend towards the fatigue limit of the material obtained from the S-N curve, whereas for large macroscopic cracks, it would tend towards the stress amplitude resulting in the threshold stress intensity of the material.

In between the two regions, there is a region where the damage growth properties transition between the two, during which a defect may grow even if it is below the fatigue limit and the stress intensity threshold. This is closely linked to Phase 2 of defect growth as discussed in earlier sections, and the evaluation and prediction of fatigue damage progression at this phase is very challenging due to its sensitivity to microstructure; a review on the current state-of-the-art can be found in [57].

A detailed understanding of defect growth in this region is beyond the scope of this research. What is important here is to acknowledge the challenge in modelling the growth of small defects (dimensions of order 0.1 to 1 mm [21]) and to be mindful of these limitations when using defect growth models for long macroscopic cracks when performing remnant life estimations as conducted later in this research.

2.2 Structural health monitoring for fatigue damage

Following a review in the mechanisms and engineering approaches to evaluating fatigue damage, a review of the current state-of-the-art of SHM technologies suitable for use as PIMS to monitor fatigue damage is provided. An outline of the basic principles of each relevant technology will be given, followed by a discussion on the benefits and challenges of using each method for SHM applications.

2.2.1 Vibration-based methods

With strategically placed accelerometers and/or laser doppler vibrometers, the vibration response of entire engineering structures can be monitored. By measuring the natural frequency, mode shape or mode shape curvature of the structure, any deviations from the undamaged state can be used as an indication of the initiation of defects [58]. This can subsequently be used to infer the structural health of the monitored structure. The use of vibration-based methods for SHM is common with civil structures such as buildings [59] and bridges [60].

While vibration-based methods can be used to monitor entire engineering structures with a relatively small number of sensors, there are several challenges in using it for detecting localised damage as summarised in [61]. Firstly, sensitivity of vibration-based methods to localised damage is significantly lower than other SHM methods. A comparative study for vibration response SHM on bridge girders shows that damage is only detected when there is a significant loss in cross-section area (~50%) unless a large amount of sensors are in place [60], [62]. It is therefore only realistically possible to detect severe local damage using vibration-based methods. Secondly, vibration-based methods for SHM would need to suppress or compensate the effect of environmental conditions such as temperature and marine growth for offshore structures; these effects can also significantly alter the vibration response of an engineering structure, thus invalidating the collected monitoring data. Lastly, vibration-based methods are very sensitive to changes in boundary conditions. This means that while failure near the joints of structures may be relatively easier to detect, sensitivity to localised damage in other areas is much lower. For instance, a cross-section loss at the root of a cantilever beam produces a much greater change in vibration response compared to a cross-section loss towards the free end of the beam [63].

2.2.2 Acoustic emission

When defects grow in a stressed component, elastic energy stored in the component is released, and a proportion of this energy dissipates in the form of elastic waves; these elastic waves are commonly known as acoustic emissions [64]. By appropriately attaching accelerometers or ultrasonic transducers on the component, these acoustic signals may be recorded, analysed and subsequently used as an indication of defect growth [65]. Various method for analysing acoustic signals are available, ranging from simple emission counting and spectral analysis [66], to more intricate methods such as artificial neural networks for damage type recognition [67], [68]. Depending on the specific application, sensor capabilities and signal processing technique used, the location, classification of defects and the rate of defect growth may be estimated from obtained signals. The first pronounced industrial use of acoustic emission methods is to certify pressure vessels during hydrostatic proof tests [69], [70], and its use have since been developed in multiple SHM applications, including civil structures [71], offshore structures [72] and aerospace structures [73].

One of the main benefits of acoustic emission sensors is that it can cover a substantial area, meaning that minimal sensors are required to cover a large structure. Also, the method is inherently a real-time monitoring technique that only detect actively propagating defects, which are usually the defects of concern in engineering structures.

The biggest challenge for acoustic emission methods is to separate acoustic signals that are a result of defect growth and acoustic signals that are from other irrelevant sources. As a result, advanced signal processing techniques performed by qualified personnel are likely needed. Even when signals of defect growth are correctly identified, the need to quantify the extent of damage would introduce another level of complexity to analysing the recorded acoustic signals.

Overall as concluded by Sengupta et al. [74], while the fundamental theory of acoustic emission methods is simple, it is one of the most challenging techniques to effectively implement in real-life engineering applications. Quantifying damage severity with acoustic emission methods is considered the most critical area of research for acoustic emission methods to be used for structural integrity assessment and remaining life estimations.

2.2.3 Active ultrasonic methods

Rather than detecting elastic waves emitted from growing defects, a more widely used acoustic method for defect detection involves actively transmitting and receiving ultrasonic waves using piezoelectric or electromagnetic transducers. The use of bulk wave, guided wave, and nonlinear ultrasonic methods will be discussed in this section.

2.2.3.1 Bulk ultrasonic wave

The use of bulk ultrasonic wave to detect internal flaws in a solid material dates back to the early 1940s [75]. An illustration from [76] on using bulk ultrasonic wave to detect defects is shown in Figure 2.14. Short bursts of ultrasonic waves, typically around the order of 1 MHz, are injected into the component of interest [77]. The following techniques can then be used to detect and characterise a wide variety of defects [78]:

- Amplitude techniques: use of a loss in transmission (i.e. pitch-catch) or an unexpected reflection of signals (i.e. pulse-echo) for indication and characterisation of defects
- Temporal techniques: use of the arrival time of scattered signals to detect and size defect (e.g. time-of-flight diffraction)
- Imaging techniques: producing a map of signal amplitude or phase by correlating time of arriving signal to a spatial point; this usually involves scanning across an area of interest and/or the use of an array of transducers.

- Inversion techniques: inferring the properties of a defect by modelling the scattered signal received by multiple transducers and use algorithms to iteratively adjust the properties of the defect until the modelled signal outputs match the actual signals measured.

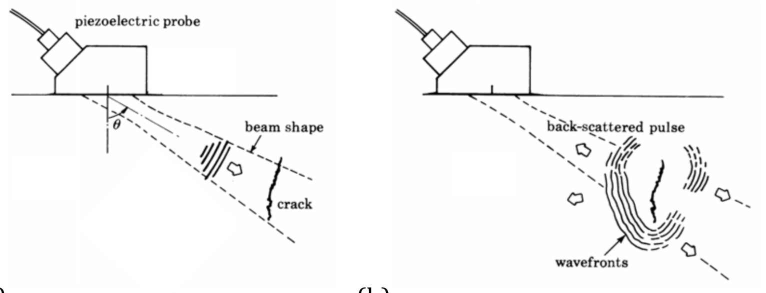

(a) (b)

Figure 2.14 Illustration of how the bulk wave ultrasonic method is used for defect detection. Modified from [76].

Although bulk wave ultrasonic testing is widely used for NDE inspections, there are currently few industrial applications of permanently installing ultrasonic sensors for SHM. An example of this would be the use of bulk wave ultrasonic sensors for wall thickness monitoring at high temperature environments as demonstrated and commercialised in [79], [80]. While bulk wave methods generally provide significantly better sensitivity to local defects compared to vibration-based and acoustic emission methods, its spatial coverage is also much smaller, meaning that its use for permanently installed SHM would be impractical unless the location of defect initiation is known with reasonable certainty.

2.2.3.2 Guided ultrasonic wave

As illustrated in Figure 2.15, the propagation of guided waves are guided by the structural form of the component it propagates through [81]. Guided wave propagation occurs when the thickness of the component is less than or of the order of the excited wavelength [82]. As the excited elastic wave is being constrained by the boundaries of the component, multiple reflections, refractions and mode conversion occurs, resulting in the generation of guided waves [83].

Guided wave methods are a common choice of technique for inspecting long and slender components such as pipes [84] and also plate structures using omnidirectional guided waves [85]. Guided waves can travel long distances with relatively minimal attenuation and covers the entire cross-section of the component, making it an effective inspection method for covering large areas with few inspection points. This also means that guided wave methods can be an attractive candidate for permanently installed monitoring.

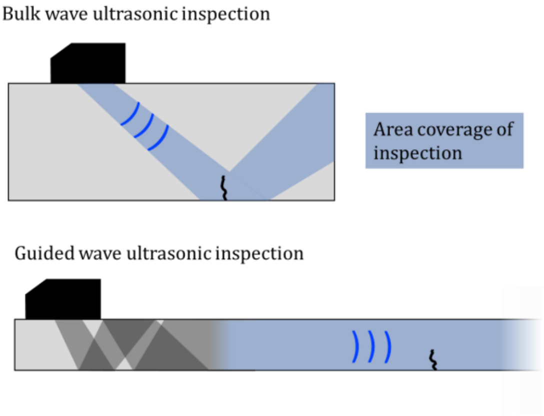

Figure 2.15 Illustration of the difference between bulk wave and guided wave ultrasonic inspection.

Significant research has been conducted in driving the development and implementation of guided wave methods for SHM. This ranges from transducer design, signal processing techniques and overcoming environmental effects; a recent review can be found in [86]. Notably, the use of guided waves for short range, higher sensitivity guided wave measurements has been studied to enable the detection and monitoring of fatigue cracks, which can prove to be beneficial for localised fatigue SHM [87].

2.2.3.3 Nonlinear ultrasonic methods

As an acoustic wave signal passes through a solid material, harmonics of the signal will be generated due to nonlinearity in the material, which originates from the anharmonicity of crystal lattices and also microscopic damage (i.e. dislocations) [88]. As discussed in Section 2.1.1.1, the accumulation of microscopic damage is what precedes the initiation of fatigue damage. Hence, it has been shown that quantifying the distortion in acoustic wave as a result of these microscopic damage can be used to measure the severity of fatigue damage of a component [89], [90]. The second-order nonlinearity parameter, β, is typically used; this is defined as the ratio of the amplitude between the fundamental and second harmonic of the measured ultrasonic signal. A sample plot of β against fatigue life of a laboratory specimen is shown in Figure 2.16.

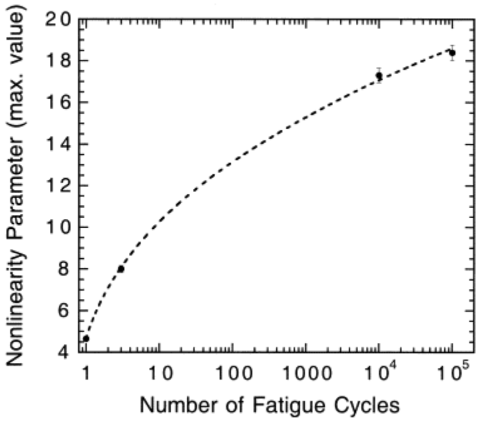

Figure 2.16 Example plot of the nonlinear parameter, β, against fatigue life for an Aluminium alloy AA2024-T4 laboratory specimen [90].

Given its potential to provide early indications of fatigue damage, the use of nonlinear ultrasonic methods has attracted considerable interest, with its use investigated for bulk wave and more recently guided wave methods. The analysis of nonlinear ultrasonic measurements is clearly more complex and not as established compared to linear methods, thus its use in real-life, in-service inspections is still currently very limited, let alone SHM applications.

2.2.4 Potential drop method

The potential drop method is typically used in laboratory conditions to monitor crack growth of fatigue or creep tests [91]. This method works by injecting current, AC or DC, into the specimen and measuring the change in resistance due to geometrical changes or changes in material properties, which can then be converted into defect sizes. An illustration of the potential drop method is shown in Figure 2.17. This method is typically used to size defects once found using other NDE methods, rather than used for inspection [92]. Also, the potential drop method is only sensitive to surface-breaking or near-surface defects.

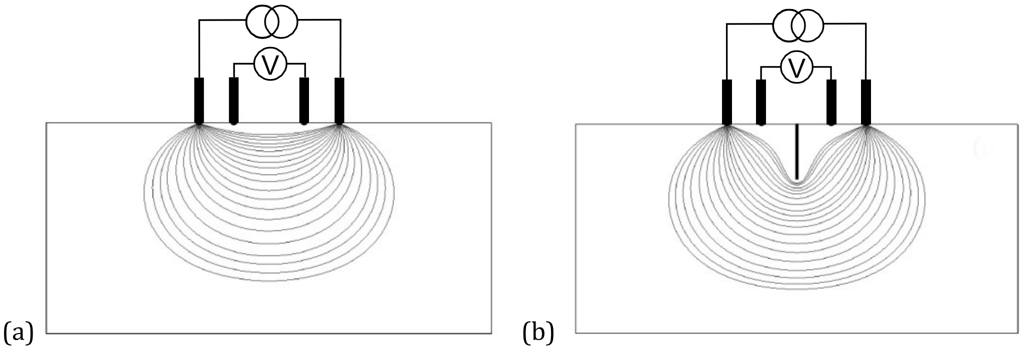

Figure 2.17 Illustration of the potential drop method, showing how current flow differs between the (a) defect-free case, and (b) defective case. Illustration modified from [93].

Area coverage of a potential drop sensor depends largely on the spacing of electrodes; large spacing of electrodes increases spatial coverage at the cost of sensitivity. An advantage of the potential drop method is that the individual electrodes for the potential drop method is relatively inexpensive and simpler to permanently install. This means that an array of current injection and sensing probes can potentially be permanently installed to maximise area coverage while retaining good sensitivity. The use of an array of potential drop sensors have been demonstrated for monitoring of creep damage [94].

There are a number of challenges and limitations to the use of potential drop methods for fatigue SHM monitoring. Primarily, electromagnetic properties of the component must remain stable or be compensated under operating conditions to enable accurate measurements. If sizing of the defect is required, this can prove to be a complicated task for real-life engineering components with complex geometries. The effect of strain and plasticity also further complicates the relationship between defect size and resistance [95].

2.3 Discussion

From this literature review, it is believed the following aspects need to be considered for a successful implementation of SHM of fatigue damage.

Overall, it is believed that for permanently installed SHM to be implemented to monitor fatigue damage in real-life engineering applications, the following needs to be considered.

Firstly, research and development in SHM technology needs to be in line with the research and development of fatigue damage growth in real-life applications. An SHM technology that can detect damage at an early stage of component life does not necessarily translate into better structural integrity assessment if it is not complemented with accurate defect growth predictions.

A literature review of the understanding of fatigue damage reveals that accurately predicting the growth of small, microstructure-dependent defects remains a challenging problem, not to mention in real-life applications with complex loading and environmental conditions. This would suggest that being able to detect damage at an early stage of component life using SHM technology may currently have limited value from the point of view of assessing the structural integrity and remnant life of the component; there is huge uncertainty as to whether or how these damage will evolve and ultimately lead to failure.

It is believed that the key value of implementing SHM technology is the ability to continuously monitor for the presence of substantial, macroscopic damage in order to provide confidence in the structural integrity of the monitored component. With the use of macroscopic crack growth laws, it can be assured that failure of the monitored component is not imminent when no substantial damage is detected by the SHM system. In cases where substantial damage is detected, measurements collected by the SHM system may also be used to continuously update the predicted remnant life of the component. The use of SHM measurements to detect and monitor the growth of macroscopic fatigue damage will be investigated in Chapters 5 and 6.

Secondly, there is a need to optimise sensor coverage and sensitivity. As shown in the review above, different SHM techniques have varying capabilities in terms of spatial coverage and sensitivity. Requirements for these capabilities are highly dependent on the certainty in defect location and crack growth behaviour. No matter how sensitive an SHM technique is, if it does not sufficiently cover all areas where a defect may initiate, confidence in structural integrity may not be sufficient. This will be investigated in Chapter 4 of this thesis, where a framework to quantify the trade-off between sensor coverage and sensitivity will be developed and demonstrated.

Finally, the implementation of SHM would have to be attractive from an economic point of view compared to existing inspection approaches while maintaining the same level of confidence in structural integrity. Applications that would favour the use of SHM would be cases where inspection is ineffective (e.g. limited accessibility or disruptive) and those where defect growth is rapid such that frequent inspections are required to be confident in structural integrity [61]. With the frameworks and methods developed throughout the thesis, the efficacy of SHM for specific applications can be quantified and compared to conventional inspections. Results obtained from the analysis using the developed frameworks can then be implemented with methods of cost analysis for evaluation from an economic point of view.

3 Evaluating the detection capabilities of permanently installed monitoring systems

3.1 Introduction

The value of PIMS is determined by the confidence in its detection capabilities; PIMS can only provide sufficient confidence in structural integrity if it is capable of detecting defects reliably. To this end, for data collected by PIMS to be integrated into real-time structural integrity assessments or 'digital twins' [96], the detection capabilities of PIMS needs to be systematically quantified.

The detection capabilities of PIMS may be evaluated using the receiver operating characteristics (ROC) analysis, whereby two metrics are used to quantify its detection capabilities. First is the probability of detection (POD), defined as the probability of detecting a defect of given severity. Second is the probability of false alarm (PFA), defined as the probability of falsely detecting a defect when there is none. A more in-depth review of ROC analysis is given later in Section 3.3.

The detection capabilities of PIMS is determined by the effect of numerous sources of uncertainty; examples include sensor and defect location, defect orientation, defect morphology, electrical noise, and environmental influences. Evaluating the detection capabilities of PIMS presents unique challenges compared to conventional NDE inspections, arising from the fact that PIMS are, by definition, permanently installed at a fixed position. If the measurement conditions are unfavourable (e.g. installed in a poor position), the POD may be severely compromised, undermining the reliability of the monitoring system. Further, the

POD usually refers to a single measurement in isolation, but one of the aims of this thesis is to make use of the series of measurements from PIMS; the effect of systematic uncertainties is problematic as each successive measurement may not be considered fully independent from previous measurements.

This chapter aims to lay out a model-assisted methodology for evaluating the POD of PIMS that distinguishes between sources of uncertainty that are random and systematic. The use of model-assisted methods will be necessary since it would be impractical to conduct the large number of destructive tests required for a probabilistic analysis, especially as each would require samples with PIMS installed on them. The methodology forms the basis for the following two chapters. In Chapter 4, the analysis is applied to the problem of assessing the detection capabilities of PIMS where the location of damage is uncertain. In Chapter 5, the analysis is used for probabilistic forecasting of remaining life based on a series of PIMS measurements.

This chapter is structured as follows. In Section 3.2, a simple example that will be used throughout to demonstrate the proposed methodology is outlined. Section 3.3 then gives a description of the fundamental theories for probability of detection. Section 3.4 discusses the intricacies and challenges specific to quantifying the sources of uncertainties of PIMS and proposes a way of overcoming these challenges. Section 3.5 proposes how the use of prior knowledge on systematic factors (e.g. likely defect orientation) may be incorporated into the analysis of detection capabilities. Finally, a discussion and conclusion of the chapter is given in Section 3.6 and 3.7.

3.2 Outline of the example problem

An example problem is used throughout the chapter to demonstrate the process of evaluating the detection capabilities of PIMS. In the example problem, we seek to evaluate the detection capabilities of a potential drop monitoring system to detect a penny-shaped crack of diameter, d, within a steel bar. The example problem is shown in Figure 3.1. The dimensions of the rectangular steel bar are $150 \times 32 \times 20$ mm. The axisymmetric crack has three translational and two rotational degrees of freedom; for simplicity, the example problem will only consider one rotational degree of freedom, θ, as shown in Figure 3.1(a). It is assumed that the crack will always be located at the centre of the beam. The more challenging problem of translational uncertainty will be the focus of the following chapter.

The potential drop monitoring system used in the example is similar to that described in Section 2.2.4. A DC monitoring system is used as its response can be simply modelled with commercial finite element software. Also, an AC monitoring system would not be sensitive to internal defects as alternating current would concentrate towards the outer surfaces of the bar [97], thus not suitable for this example problem.

The monitoring system consists of four electrodes, two on each end of the beam. Current is injected between a pair of electrodes and the electric potential is measured by the other pair as illustrated in Figure 3.1(b). The presence of a defect forms an impediment to the current flow and therefore increases the resistance. A relative increase in resistance indicates the growth of a defect. We seek to evaluate the detection capability of the potential drop monitoring system for a range of defect sizes.

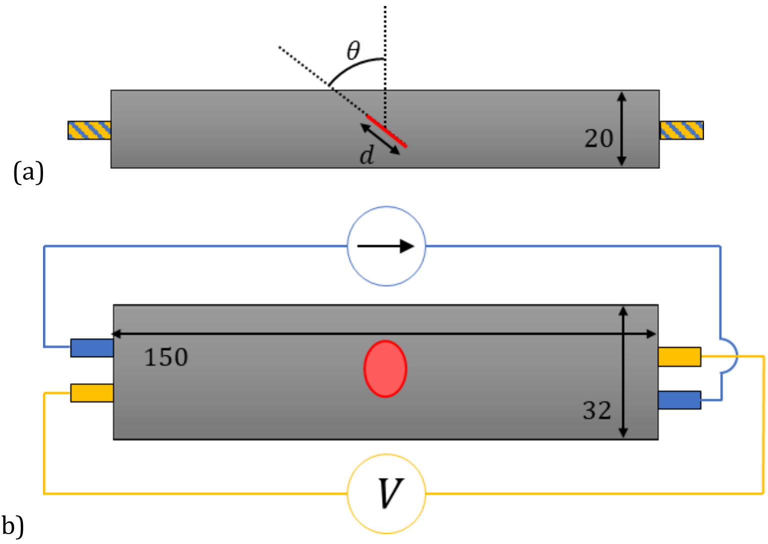

Figure 3.1 Setup of the example problem; (a) side view, (b) top view.
The sought penny-shaped crack is represented in red. All dimensions in mm.

3.3 Receiver operating characteristic analysis of PIMS

3.3.1 Theory of receiver operating characteristic analysis

PIMS may be considered as systems that output a signal, X, that is correlated to the likelihood of a defect being present in the monitored component. In the example potential drop problem, the output signal would be the relative change in resistance which scales with defect severity. Another example would be an ultrasonic sensor which returns the maximum amplitude of a reflected signal from a defect. In both cases, the greater the signal, the more likely it is that a defect is present.

Given that the output of PIMS will inevitably be subject to sources of uncertainties, it is appropriate to model their possible outputs as probability distributions, $P(X)$. The distribution given the monitored component is defect-free would be $P(X|\text{no defect})$; the distribution given a specific class of defect is present in the monitored component would be $P(X|\text{defect})$. The distributions are schematically illustrated in Figure 3.2.

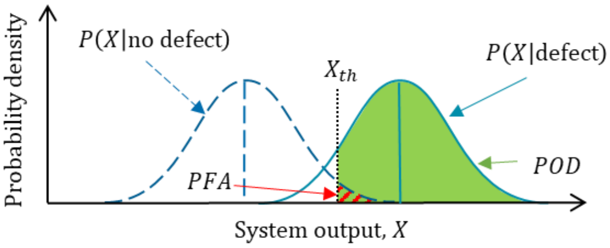

Figure 3.2 Schematic illustration of the probability distributions of the system output, X, for a defect-free case, $P(X|\text{no defect})$, and; a defective case, $P(X|\text{defect})$.
A threshold, X_{th}, is chosen and the corresponding POD and PFA is shown.

In order for PIMS to distinguish between the defect-free and defective cases, a signal threshold, X_{th}, is typically defined such that a defect is called when the PIMS outputs $X > X_{th}$. This is represented as the dotted black line in Figure 3.2. With this, two metrics may be evaluated for a chosen X_{th}. The first is the probability of detection (POD), which quantifies how well PIMS perform in terms of calling a defect if present. The POD is illustrated as the area shaded in green in Figure 3.2, and is defined as,

$$POD = P(X > X_{th}|\text{defect}) \qquad \text{Eq. 3.1}$$

The second metric is the probability of false alarm (PFA). This metric defines how well PIMS perform in terms of not calling a defect when the component is defect-free. The PFA is illustrated as the area shaded in red dashes in Figure 3.2, and is defined as,

$$PFA = P(X > X_{th}|\text{no defect}) \qquad \text{Eq. 3.2}$$

Clearly, the choice of X_{th} would have a significant effect on the performance characteristics. A useful plot to visualise the performance is to plot its POD and PFA for a range of X_{th}, producing what is known as the receiver operating characteristic (ROC) curve; illustrative examples of this are shown in Figure 3.3. On this plot, a small X_{th} would result in a point close to $(1, 1)$ on the ROC space, corresponding to having a high POD at the cost of a high PFA. Conversely, a large X_{th} would result in a point close to the origin of the ROC space, corresponding to having a low PFA but also a low POD. A useful metric to gauge the performance of the PIMS is to evaluate the area under the ROC curve. A perfect system (i.e. $POD = 1$ and $PFA = 0$) would have an area of unity; a naïve system which randomly outputs a positive result would have an area of 0.5. In practise, PIMS would lie somewhere between the naïve and the perfect system, as represented by the solid blue and the dashed red curve.

The appropriate choice of X_{th} depends on the nature of the application. The decision process typically involves weighing the risks and consequences of missing a defect and making a false call. For instance, if the risk of missing a defect is catastrophic, it may be worthwhile to choose an operation point with a higher POD at the expense of a higher PFA; this corresponds to choosing a lower X_{th} value. On the other hand, if the consequence of a false alarm is very costly, an operation point with a low PFA at the expense of a lower POD would be chosen; this corresponds to choosing a higher X_{th} value. In practise, X_{th} is usually chosen to meet the predefined requirement of a maximum allowable PFA or a minimum required POD, and the corresponding POD or PFA is used as a metric to gauge the capability of the PIMS.

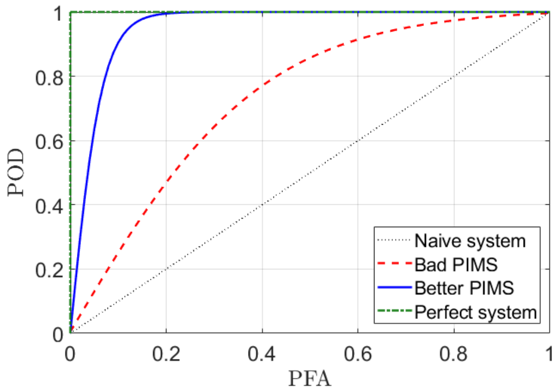

Figure 3.3 Illustrative plot of various ROC curves in the ROC space.

3.3.2 Probability of detection curves

It is often essential to characterise the capabilities of PIMS in terms of how small a defect it can reliably detect. To characterise the performance of PIMS in terms of defect sizes, the probability distribution, $P(X|\text{defect})$, for a range of defect sizes needs to be obtained. To do so, ROC analysis will have to be repeated for a range of defect sizes, subsequently obtaining POD as a function of defect size (for a given X_{th} and thus PFA). The plot of POD against defect size is known as a POD curve, and is a standardised way of representing the performance of NDE systems [98], [99]. A schematic illustration of a typical POD curve is shown in Figure 3.4. The POD curve typically takes the form of a logistics curve, whereby the POD approaches the predefined PFA when defect size is close to zero (i.e. defect-free) and approaches unity with increasing defect size.

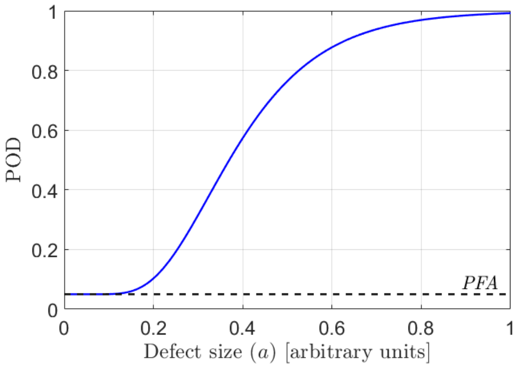

Figure 3.4 Schematic illustration of a POD curve, plotting POD against the depth of a defect.

3.4 Evaluating the sources of uncertainties of PIMS

From the above theory of ROC analysis, it is clear that accurately defining the distributions $P(X|\text{no defect})$ and $P(X|\text{defect})$ is crucial to evaluating the detection capabilities of PIMS. This in turn means that uncertainties in the signal output of PIMS need to be accurately quantified. There are numerous sources of uncertainty including random effects such as electrical noise, and systematic effects such as defect location. The treatment of different sources of uncertainty will have to be carefully considered in order to ensure that the statistical interpretation of the ROC and POD curves is robust.

Quantifying the uncertainty of periodic NDE inspections is comparatively well established [99]. Measurements taken with periodic inspections are relatively infrequent, and it is highly unlikely that successive inspections of the same component will be performed under exactly the same conditions by exactly the same equipment (even if the 'same' technique is used). Therefore, many sources of uncertainties may be considered independent between successive inspections of the same component. Hence, the effect of relevant factors can simply be combined to produce a single representative probability distribution. Thereon, conventional ROC analysis can be performed to evaluate its detection capabilities.

The same treatment is not applicable for PIMS. PIMS are by definition permanently installed onto a specific component, and this combination of sensor and component will last for the entirety (or at least a significant portion) of the service life of the component. If systematic factors such as error in sensor placement or deficient sensor-component coupling have a significant effect on the detection capabilities, then the reliability of the system may be hindered. Further, if all sources of uncertainty are treated as independent, systematic bias or serial correlation between successive measurements will cause significant discrepancy between the predicted and actual detection capabilities. Thus, while random sources of uncertainty contribute to the variance in the distributions, systematic uncertainty will instead have the effect of reducing the confidence in the central tendency of the distributions.

It is proposed that the sources of uncertainties can be divided into three categories: short-term random uncertainties, medium-term uncertainties, and long-term systematic uncertainties. The following sections give a description of these three categories of uncertainties, together with how each should be considered in the context of evaluating the detection capabilities of PIMS for structural integrity assessment.

3.4.1 Short-term random uncertainties

Short-term random uncertainties are sources of uncertainties that effect the system output at a much faster rate than the rate at which measurements are taken. As a result, the effect of these sources of uncertainties are essentially randomised for each successive measurement taken. Independent sources of random uncertainty can easily be evaluated and aggregated, subsequently contributing to the variance in the probability distributions $P(X|\text{no defect})$ and $P(X|\text{defect})$. Illustrative distributions of varying amount of random uncertainty in the system output is shown in Figure 3.5.

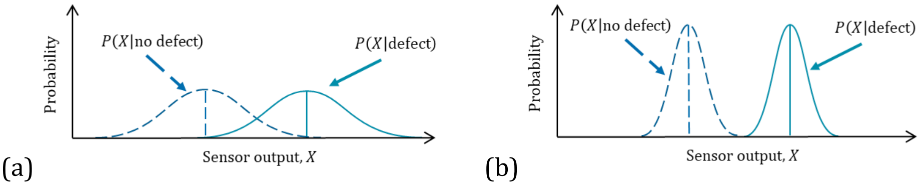

Figure 3.5 Illustrative distributions of $P(X|\text{no defect})$ and $P(X|\text{defect})$ with (a) large random uncertainty, and (b) small random uncertainty.

Few sources of uncertainties can be considered as short-term random uncertainties with PIMS; an example would be internal electrical noise. Moreover, since random uncertainties may be effectively suppressed by averaging, random uncertainties are generally of lesser importance to PIMS.

3.4.2 Medium-term uncertainties

In practise, various sources of uncertainty neither change instantaneously nor are truly constant throughout the entire life of the component. These medium-term uncertainties affect the system output change at a rate similar or slower than the rate at which measurements are taken. It can be challenging to decide on their treatment. The approach suggested in this Chapter is to either treat them as short-term or long-term according to the following guidance.

A well-recognised problem in the use of PIMS is the influence of environmental effects such as the operating temperature of the monitored component or measurement system, consequently the sensor output may fluctuate on a daily or yearly timescale along with the temperature. The introduction of serial correlation in the data leads to a systematic uncertainty in the defect free signal that will limit the detection capabilities. To overcome this, methods must be employed to compensate or suppress the influence of temperature; examples of temperature compensation schemes for guided wave monitoring can be found in [100], [101]. The use of compensation schemes has been shown to be sufficiently effective at limiting the effect of temperature to a level where the residuals may be considered random [102], [103] and can therefore be treated as a short-term random uncertainty.

Some medium-term effects cannot be suppressed; an example of this would be defect morphology. While a defect may have a particular realisation of shape or roughness at a given instance, over time its morphology may evolve to become either more or less favourable to be detected. Clearly, near-instantaneous repeated measurements are not going to overcome the problem of unfavourable defect morphology, nor would it be possible to suppress the effect with compensation methods. Therefore, this source of uncertainty must be treated as a long-term systematic uncertainty.

3.4.3 Long-term systematic uncertainties

Systematic uncertainties are factors that nominally do not change over the service life of a sensor-component combination. There are a wide variety of parameters that contribute to systematic uncertainties in the signal output of PIMS, and this has been studied in a wide range of literature. Some examples of these parameters include defect characteristics (e.g. location [104], orientation [105], morphology [106]), sensor characteristics (e.g. position [104], and coupling between the sensor and the component [107]).

In most cases, multiple factors would result in systematic uncertainty and not all of them may be independent of each other. Therefore, simulations on a range of combinations of these factors are needed to capture their combined effect on the expected response of PIMS. Ultimately, the effect of these factors would contribute to uncertainty in the central tendency of the distributions $P(X|\text{no defect})$ and $P(X|\text{defect})$. This is illustrated in Figure 3.6 where distributions of favourable and unfavourable combinations of systematic factors are shown. Consequently, separate ROC analysis will need to be completed for a range of combinations of systematic factors to produce a population of ROC curves and subsequently POD curves for a given threshold. The resulting range of POD curves would subsequently inform the uncertainty and confidence in the detection capabilities.

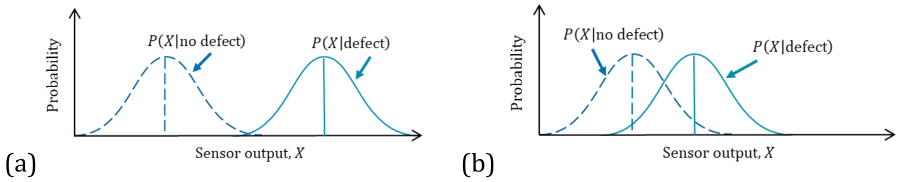

Figure 3.6 Illustrative distributions of $P(X|\text{no defect})$ and $P(X|\text{defect})$ with (a) favourable, and (b) unfavourable combination of systematic factors.

3.4.4 Analysis of the example problem

For simplicity, only the effect of random signal noise and defect orientation will be considered in the example problem. Evidently, random signal noise will contribute to the random uncertainty and defect orientation will contribute to the systematic uncertainty.

3.4.4.1 Random uncertainties

The effect of random signal noise is assumed to follow the normal distribution,

$$X_{PD} \sim normal(\bar{X}_{PD}, \sigma_{PD}) \qquad \text{Eq. 3.3}$$

where $\bar{X}_{PD}$ is the expected sensor output as evaluated in the following section and σ_{PD} is the standard deviation. σ_{PD} is assumed to be 2.8×10^{-4} in this analysis. This is approximated from the anticipated resistance measured by the monitoring system being of order $10\ \mu\Omega$ based on finite element results. This is then combined with the fact that a state-of-the-art potential drop system can produce resistance measurements of the same order of magnitude with standard deviation of approximately $2.8\ n\Omega$ [108].

3.4.4.2 Systematic uncertainties

To evaluate the expected responses of the potential drop monitoring system, $\bar{X}_{PD}$, finite element simulations using COMSOL Multiphysics were conducted to evaluate the expected resistance measurement, R, for the defect-free case as well as a range of defect diameter, d, and orientation, θ. The range of defect diameter evaluated is from $d = 0.5$ mm to $d = 15$ mm in increments of 0.5 mm; the range of defect orientation evaluated is from $\theta = 0°$ (i.e. normal to current flow) to $\theta = 90°$ (i.e. parallel to current flow) in increments of 5°.

The final system output of the potential drop monitoring system is the change in normalised resistance, which is defined as,

$$\bar{X}_{PD} = \frac{R_{defect}}{R_{no\ defect}} - 1 \qquad \text{Eq. 3.4}$$

where the subscript indicates the defective and defect-free states. The plot of $\bar{X}_{PD}$ as a function of defect size is shown in Figure 3.7(a); the plot of expected response as a function of defect orientation is shown in Figure 3.7(b). A PFA of 10^{-3} is chosen for this example. This is used to evaluate the corresponding threshold, X_{th}, as schematically demonstrated earlier in Figure 3.2 using the distribution, $P(X_{PD}|\text{no defect})$. The resulting value of $X_{th} = 0.865 \times 10^{-3}$ is also shown in Figure 3.7(a) and (b). It is clear from the results that the potential drop monitoring system is very sensitive to the defect orientation. As θ increases, the effect of the defect obstructing in electric current flow quickly diminishes and therefore sensitivity also reduces.

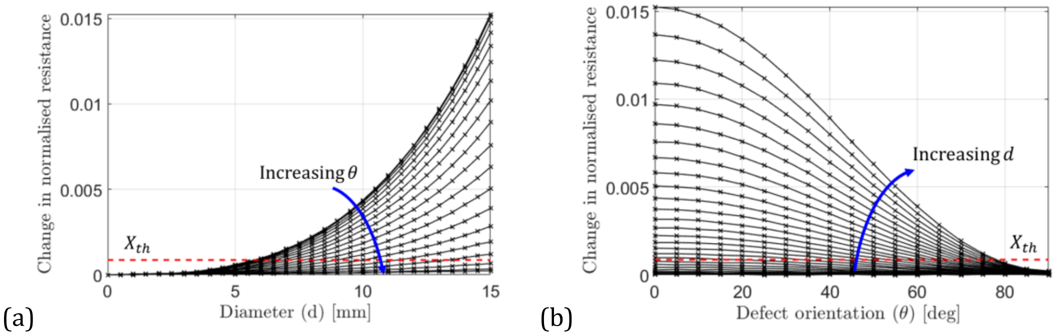

Figure 3.7 Results from the finite element simulations of the example problem, plotting (a) change in normalised resistance as a function of defect diameter, and (b) change in normalised resistance as a function of defect orientation.

3.4.4.3 ROC analysis and POD curves

With the effect of random and systematic uncertainties quantified, there is now sufficient information to construct the probability distributions $P(X|\text{no defect})$ and $P(X|\text{defect})$ for each combination of defect orientation and size. With this, ROC analysis as detailed in Section 3.3.1 can be performed, resulting in a population of ROC curves for a range of defect orientations and sizes. Finally, POD curves for a given PFA as detailed in Section 3.3.2 for each defect orientation can be plotted; the results for $PFA = 10^{-3}$ are shown in Figure 3.8.

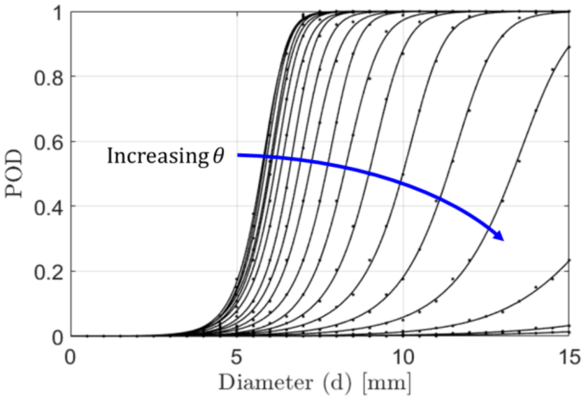

Figure 3.8 POD curves for $PFA = 10^{-3}$ from the results for the example problem.

3.5 Incorporating the statistical variations of systematic factors

Evaluating the anticipated POD from Figure 3.8 is clearly dependent on what is the anticipated angle of the crack. From the results, at $d = 10$ mm, the POD ranges anywhere between 0 and 100%, reflecting an exceptional lack of confidence in the detection capability of the monitoring system when there is no prior knowledge on the likely defect angle. However, in practise, it is often possible to obtain information on the likelihood of crack orientation, or more generally, any other relevant systematic factors. This information may come in the form of statistical distributions based on underlying physics, computational analysis, experiments, or simply a survey from previous experiences. Using the Monte Carlo method where systematic factors are sampled from these distributions, the statistical expectation and confidence levels in POD of the monitoring system when used for a specific application may be evaluated. This approach closely resembles the model-assisted probability of detection (MAPOD) approach for NDE inspections as implemented in the CIVA software designed for assessing NDE inspection techniques [109], [110].

In the context of the example problem, suppose the penny-shaped crack we sought to detect typically originates from a 60° "V" groove weld as illustrated in Figure 3.9. As a result, we arbitrarily assume, for illustration purposes, that the probability distribution of defect orientation follows a normal distribution with a mean of 30° and a standard deviation of 5°; a plot of the distribution is shown in Figure 3.10.

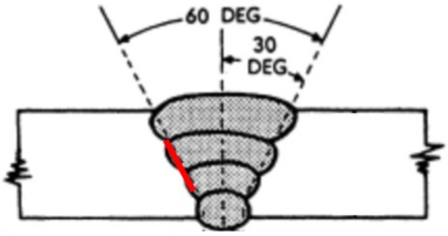

Figure 3.9 Illustration of a 60° "V" groove weld modified from [111]. The sought penny-shaped crack is indicated by a red line.

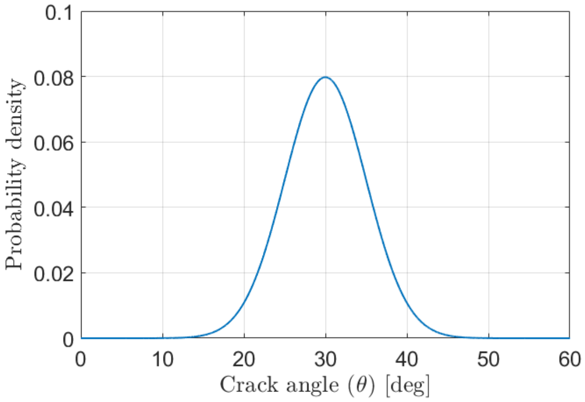

Figure 3.10 Plot of the distribution of crack orientation.

A 1000-trial Monte Carlo simulation is carried out to evaluate the expected response of the monitoring system and subsequently POD as a function of defect size for a distribution of defect orientations. For each trial, a sample of crack orientation is drawn from the distribution shown in Figure 3.10, and the expected response of the monitoring system for a range of defect sizes is interpolated from the finite element results. The probability of detecting a crack at the sampled orientation is subsequently evaluated for each defect size using the ROC analysis. With this, a POD curve for a crack at the sampled orientation is obtained. By repeating the process for all sampled defect orientations, a population of POD curves is produced; a selection of this is plotted in Figure 3.11.

For each defect size, a histogram and empirical cumulative distribution function (CDF) of POD can be plotted; an example for $d = 7$ mm is shown in Figure 3.12. With this, the expected POD for each defect size, POD_{exp}, can be evaluated simply as the average of the results in the histogram. Confidence bounds of POD for each defect size can also be obtained from the empirical CDF; this is illustrated in Figure 3.12 for the 95% confidence bound, denoted as POD_{95}. The 95% confidence bound means that the true POD for a given combination of systematic factors at the evaluated defect size is anticipated to be at least the POD_{95} value for 95% of the cases.

The resulting POD_{exp} and POD_{95} (as well as the 5% confidence bound for completeness) for all defect sizes are subsequently evaluated and curve-fitted to the logistics function, and the resulting POD curves can be plotted as also shown in Figure 3.11. Compared to the plot shown earlier in Figure 3.8, it is clear from the results that with more accurate information on the angle of the sought defect, there is much greater confidence in the detection capabilities of the monitoring system. Since it is known that defects that happen to be in an unfavourable orientation are unlikely to occur, the corresponding poorly performing POD curves can be eliminated; this is evident in the comparison between Figure 3.8 and Figure 3.11. This shows that a more accurate estimation of the detection capabilities can be produced by incorporating the prior information about the sources of uncertainties.

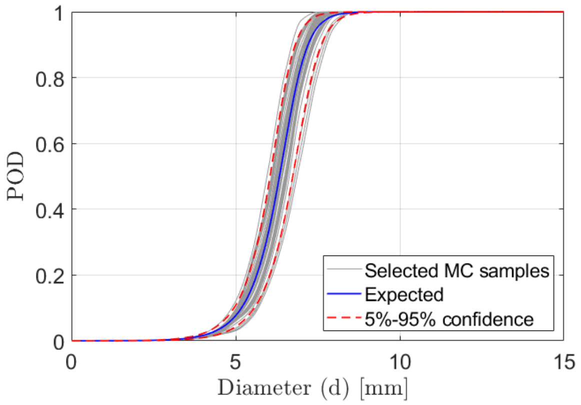

Figure 3.11 Resulting expectation and confidence POD curves considering the distribution of crack orientation together with POD curves from selected samples of defect orientation.

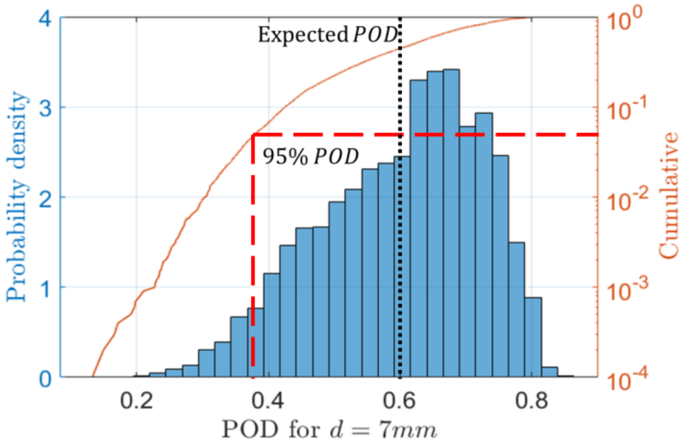

Figure 3.12 Probability density and cumulative function of POD at $d = 7$ mm. The expected POD and 95% confidence POD are shown as a dotted black line and dashed red line respectively.

3.6 Discussion

Overall, the key steps for evaluating the detection capability of PIMS established in this chapter is as follows:

1) Define a nominal configuration of the PIMS used, the component and the type of defect to be detected.
2) Obtain all relevant sources of uncertainties with the use of sensitivity analysis, and categorise their contribution to uncertainty as random or effects. Medium-term effects should be categorised into either categories base on the nature of each individual effect.
3) Evaluate the contribution of random uncertainties and thus obtain the variance in $P(X|\text{no defect})$ and $P(X|\text{defect})$
4) Evaluate the effect of long-term systematic uncertainties on the expected system response using MAPOD or equivalent methods.
5) Combine the effect of random and systematic uncertainties and evaluate the POD of the PIMS for each combination of systematic uncertainties for a chosen PFA.
6) Evaluate the likelihood of each combination of systematic uncertainties occurring based on underlying physics, computational analysis, experiments, or survey of previous experiences.
7) Evaluate the expectation and confidence bounds of POD for the chosen defect size.
8) Repeat Steps 4 to 7 for a range of defect sizes to obtain a POD curve with confidence bounds.

With an established framework for evaluating the detection capabilities for PIMS, quantified plots and metrics can be produced to evaluate the efficacy of PIMS under different engineering applications. This will be useful in comparing between different monitoring system or different configurations of the same monitoring system. Also, by taking into account the statistical distributions of systematic factors of specific applications, decisions in choosing and optimising the use of monitoring systems becomes more effective and better-informed. This will be further studied in Chapter 4, where the well-recognised optimisation of sensitivity and area coverage for PIMS is addressed.

The quantified detection capabilities of PIMS can also be implemented in the assessment of structural integrity of the monitored component. With confidence in how small a defect can PIMS detect, confidence in the useful life of the monitored component can be inferred based on the response of the PIMS. This would clearly illustrate the benefits of using PIMS from the point of view of managing the life cycle of engineering components; this will be studied later in Chapter 5.

The example problem used in this chapter only considers the effect of one systematic factor, whereas in practice it is very likely that many more systematic factors would significantly affect the detection capabilities of PIMS. As a result, research into more advanced methods of efficient sampling and modelling would be required for these studies to be feasible in real-life applications. Recent studies have already been conducted to use more advanced mathematical tools such as the polynomial chaos expansion method for sensitivity analysis and MAPOD studies [112], [113], and the use of similar methods may be implemented into the use of evaluating the detection capabilities of PIMS.

Validating the results obtained from using the framework with experimental studies and subsequently field studies would also be required to demonstrate its use in real-life applications. This will be challenging given the large number of destructive tests on samples with PIMS installed that would be required. While model-assisted methods can reduce the need of experimental studies at earlier stages of development of PIMS, experimental and field studies are inevitably needed for successful implementation of PIMS in real-life applications to provide confidence in the capabilities of PIMS under realistic operating conditions.

3.7 Conclusions

To sum up, a framework for evaluating the detection capabilities for PIMS has been established, forming the foundations of quantifying the benefits of using PIMS for structural integrity assessments. The framework builds upon existing methodologies used with NDE inspections, including the ROC analysis and MAPOD studies. The framework deals with sources of random and systematic uncertainties and incorporates statistical distributions of the systematic factors when evaluating the confidence in the detection capabilities of PIMS. The framework is demonstrated with a hypothetical example of detecting a penny-shaped crack in a steel block using a potential drop monitoring system. This established framework will be used in the following chapters to compare between different monitoring systems or configurations of the same monitoring system, and also to implement results from PIMS for structural integrity assessments.

4 Structural integrity-informed approach to optimising sensitivity and area coverage for permanently installed monitoring systems

4.1 Introduction

This chapter builds upon the established framework in Chapter 3 to address the spatial aspect of the detection capabilities of PIMS. In contrast to manual NDE inspection techniques which usually rely on the ability to manipulate the sensor position and pseudo-optimise sensor location to possible defects, PIMS may be positioned in a sub-optimum location with respect to the sought defect. The detection capabilities will be determined by the location-specific sensitivity of the measurement to the defect at the given location, but the location of the emerging damage is unlikely to be known precisely or be predicted deterministically and so it is necessary to use a probabilistic approach. The anticipated location of damage may be predicted from past experience or surveys, or predicted based on structural considerations such as distributions of stresses. Such a probabilistic approach is consistent with the aim of estimating a probability of detection.

The effect of defect location on the detection capability of PIMS has been studied in previous literature [114], and is similarly studied as an optimisation problem for sensor network placement in structural health monitoring [115], [116]. However, to the knowledge of the author, a unified approach that combines this information with structural integrity information on the probability of defect location has yet to be developed.

It is proposed that the framework established in Chapter 3 can be used to produce, for a specific sensor-component combination, standardised visualisations and metrics that characterise the detection capability of PIMS which takes into account the confidence in defection location obtained from structural integrity information. The proposed approach is composed of three main stages:

1) Evaluating the spatial distribution of probability of detection (POD map);
2) Evaluating the spatial probability of defect location (PDL map);
3) Combining the steps 1 and 2 to evaluate the overall anticipated detection capabilities.

The three stages are consistent with the methodology laid out in Chapter 3, corresponding to steps 1 to 5, step 6 and step 7 of the framework respectively.

The use of the established framework will be demonstrated with illustrative numerical studies of example sensor and component combinations. In structural health monitoring, there is a well-recognised compromise between area coverage and sensitivity. Sensors may interrogate either a small inspection volume and therefore have high sensitivity to any changes within that volume, or interrogate a larger volume which inevitably leads to a reduction in sensitivity. The choice of design point within this compromise is clearly dependent on the confidence in defect location and in turn the required area coverage. The illustrative examples are chosen as they show how the framework may be used to quantify the detection capabilities of a sensor-component combination and how to address the well-recognised compromise between area coverage and sensitivity.

This chapter will be structured as follows. The example problems used for illustration are first described in Section 4.2. The process of obtaining the spatial detection capability of PIMS is demonstrated in Section 4.3. The process of obtaining the probability of defect location is demonstrated in Section 4.4. Results of combining the two to quantify the detection capabilities of the combinations of sensor and components are then presented and discussed in Section 4.5. Evaluation and discussion of the detection capabilities of sensor-component combinations as a function of defect size is presented in Section 4.6. Finally, a discussion and summary of findings is provided in Section 4.7 and 4.8.

4.2 Description of examples problems

Two structural problems are presented, together with two separate example PIMS, giving a total of four sensor-component combinations. The two structural examples are a rectangular beam undergoing three-point and four-point fatigue bending. These examples were chosen due to it being simple to model, and that they are representative of cases where there is a high and low confidence in the location of damage respectively. A bulk-wave ultrasonic sensor is suggested as an example with high sensitivity but low area coverage, and a potential drop sensor is suggested as an example with lower sensitivity but higher area coverage.

The examples described here are hypothetical and are chosen to best illustrate the value of using the proposed framework for quantifying the performance of a PIMS for different operating conditions. More realistic models of monitored components and sensors may be substituted. This section describes these examples in more detail to further elucidate the challenge before the framework is described in the following section.

4.2.1 Description of example structural problems

Two beams, each with dimensions shown in Figure 4.1, are to be exposed to either three- or four-point fatigue bending with equal maximum stress amplitude and load ratio, $R = 0$, meaning that the top surface is always in axial-compression while the bottom surface is always in axial tension. The surface axial stress distributions along the length of the beams are shown schematically in Figure 4.2. The triangular stress amplitude distribution of the three-point bending example indicates that the maximum stress amplitude is experienced only at the centre of the beam, whereas the trapezoidal stress distribution of the four-point bending example indicates the maximum stress amplitude is nominally uniform between the two loading points. The two cases therefore represent scenarios where the area over which damage is expected to initiate is small and large respectively. Assuming that the defect will occur on the surface of the component experiencing tension, we can expect the damage to initiate close to the centre line of the component in the three-point bending case, whereas we can expect the damage to initiate anywhere in the uniformly stressed section between the two loading points in the four-point bending case. The distribution of probability of damage location will be quantitatively assessed in Section 4.4.

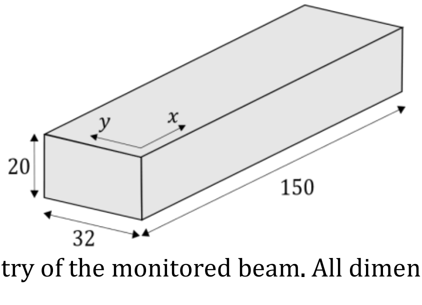

Figure 4.1 Geometry of the monitored beam. All dimensions in mm.

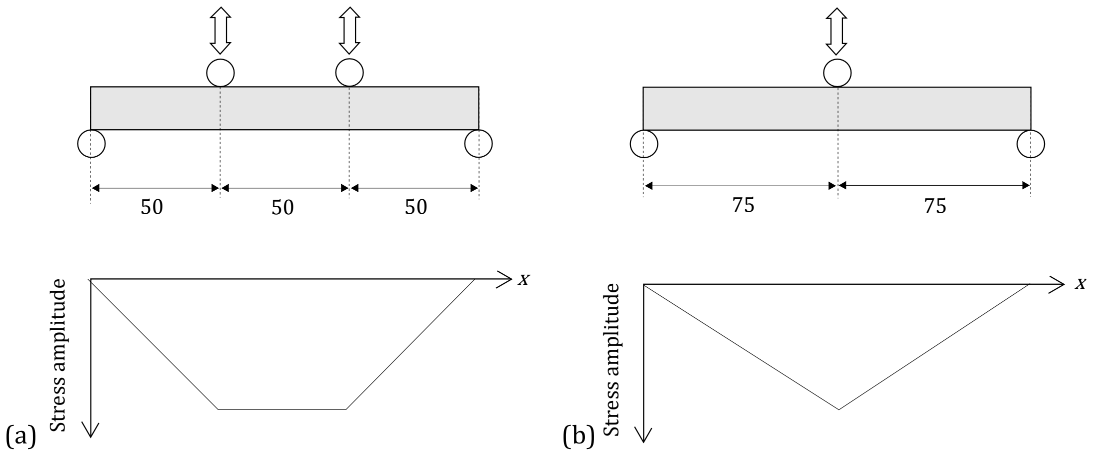

Figure 4.2 Loading conditions and a schematic stress amplitude distribution of the bottom surface of the beam under (a) three-point fatigue bending , and (b) four-point fatigue bending. All dimensions in mm.

4.2.2 Description of example PIMS

Two PIMS were considered and modelled numerically: a bulk-wave ultrasonic sensor and a potential drop sensor. The modelled ultrasonic sensor is schematically illustrated in Figure 4.3. A 45° ultrasonic shear-vertical wave is created by coupling a 25 mm diameter transducer to a 36° Perspex wedge which is fluid-coupled to the monitored component. In the numerical model of this study, this was modelled as phased out-of-plane point forces on the top surface of the block. The reflected signal is then evaluated by summing the phased surface displacements at the same points where the signal is excited.

The ultrasonic sensor is positioned so the ultrasonic beam is parallel to the long axis of the component and the centre of the ultrasonic beam is coincident with the centre of the bottom surface of the component. The excitation signal was a 5-cycle Hanning-windowed toneburst at a centre frequency of 1 MHz. The presence of a defect would reflect the signal back to the transducer, the amplitude of the reflected signal is dependent on the size and location of the defect and is used to indicate the presence of a defect.

The potential drop sensor is schematically illustrated in Figure 4.4. Similar to the monitoring system used in Chapter 3, current injection and sensing electrodes are placed at the two ends of the beam. By monitoring the injected current and resulting voltage the transfer resistance can be calculated. The presence of a defect would deflect current flow in the beam, resulting in an increase in resistance. The expected increase in resistance is again dependent on the size and location of the defect and is used as an indication of whether a defect is present.

The ultrasonic and potential drop sensors are chosen to represent sensors of high sensitivity and low area coverage, and a sensor of low sensitivity and high area coverage respectively.

One could imagine the ultrasonic sensor would be very sensitive to defects at the centre of the beam where the ultrasound is interrogating, while having negligible sensitivity to defects near the sides and ends of the beam. Conversely, the potential drop sensor would have a reasonably uniform sensitivity across the whole surface of the beam. This will be demonstrated and quantified in the following section.

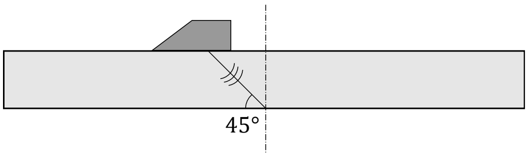

Figure 4.3 Schematic of the permanently installed bulk-wave ultrasonic senor evaluated for monitoring.

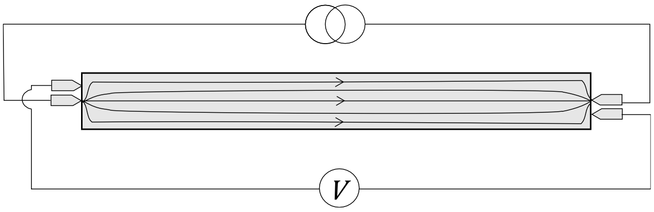

Figure 4.4 Schematic of the permanently installed potential drop senor evaluated for monitoring.

4.3 Obtaining the spatial POD maps of the PIMS (Steps 1 to 5)

The detection capabilities of the two example sensors will now be evaluated using the proposed framework outlined in Chapter 3. This section covers the analysis of the POD of the PIMS, which corresponds to steps 1 to 5 in the framework. The outcomes of this section are spatial POD maps for the two PIMS, which illustrates the POD of the PIMS with respect to where the sought defect is located.

Step 1: Defining a nominal configuration of the component, defect type and PIMS

The first step is to define and model a nominal configuration of the component, defect type and PIMS. The monitored component is defined earlier in Section 4.2.1. For simplicity in modelling, the sought defect is defined as a smooth, square crack-like notch having zero axial extent with sides of length, a, and is orientated normal to the length of the beam. A schematic illustration of this is shown in Figure 4.5. The nominal sensor configuration was described earlier in Section 4.2.2. A defect length of $a = 6$ mm will be used in this section for illustration. The effect of varying defect location is the focus of this study and will be evaluated in Step 4. The effect of varying defect size will be discussed later in Step 8.

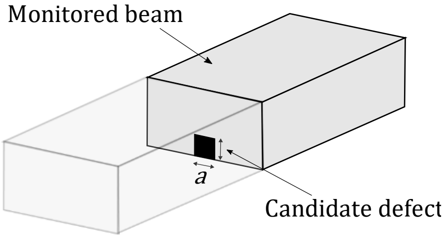

Figure 4.5 Schematic of the cross-section of the beam and the candidate defect modelled in this study.

The outputs of the two sensors considered, X_{UT} and X_{PD}, are defined as follows. For the ultrasonic sensor, this would be the maximum amplitude of the reflected signal obtained with the Hilbert transform. For clarity, the signals are normalized to the case where the defect spans the entire cross section of the beam (i.e. a corner-echo reflection). X_{UT} would therefore nominally be zero when the beam is defect-free, and $X_{UT} = 1$ would nominally be the maximum output of the ultrasonic sensor. Example input and output signals of the ultrasonic sensor are illustrated in Figure 4.6. For the potential drop sensor, the measured resistance is normalized to the resistance measured when the component is defect-free; the signal output is the normalized resistance minus one.

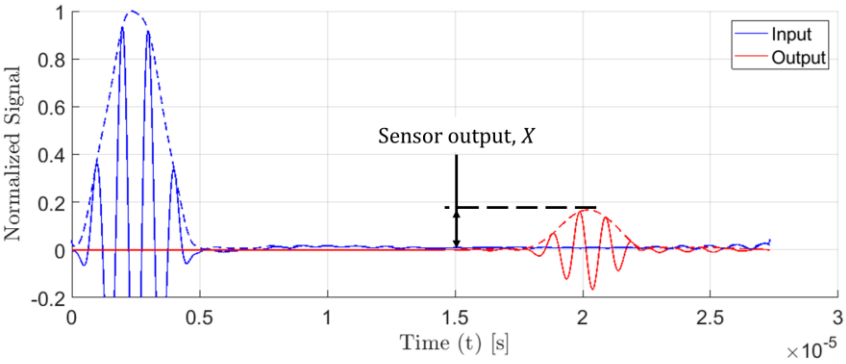

Figure 4.6 Sample signal of the ultrasonic sensor from finite element simulations to illustrate the sensor output.

Step 2: Defining sources of uncertainty in measurements

The aim of this study is to investigate the process of optimising between area coverage and sensitivity. It is clear even without a formal sensitivity analysis that the POD of the ultrasonic sensor would be highly dependent on the defect location given its limited field of view. Hence, for simplicity and clarity of focus, only the variation in signal output as a result of defect location and random noise will be incorporated. Evidently, random noise will contribute to the random uncertainty and defect location will contribute to the systematic uncertainty. In practice, the evaluation of more parameters is almost certainly required, and the appropriate choice of uncertainties to incorporate in the analysis can be determined with parameter sensitivity analysis methods.

Step 3: Evaluating the contribution of random uncertainties

In the present study, the signal output of an ultrasonic sensor, X_{UT}, is assumed to follow the Rice probability distribution,

$$X_{UT} \sim Rice(\bar{X}_{UT}, \sigma_{UT}) \qquad \text{Eq. 4.1}$$

where $\bar{X}_{UT}$ is the expected sensor output as evaluated in the following section, and σ_{UT} is the shape parameter of the distribution as a result of noise signals backscattered from microstructural inhomogeneities [117]. A value of 0.01 is chosen for the shape parameter in this study as evaluated from the results in [118]. This is an approximation of the typical capabilities of ultrasonic measurement systems; in practice, this should be determined accordingly with the actual monitoring system used under its operating conditions.

Similar to Chapter 3, the measured change in normalized resistance of the potential drop sensor, X_{PD}, is assumed to follow the normal distribution,

$$X_{PD} \sim Normal(\bar{X}_{PD}, \sigma_{PD}) \qquad \text{Eq. 4.2}$$

where $\bar{X}_{PD}$ is the expected sensor output as evaluated in the following section and σ_{PD} is the standard deviation, assumed to be 2.8×10^{-4}.

Step 4: Evaluating the contribution of systematic uncertainties

By running multiple finite element simulations where the candidate defect is moved to different positions, the expected signal outputs, $\bar{X}_{UT}$ and $\bar{X}_{PD}$, may be evaluated. The simulations for the ultrasonic sensor were conducted using the finite element software Abaqus; the simulations for the potential drop sensor were conducted using the finite element software COMSOL Multiphysics. By interpolating the results of the simulations at selected points, a map of expected signal outputs for both sensors is populated as shown in Figure 4.7. As mentioned in Section 4.2.1, only defects initiating from the bottom of the beam are considered in this analysis.

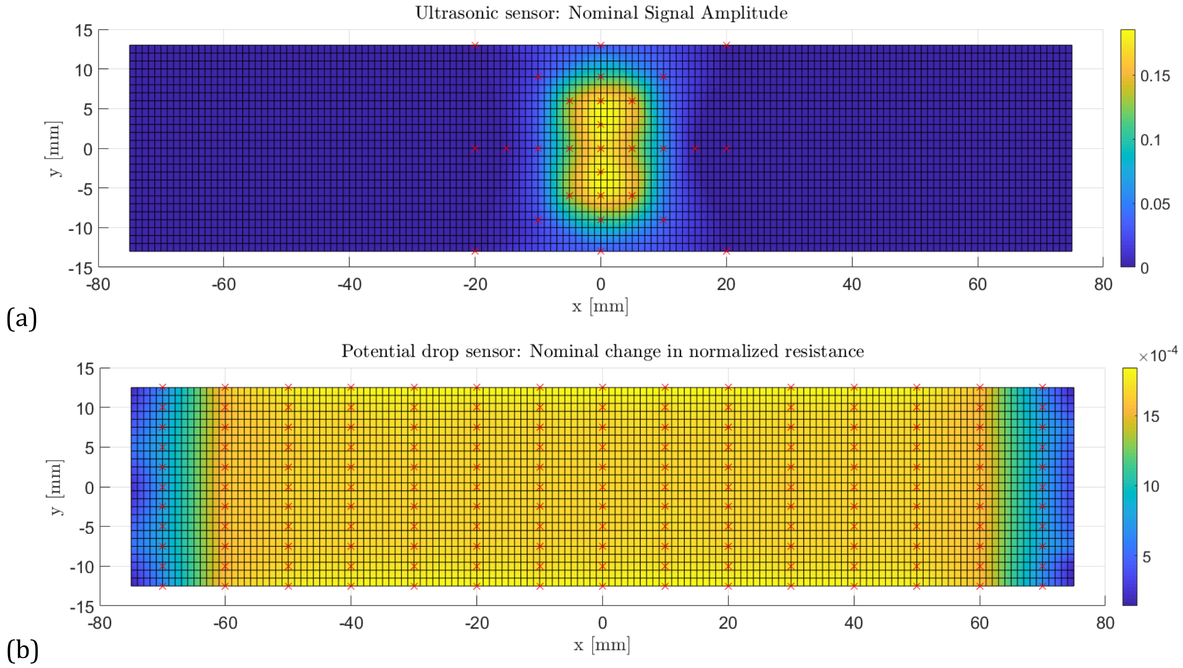

Figure 4.7 Maps showing (a) the nominal signal amplitude of the ultrasonic sensor, and (b) the nominal change in normalised resistance of the potential drop sensor for a 6 × 6 mm defect. The red crosses indicate points where FE simulations are conducted; all other values were interpolated or extrapolated.

Step 5: Evaluating the POD of the PIMS for each combination of systematic uncertainties

With the effect of random and systematic uncertainties evaluated, distributions of the signal output of the PIMS, $P(X|\text{no defect})$ and $P(X|\text{defect})$, can be produced. With this, ROC analysis can be used to evaluate the POD of the for an acceptable PFA. A PFA of 10^{-6} is used in this study, which is significantly lower than what is typically used with NDE inspections. This is needed for PIMS since frequent measurements are made, resulting in more possibilities for a false alarm to occur. For instance, if a PFA of 10^{-3} is chosen, it is expected that a false alarm would occur if 1000 measurements are made.

Also note that for the ultrasonic sensor, the output contains a vector of p data points, and a false alarm is defined as *any* of the output data points greater than the threshold. Hence, the PFA of the ultrasonic sensor can be approximated by De Morgan's law [119],

$$PFA = 1 - (1 - f)^p \qquad \text{Eq. 4.3}$$

where f is the probability of a single data point being above the threshold given there is no defect.

By performing the ROC analysis as described in Section 3.3 for defects at different locations, the spatial POD map for the sensors can be produced. The results of the two sensors for a 6×6 mm square defect are shown in Figure 4.8. As seen from the results, the ultrasonic sensor has near perfect detection capabilities with POD close to unity at the centre of the beam where the ultrasonic beam is directed. However, the sensitivity quickly diminishes with defects located away from the limited area of ultrasonic interrogation. On the other hand, the potential drop sensor has a relatively even coverage over the entire beam except for the ends of the beam where the electrical current has yet to spread out sufficiently.

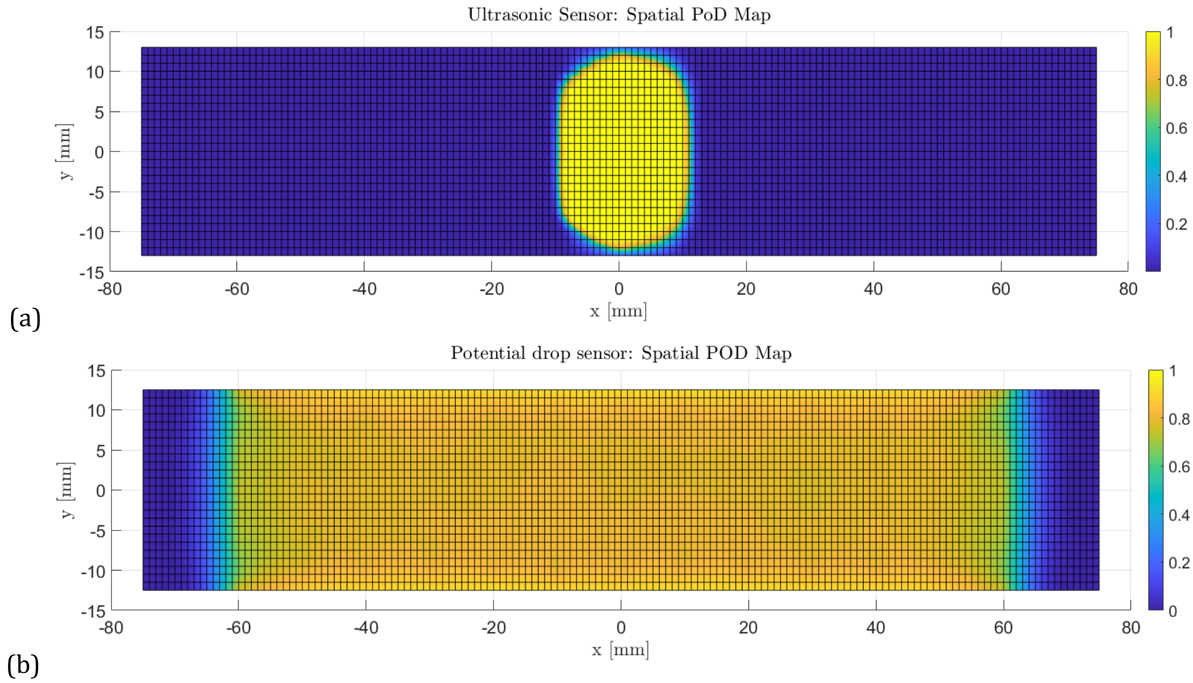

Figure 4.8 Spatial POD Map of (a) the ultrasonic sensor, and (b) the potential drop sensor.

4.4 Probability of defect location maps (Step 6)

Step 6: Evaluating the likelihood of combinations of systematic uncertainties

With the spatial POD map for both sensors defined, the next step is to evaluate the spatial probability of defect location. In real-life applications, the potential defect location on a component is generally not known deterministically. The defect location will be determined by a combination of the externally applied demand on the component resulting in distributions of stress, temperature or environmental conditions, together with the intrinsic material properties and condition of the component [120]. As discussed in Section 2.1, the formation of fatigue cracks depends greatly on the stress and location of microstructural imperfections (e.g. dislocations), which are most likely unknown for an engineering component. Given this uncertainty in where the "weakest link" of the component is, it is necessary to evaluate the location of a damage using a probabilistic approach.

The overall aim is to produce what is defined here as the probability of damage location (PDL) map, which is the map of where a defect is most likely to initiate given there is a defect somewhere on the component. This can be mathematically expressed as,

$$PDL(i) = \frac{P_f(i)}{\sum_{k=1}^{n} P_f(k)} \qquad \text{Eq. 4.4}$$

where $P_f(i)$ is the probability of the defect being present at location i, and n is the total number of discretized locations considered in this analysis.

Several methods can be used to construct the PDL map for the monitored component. Some of these include the use of finite element models, experiments, surveying from previous experiences, or simply the identified inspection zones that are often readily available in practice [121]. In some cases, such as corrosion, it may not be possible to estimate the location of damage, but the length scale of damage will provide an indication of the required spatial coverage [122].

In this study, the weakest-link theory by Weibull [123] is used to evaluate the PDL map. The theory was originally developed to evaluate the effect of specimen size on measured material strength. The method has since been applied to evaluating a range of damage mechanisms such as brittle fracture [124] and provide a non-local stress approach to fatigue assessment [125], [126] with commercially-available software based on the theory [127].

The theoretical analysis of the example problem in the present study using the weakest-link theory is summarized in Appendix A; only the results are shown here. Overall, $P_f(i)$ for fatigue damage is given by,

$$P_f(i) = 1 - \left(1 - \Phi\left(\frac{\ln(N) - C_1 + C_2 \ln\big(S'(i)\big)}{\sigma}\right)\right)^{\frac{A(i)}{A_{ref}}} \qquad \text{Eq. 4.5}$$

where:

- $N =$ number of loading cycles experienced by the component
- $S'(i) =$ stress amplitude with mean stress correction using the modified Goodman relationship [12] experienced by the component at location i
- C_1 and $C_2 =$ material constants for the Basquin law [128]
- $\sigma =$ shape parameter of the lognormal distribution which describes the uncertainty in the Basquin law relationship between $S'(i)$ and N
- $\Phi(\cdot) =$ cumulative distribution function of the standard normal distribution
- $A(i) =$ surface area of discretised location i
- $A_{ref} =$ surface area of the specimen used to determine C_1 and C_2

The parameters used in analysing the sample problem in this study are summarized in Table 4.1. Clearly the parameters selected here are rough estimates, but they provide an indication of the form of the results to expect from the analysis. Results from actual experimental data can be implemented when evaluating applications in real life.

Table 4.1 Material parameters used in this study.

Parameter	Value	Source and remarks
C_1	186	From properties of AISI 1015 in [129]
C_2	9.09	
σ	0.477	Estimated from NUREG/CR–6909 [12]
$A(i)$	$1\ mm^2$	Surface area of an element in FE simulations
A_{ref}	$380\ mm^2$	Surface area of a uniform-gage test specimen recommended in ASTM E-606 [130]

The map of stress amplitude for the two loading cases is produced using 3-D finite element simulations. The maximum stress amplitude for the two cases were set to be equal at 110 MPa (see Figure 4.9 for the stress distribution). This map of stress amplitude is then used to produce the corresponding PDL maps using Eq. 4.5 and values in Table 4.1. The results are shown in Figure 4.10. As expected, the area over which a defect is likely to occur is much greater in the four-point bending case compared to the three-point bending case, meaning that the area which the monitoring system needs to cover is much larger.

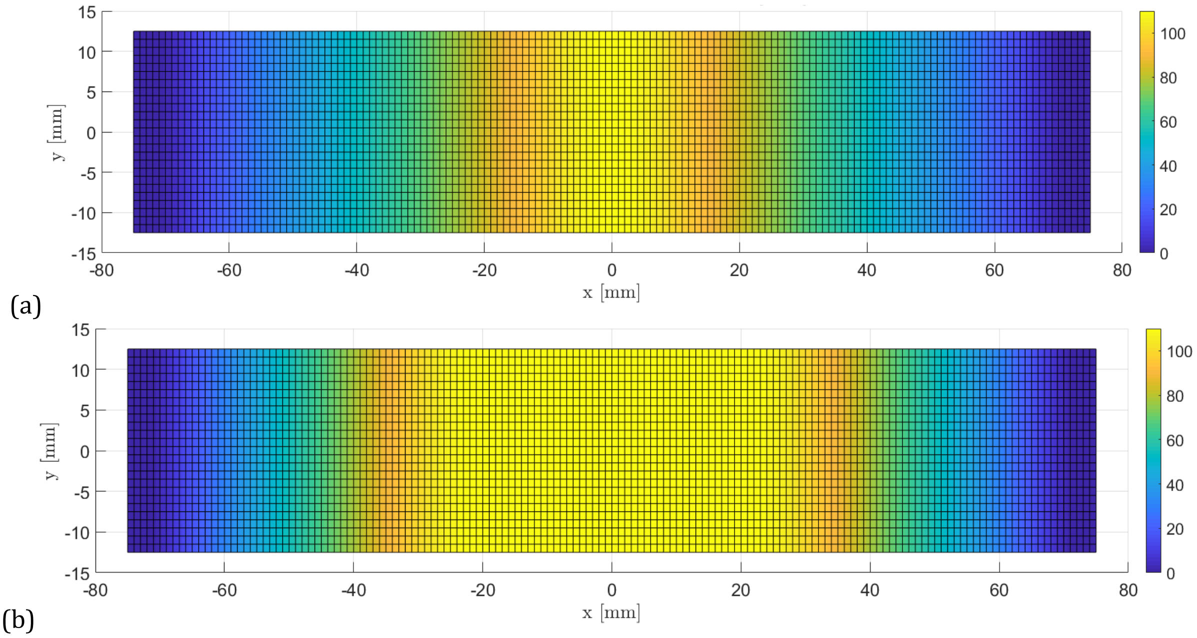

Figure 4.9 Stress amplitude maps (in MPa) for (a) the three-point fatigue bending, and (b) the four-point fatigue bending case.

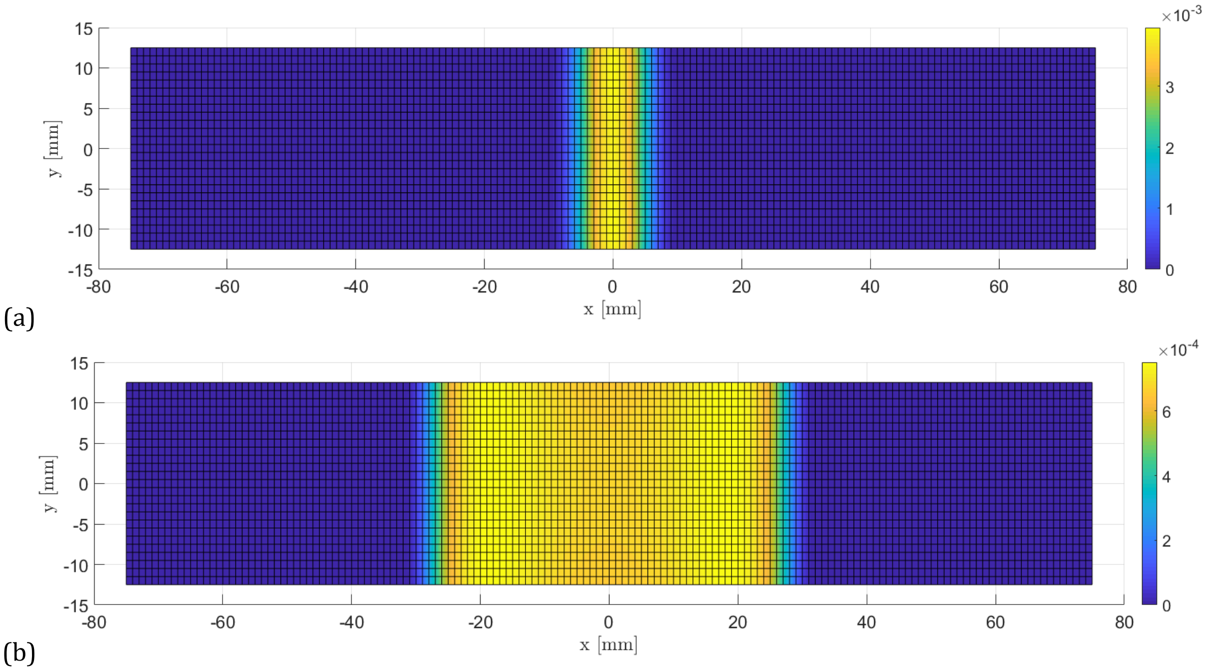

Figure 4.10 PDL maps for (a) the three-point fatigue bending, and (b) the four-point fatigue bending case.

Note that in theory, the PDL map would vary with the number of loading cycles as $P_f(i)$ is a function of the number of loading cycles. This variation is however found to be minimal and therefore insignificant to the analysis demonstrated here; from Eq. 4.5, one could imagine that $P_f(i)$ would steadily increase for all the elements as the number of loading cycles increase and so the normalized $PDL(i)$ remains reasonably constant.

4.5 Overall probability of detection – Combining the POD and PDL map (Step 7)

Step 7: Evaluating the expectation and confidence bounds of POD

With spatial POD maps for the PIMS and PDL maps for the two loading conditions defined, the expectation and confidence in the detection capabilities of each sensor-component combination can be evaluated. A weighted statistical analysis will be used as described in the following section. This is different to the Monte Carlo approach used in Chapter 3, where samples of systematic uncertainties are drawn from predefined distributions and evaluated. The weighted approach used here allows for a direct weighting of the POD of the PIMS at each discretised location on the mapped space. For clarity, the analysis will be described generically in the following section before being applied to the example problem.

4.5.1 Weighted Statistical Analysis

Consider the case where there are n possible mutually exclusive events ($n = 10$ in the illustration in Figure 4.11), each with an index, i, an associated event value, $x(i)$, and probability of occurrence, $P(i)$ (Figure 4.11a). We wish to evaluate the expected event value and the associated confidence.

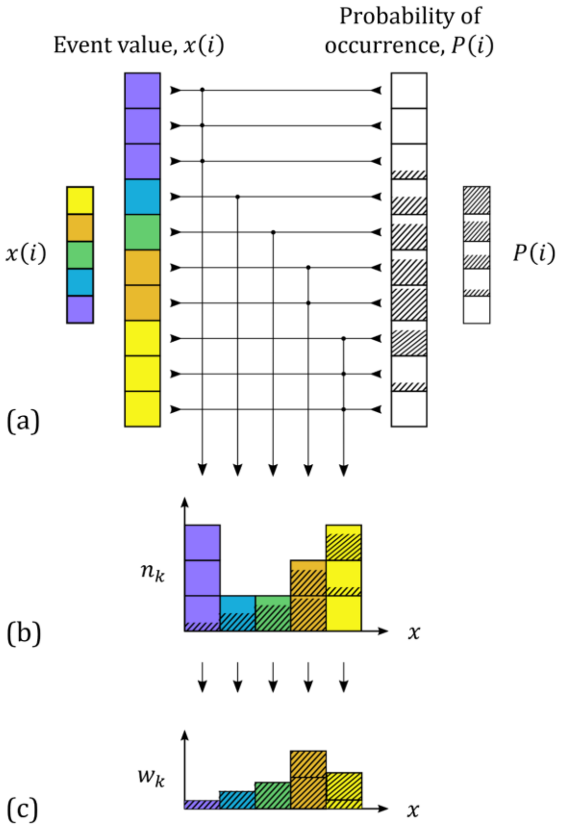

Figure 4.11 Illustration of constructing a weighted histogram. An event space of $i = 1, \ldots, 10$ events is constructed. (a) Each event has a corresponding event value and probability of occurrence. (b) A naïve, unweighted histogram is constructed based on the event values; their corresponding probability of occurrence is also shown, represented by the shaded area. (c) The final weighted histogram weighted according to the corresponding probability of occurrence of each event.

The list of possible event values can be visualised with a histogram (Figure 4.11b). For an unweighted histogram, each event will contribute to one of k bins according to the event value. The resulting height of each bin is simply the number of events in each bin category, n_k; the sum of heights of this histogram would therefore be n.

This histogram cannot be used to accurately evaluate the expected event value and its confidence as it does not include any information on the probability of each event occurring; it would implicitly assume there is an equal probability of the event occurring. To evaluate the expected event value, each contribution to the histogram should be weighted according to its corresponding probability of occurrence, producing what is known as a weighted histogram [131]. The height of each bin in the weighted histogram, w_k, can be calculated by summing the probability of occurrence associated with each individual contribution to the histogram,

$$w_k = \sum_{i=1}^{n_k} P_k(i) \qquad \text{Eq. 4.6}$$

where $P_k(i)$ is the probability of event i in bin k (Figure 4.11c). The sum of heights of this histogram is the sum of the probability of all event and therefore equals unity.

In the context of this chapter, the events in the weighted statistical analysis would be a defect occurring at each discretised location, i, on the monitored component; the event value for each location is the corresponding POD of the permanently installed sensor, $POD(i)$; the probability of occurrence is the corresponding PDL from structural integrity information, $PDL(i)$.

4.5.2 Application to the example problem

The analysis above is applied to the results from the four sensor-component combinations of the example problem; the case of using the ultrasonic sensor to monitor the three-point bending beam to detect 6 × 6 mm defects is used here to illustrate. Results for all four sensor-component combinations and of different defect sizes will be discussed later in Section 4.5.3 and Section 4.6 respectively.

Figure 4.12(a) shows the unweighted histogram normalised to the total number of discretised locations. Figure 4.12(b) shows the weighted histogram together with the weighted empirical CDF where the contribution of POD values at unlikely defect locations are suppressed. The weighted empirical CDF is produced by sorting all $POD(i)$ in ascending order and plotting the corresponding cumulative weights, $PDL(i)$, as a function of POD. Compared to the unweighted histogram, the effect of weighting the histogram with the probability of damage location is most apparent from the disappearance of the peak at $POD = 0$; the $POD = 0$ bin of the histogram was populated by contributions from outside of the region interrogated by ultrasound, but in the three-point bending example the PDL map provides the information that the defect is very unlikely to occur in these low-sensitivity regions and so should be given a low weighting accordingly.

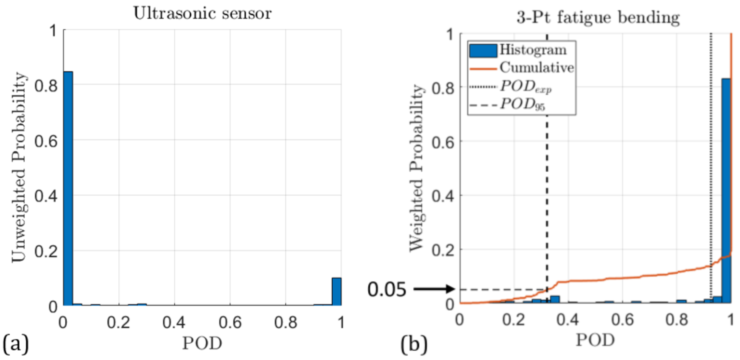

Figure 4.12 Relative frequency histogram of POD_i for the ultrasonic sensor – (a) unweighted, and (b) weighted by the probability of damage location, PDL_i.

Using the weighted histogram and cumulative plot, two metrics of detection capabilities, POD_{exp} and POD_{95} can be evaluated to quantify the performance of a sensor-component combination; this is similar to that discussed in Section 3.5 and are also illustrated in Figure 4.12. Since a weighted statistical analysis is used, methods of obtaining POD_{exp} is slightly different compared to when Monte Carlo methods is used in Chapter 3. Instead of averaging the POD value of all discretised locations, the POD_{exp} is evaluated as the probability-weighted average in probability theory,

$$POD_{exp} = \sum_{i=1}^{n} POD(i) \times PDL(i) \qquad \text{Eq. 4.7}$$

4.5.3 Evaluation of all sensor-component combinations

Using the same method, the detection capabilities of each of the four sensor-component combinations for 6×6 mm defects can now be compared. The graphical results for a 6×6 mm defect are shown in Figure 4.13. A table of POD_{exp} and POD_{95} is shown in Table 4.2.

The histograms for the potential drop sensor are shown in Figure 4.13(b), (d) and (f). Between the naïve unweighted case and the four-point bending case the few low-sensitivity locations at the extreme ends of the component are weighted to zero and the corresponding low POD bins in the histogram are suppressed. The sensitivity over the remainder of the component is relatively uniform, resulting in the cluster of results at around $POD = $ 85-95%; there is little consequence to increasing the confidence in damage location within an already uniform sensitivity. Therefore, there is little uncertainty in the POD and therefore the POD_{exp} and POD_{95} values are in reasonable agreement.

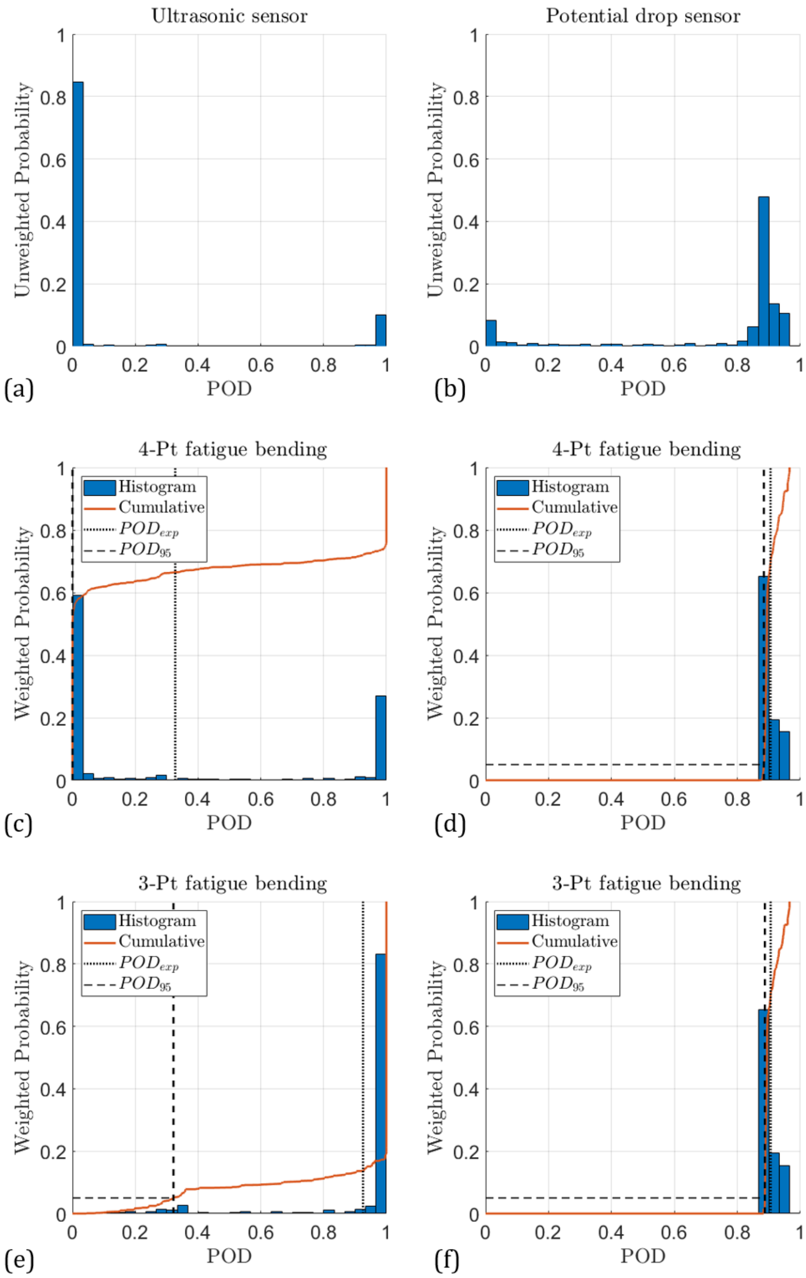

Figure 4.13 Weighted histograms of the POD for 6 × 6 mm defects of the ultrasonic sensor (a, c, e) and the potential drop sensor (b, d, f) for the four-point (c, d) and three-point (e, f) bending case. The unweighted histograms (a, b) are also plotted for comparison.

Table 4.2 PoD_{exp} and PoD_{95} for all four of the sensor-component combinations for 6 × 6 mm defects. Results are for $PFA = 10^{-6}$.

	Ultrasonic sensor		Potential drop sensor	
	POD_{exp}	POD_{95}	POD_{exp}	POD_{95}
Four-point fatigue bending	32.7%	0%	90.5%	88.4%
Three-point fatigue Bending	92.5%	32.1%	90.6%	88.8%

Due to the bi-modal nature of the ultrasonic sensor histogram as shown in Figure 4.13(a), there is a great deal of uncertainty in the POD; depending on the location of the damage the POD will either be near-zero or near-unity. As the region where a defect may be expected to occur gets successively smaller between the naïve, four-point and three-point cases, increasingly many low-sensitivity locations are weighted to zero and the corresponding $POD = 0$ peak gets increasingly suppressed. Despite this, for both the three-point and four-point structural cases, there remains enough possibility that a defect will occur in a low-sensitivity region that the POD_{95} value is poor; even in the three-point bending case there is a 5% chance that the POD will be less than 32.1%.

The results in Table 4.2 indicate the importance of evaluating the expectation and confidence in POD. For the three-point bending case, based on the expected value the ultrasonic sensor appears to outperform the potential drop sensor. Conversely, the POD_{95} values indicate that for the ultrasonic sensor there is a significant possibility that a defect may occur in a poor sensitivity region and therefore may go undetected, whereas this is unlikely for the potential drop sensor due to the greater area coverage. The POD_{95} results significantly penalise sensor-component combinations where there is insufficient area coverage. This can be visualised by plotting the map of $[1 - POD(i)] \times PDL(i)$ as shown in Figure 4.14 for the case of monitoring the three-point bending case with the ultrasonic sensor; this map highlights areas of insufficient POD with significant PDL. A wider ultrasonic sensor would reduce the problem of insufficient coverage at the edges as indicated, though the problem would remain for the four-point fatigue bending case.

It is also worth considering the impact of sensor mis-positioning. The improvement in performance is achieved as the region where damage is likely to occur is well aligned with the sensor; if the sensor was not in this location, the region where damage is likely to occur would not align with the sensor field-of-view and the performance would naturally suffer; the high POD elements would be poorly weighted instead of the low POD elements.

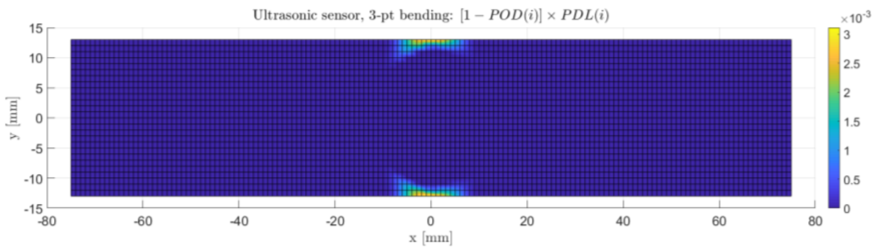

Figure 4.14 Plot of $[1 - POD(i)] \times PDL(i)$ for monitoring the three-point bending case using the ultrasonic sensor, highlighting areas of insufficient sensitivity with significant probability of defect location.

The analysis presented here helps to identify the performance limiting aspects of a permanently installed sensor. For the ultrasonic sensor, despite the very high sensitivity in the interrogated region, clearly the performance is limited by poor area coverage; increasing the sensitivity or reducing the measurement uncertainty (for example by improving the noise performance) is unlikely to cause significant improvement in performance. On the other hand, the potential drop sensor has sufficient area coverage for both structural cases and increasing the area coverage still further will lead to negligible performance increase; in this case the performance is limited by the sensitivity and/or measurement uncertainty.

4.6 Detection capabilities as a function of defect size (Step 8)

The study above can be repeated to evaluate the detection capabilities of different sizes to produce a plot of POD against defect size. Square defects with side length $a = 2$ to 8 mm are evaluated, and the results are shown in Figure 4.15. The expected POD and its 5% and 95% bounds are plotted. It is common to quantify the detection capabilities of a sensor as the defect size for which there is 95% confidence that a POD of at least 90% can be achieved by the sensor; this is often referred to as the $a_{90|95}$ defect size [98], [99]. The $a_{90|95}$ is recognised as being particularly valuable for structural integrity assessments as a metric for the largest defect that may be reasonably assumed to be present and go undetected.

To evaluate the $a_{90|95}$ defect size for each sensor-component configuration, the POD_{95} results are fitted to the logistic function [132]. The resulting $a_{90|95}$ for each sensor-component configuration is shown in Table 4.3. As anticipated, due to the relatively uniform sensitivity of the potential drop sensor there is little uncertainty in the POD and therefore little discrepancy between the POD_{exp} and POD_{95} values. The $a_{90|95}$ achieved for both the three-point bending and four-point bending cases is the same at 6.0 mm. The potential drop sensor is not limited by coverage and thus the increase in POD is in essence solely dependent on the defect size; the larger the defect, the more disruption in current flow is caused and the greater the change in resistance measurement.

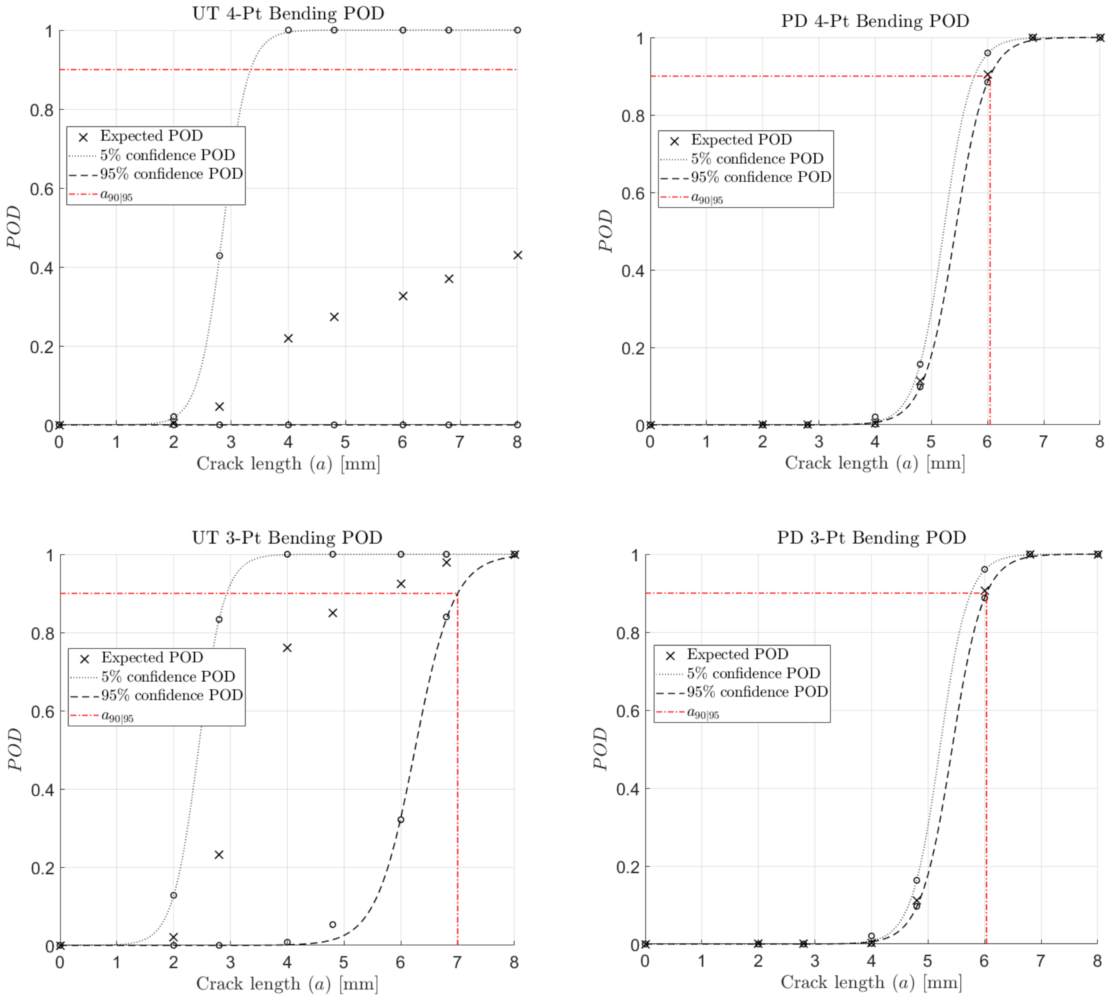

Figure 4.15 Plot of POD against a for the four sensor-component combinations with confidence bounds and the estimated $a_{90|95}$.

Table 4.3 $a_{90|95}$ for all four of the sensor-component combinations.

	Four-point Bending	Three-point Bending
Ultrasonic Sensor	$\gg 8\ mm$	$7.0\ mm$
Potential drop sensor	$6.0\ mm$	$6.0\ mm$

Conversely, there is significant uncertainty in the POD of the ultrasonic sensor and therefore a significant discrepancy between the POD_{exp} and POD_{95} values. The POD_{95} values are poor as a result of the possibility that defects may occur in the regions with very poor sensitivity. For the four-point bending case the POD_{95} value never exceeds zero; if a defect occurs in a location with negligible sensitivity then it will not be detected regardless of its size. This conclusion is subtly different for the three-point bending case, as indicated by Figure 4.14 the locations with inadequate coverage are situated to the sides of the component. Consequently, when a defect increases in size it ‘grows’ into an area of high sensitivity and is therefore detected. Again, a wider sensor would overcome the problem of insufficient coverage for the three-point bending case.

4.7 Discussion of results

Quantitative assessment is necessary to optimise the selection and design of PIMS. It is proposed that the analysis described in this chapter may be conducted for a range of different monitoring system design parameters in order to maximise the $a_{90|95}$ value. In the example problem, the ultrasonic transducer diameter or frequency could be altered in order to achieve sufficient area coverage, without compromising too far on sensitivity. On the other hand, the placement of electrodes of the potential drop sensor may be optimised based on confidence in defect location to improve sensitivity.

In the examples used in this chapter, finite element structural analysis and the weakest link theory is used to provide a probability of damage location specific to each discretised spatial location. It is worth emphasising that on many occasions such involved analysis is not required. For simple problems such as the example problems in this chapter, dividing the component into uniform domains of 'likely' and 'unlikely' areas for damage location would have little consequence on the conclusions; in the three-point bending case the 'likely' areas would correspond to an element wide strip down the centre of the component, while for the four-point bending case the 'likely' area would be between the two central supports. The difference in the results of POD_{exp} and POD_{95} for the example problem would have been within 5% compared to the more comprehensive study using finite element simulations and the weakest link theory.

This chapter focusses on the spatial aspect of POD and does not exploit the ability of a permanently installed sensor to collect frequent, real-time data, which may significantly improve its detection capabilities; the analysis presented here is only based on isolated measurements. The benefits of collected real-time data from the point of view of life cycle management of fatigue-prone components will be explored in the following chapter.

4.8 Conclusions

The spatial aspect of the detection capabilities of PIMS is addressed using the proposed framework in Chapter 3. The map of sensor sensitivity is combined with the map of probability of defect location to evaluate the detection capabilities of PIMS for a specific application. The spatial map of probability of detection is evaluated using a model-assisted approach in this study. The map of probability of defect location is evaluated using a finite element-based weakest-link approach. There are many other methods for estimating the probability of defect location; these range from simple segmentation into 'likely' and ‘unlikely’ areas of defects arising, to more quantitative structural mechanics-based assessments.

Illustrative examples have been used to demonstrate the value of using the framework established in Chapter 3 to address the well-recognised area coverage sensitivity compromise. Histograms of POD are suggested to be particularly valuable in evaluating the performance of the monitoring system, and when coupled with the spatial maps of POD and PDL can help identify the performance limiting design aspects.

Key performance parameters such as POD_{exp}, POD_{95} and $a_{90|95}$ have been suggested and evaluated. The $a_{90|95}$ is recognised as being particularly valuable for structural integrity assessments as a metric for the largest defect that may be reasonable assumed to be present and go undetected. Quantifying performance is necessary to be able to optimise monitoring system design, and tailor it to the specific needs of the structural integrity assessment and subsequently life-cycle management of engineering components as will be demonstrated in the following chapter.

5 Life-cycle management of engineering components incorporating data from permanently installed monitoring systems

5.1 Introduction

The previous two chapters provided methods to evaluate the detection capabilities of PIMS. The aim of this chapter is to propose a framework to integrate the uncertainty quantified PIMS data into a probabilistic structural integrity assessment to aid the life-cycle management of fatigue-prone engineering components.

To date, the life cycle of an engineering infrastructure or plant is usually managed by a combination of structural integrity assessments and regular manual NDE inspections. The typical life-cycle management of an engineering component is summarised in Figure 5.1(a). At regular intervals during service of a component, an NDE inspection is carried out to ensure no defects exceeding a certain critical size are present (a negative inspection result). Following a negative inspection result the fitness-for-service (FFS) is evaluated by postulating the existence of 'the largest defect that might be missed' and forecasting its growth. Clearly, 'the largest defect that might be missed' is determined by the reliability of the detection capabilities of the inspection or monitoring system. The $a_{90|95}$ defect size described in the previous chapter is suggested in [99], but in this chapter the full POD curve will be used. The remaining life of the inspected component is then calculated based on the size of the postulated defect and the crack growth model and parameters. This subsequently provides assurance on the integrity of the component and confidence in its FFS for a calculable period of time.

The availability of regular in-situ measurements from PIMS enables frequent assessments of FFS without manually inspecting the component. The life-cycle management of an engineering component with monitoring is illustrated in Figure 5.1(b) as similarly described in [133]. Notably, incorporating data collected from PIMS has the potential benefit of reducing the need of in-service inspections while ensuring the integrity of the monitored component to the same confidence level. Industrial applications have also shown that the deployment of PIMS is valuable for components that are difficult or hazardous to access and inspect [134].

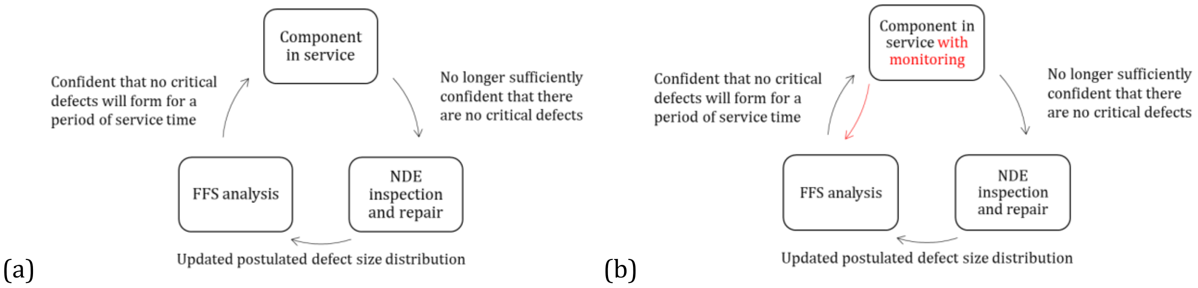

Figure 5.1 Illustration of (a) the typical life-cycle management of a component, and (b) the proposed life cycle management of a component with the availability of monitoring data.

In this chapter, a framework is proposed to integrate data collected from PIMS with probabilistic FFS assessments. The uncertainty quantified POD curves from the previous chapters provide a distribution that may be used to filter out the possibility of a significant defect being present. It is then proposed that particle filtering methods (also known as sequential Monte Carlo methods) can be used to recursively update the possible defect extent of the monitored component and subsequently its FFS. With each successive negative result, the possibility of a significant defect being present is filtered based on the detection capabilities of the PIMS, expressed in the form of a POD curve. This results in an updated distribution of postulated defect sizes, which then feeds into a probabilistic FFS analysis to forecast the evolution of the postulated defects. The postulated defect size distribution is then used to forecast the defect evolution, which in turn is used to predict the probability distribution of failure time. In this way a real-time probabilistic assessment of FFS can be evaluated.

This chapter is structured as follows. A description of an example problem that is used to demonstrate the proposed framework is first provided in Section 5.2. The theory of particle filtering methods that is proposed for postulated defect size updating and evaluating the confidence in FFS will be described in Section 5.3. The proposed approach is then applied to the example problem, with the results being discussed in Section 5.4. Finally, a discussion on the results and conclusions are presented in Section 5.5 and Section 5.6.

5.2 Description of example problem

To illustrate the benefits of incorporating data collected from PIMS into life-cycle management, a hypothetical example of a steel pipe undergoing three-point fatigue bending is used. The life cycle of the pipe may be managed by one of two approaches. First is the use of periodic inspections only, second is the use of a combination of PIMS and potentially less frequent inspections. Details of the structural problem, the inspection and monitoring techniques used, and the failure criterion of the example problem will be outlined in this section.

5.2.1 Description of the structural problem

A hypothetical example of managing the life cycle of a welded steel pipe with nominal diameter, $D = 152.4$ mm (i.e. 6-inch) and wall thickness, $t = 11$ mm undergoing three-point fatigue bending is used in this chapter. This example was chosen as results from experimental study on a guided wave crack growth monitoring system is available as published in [135]. A schematic illustration of the sample pipe is illustrated in Figure 5.2. The pipe is welded at the midpoint of the pipe as indicated by the dashed black line in the figure. The pipe is prone to initiation and propagation of a planar thumbnail fatigue crack at the weld where it experiences maximum stress amplitude.

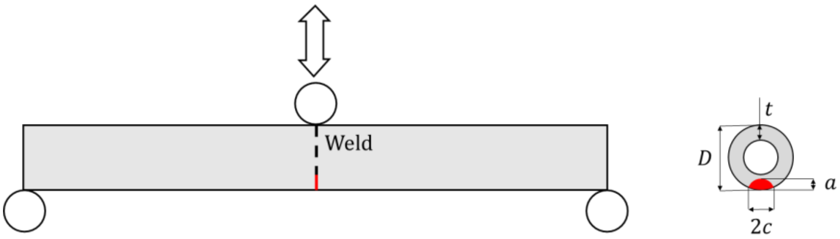

Figure 5.2 Schematic illustration of the welded pipe used in this study. The red line and patch represent the planar thumbnail fatigue crack.

To evaluate the FFS of a component using the damage tolerant approach, a defect growth model is required. As discussed earlier in Section 2.1.2.2, many empirical fatigue crack growth models are available in the literature. The most commonly used Paris' crack growth law with a cut-off at the threshold stress intensity factor is used in this study; any combination of loading and defect size resulting in $\Delta K < \Delta K_{th}$ will not grow. This is consistent with the simplest crack growth model used in the British Standard 7910 [16].

$$\frac{da}{dN} = \begin{cases} C\ (\Delta K)^m, & \Delta K \geq \Delta K_{th} \\ 0, & \Delta K < \Delta K_{th} \end{cases} \qquad \text{Eq. 5.1}$$

$$\Delta K = Y(a)\Delta S\sqrt{\pi a}$$

C and m = Paris' constant and exponent of the material
ΔK = stress intensity range
ΔK_{th} = threshold stress intensity range of the material
a = defect size in the evaluated defect growth direction
$Y(a)$ = geometry factor
ΔS = stress range

As with many other damage mechanisms, fatigue damage accumulation is stochastic in nature [136]–[139]. In this study, the stochasticity in defect growth is simply represented by a probability distribution of the Paris' constant, C; the Paris' exponent, m, and threshold stress intensity range, ΔK_{th}, are assumed to be known. The values used are also from the British Standard 7910 [16] and are shown in Table 5.1. Clearly this is a simplified model as pointed out in the literature [140]. However, it is believed that this simplified model is sufficient for illustration purposes in this study. A different probabilistic defect growth model can easily be substituted to suit the actual application.

All postulated initial cracks are assumed to be semi-circular (i.e. $a = c$). However, the growth of the semi-circular crack in both the depth, a, and width, c, direction needs to be evaluated. The same defect growth model is used for evaluating the defect growth in both directions; the difference in growth rate in the two directions is accounted for when evaluating the geometry factor, $Y(a)$, as described in the AFGROW Handbook for Damage Tolerant Design [141].

Table 5.1 Welded steel parameters for the defect growth model used from British Standard 7910 and the AFGROW Handbook for Damage Tolerant Design.

Description	**Parameter**	**Value / Probability Distribution**
Paris' constant	C	$C \sim \text{Lognormal}(\mu = -29.84, \sigma^2 = 0.55)$
Paris' exponent	m	3.11
Threshold stress intensity range [$MPa\sqrt{mm}$]	ΔK_{th}	63
Geometry factor	$Y(a)$	Evaluated from [141] for a given defect size, a

The uncertainty in loading conditions experienced by the component is characterised by uncertainties in stress range, which is said to follow a normal distribution with parameters shown in Table 5.2. Loading is assumed to be fully reversed (i.e. load ratio, $R = -1$). Again, this is a simplified model and the values chosen here are arbitrary to give a fatigue life of order 10^6 cycles with considerable uncertainty in load severity. A more realistic representation of the loading conditions, such as predictions made from inputs of a conditional monitoring SHM system, can be substituted as needed.

Table 5.2 Loading conditions of the component used in this study.

Description	**Parameter**	**Probability Distribution**
Stress range	ΔS	$\Delta S \sim \mathrm{Normal}(\mu = 220, \sigma = 22)$
Load ratio	R	-1, deterministic

With the loading conditions and defect growth parameters defined, defect growth from a crack of given geometry may be modelled and predicted by numerically integrating the crack growth law. A sample result of growing a 1 mm semi-circular crack (i.e. $a = c$) to a through-thickness crack (i.e. $a = t$) with mean values of Paris' constant, C, and stress range, ΔS, is shown in Figure 5.3. The uncertainty in these parameters and the postulated crack length will result in a range of possible defect growth curves; this uncertainty and how it is managed with inspection and monitoring results is the focus of this chapter.

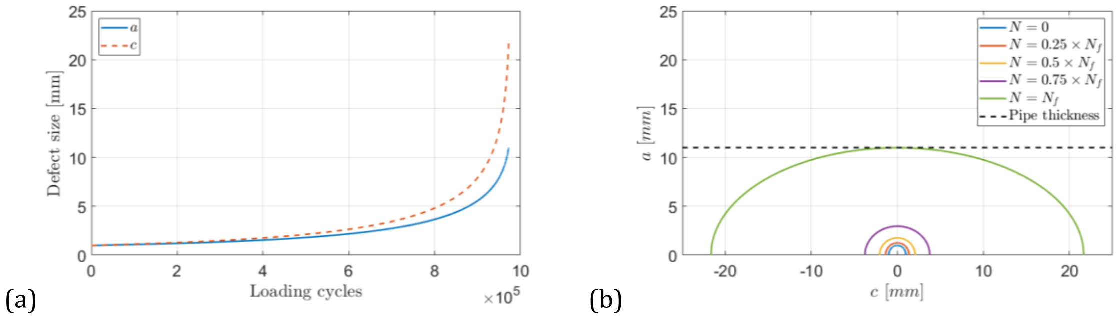

Figure 5.3 Sample result of fatigue crack growth, showing (a) growth in the depth and width direction against the number of cycles; (b) shape of the defect at selected intervals.

5.2.2 Description of the inspection and monitoring schemes

In this hypothetical example problem, an eddy current sensor will be used for periodic inspections, and a permanently installed ultrasonic guided wave sensor will be used for defect monitoring. Descriptions of the setup and detection capability of the two sensors are given below.

5.2.2.1 Eddy current sensor for inspection

An eddy current sensor is used for inspection in this study; an overview on how an eddy current sensor works can be found in [142]. An eddy current sensor was chosen for this study because it is suited for detecting surface-breaking defects, which is ideal for the example problem. The POD curve of the eddy current sensor for a crack-like defect is obtained from existing literature for an eddy current sensor by Mohseni et al. [143] where its detection capabilities are evaluated experimentally with qualified inspectors. The results are fitted to a logistics function and is shown in Figure 5.4. As a metric of detection capability, the eddy current sensor is expected to have a $POD = 90\%$ at $a = 0.95$ mm.

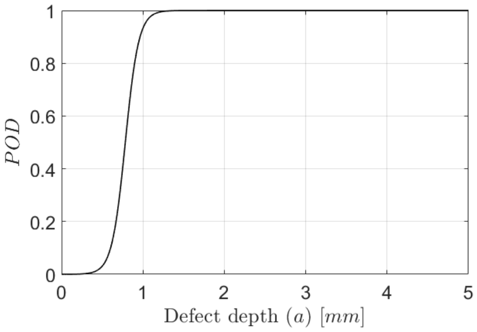

Figure 5.4 POD curve of the eddy current sensor used in this study.

5.2.2.2 Guided wave sensor for monitoring

For defect monitoring, a short-range shear-horizontal guided wave PIMS as described in [135] is used. Basic theory on how guided wave sensors work is described in Section 2.2.3.2. The POD curve of the guided wave sensor is evaluated using a combination of analytical solutions and experimental results produced by Chua et al. [87], [135]. The amplitude of the guided wave signal reflected from a zero axial extent crack-like defect is evaluated analytically, with the results shown in Figure 5.5(a). The amplitude of the signal is represented as a percentage of the amplitude of a pipe-end reflection. The signal noise level is evaluated from a laboratory experiment, which is found to follow a normal distribution with a standard deviation of 0.13% in the case where only one transducer is used as a receiver and no averaging is done. A separate study on the effect of long-term stability of guided wave systems also yielded similar results in terms of signal noise level [144]. Assuming a target PFA of 10^{-6}, a POD curve plotting the probability of detection against defect depth can be produced as shown in Figure 5.5(b). As a metric of detection capability, the guided wave sensor has a $POD = 90\%$ at $a = 3.5$ mm. This is inferior compared to the eddy current sensor used for inspections.

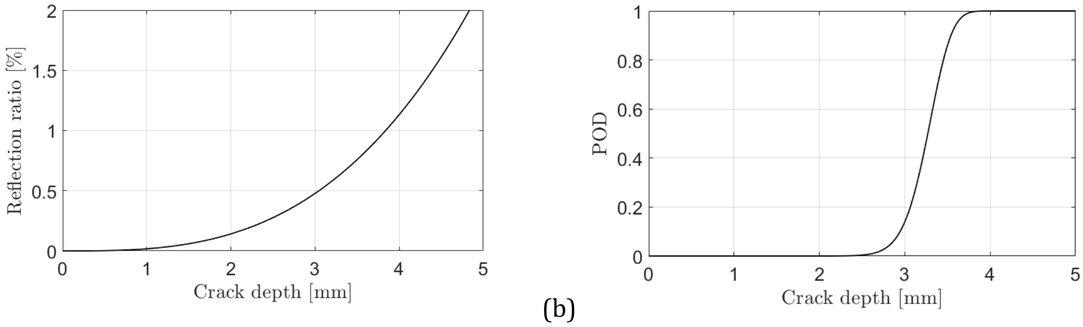

(a) (b)

Figure 5.5 (a) Plot of the reflection ratio of the guided wave sensor as a function of crack depth, and (b) the subsequent POD curve assuming normally distributed noise and $PFA = 10^{-6}$.

5.2.2.3 Considerations in choosing POD curves

Note that the POD curves shown in Figure 5.4 and Figure 5.5 consider all sources of uncertainty as random and are therefore the expected POD curves. It has been shown in the previous two chapters that for PIMS, systematic uncertainty can cause considerable uncertainty in the POD curve that can be represented by showing various curves, such as the expected value curve, the median curve, or a curve representing the bounds of any chosen level of confidence. The choice of which curve to use corresponds to the meaning of the FFS estimate produced. The expected POD curve results in an estimate of the expected FFS, while the 95% confidence bound curve will result in estimates that will be conservative 95% of the time.

Alternatively, a Monte Carlo approach to sample POD curves based on their probability of occurrence can be used to evaluate how the uncertainty in the detection capabilities translate to uncertainty in FFS. Clearly, this approach would require significantly more computational effort. In this Chapter, the expected POD is used in the first instance to illustrate the method, but the possible effect of systematic uncertainty is explored in Section 5.4.3.

5.2.3 Failure criterion, confidence in FFS and inspection opportunities

To conduct a meaningful FFS analysis, a failure criterion would have to be defined. In practice, the failure criterion is either defined as a loss of function such as a leaking pipe, or potential structural failure as discussed earlier in Section 2.1.2.4. With probabilistic analysis, the confidence in FFS of a component, denoted as FFS_C in this study, is defined as the confidence in the component not violating the failure criterion. As an example, assume that the failure criterion is a defect of depth a_{crit} to be present. FFS_c would subsequently be defined as the probability that no defect greater than a_{crit} is present on the component of interest. If our estimated defect depth distribution, $p(a)$, at a given time during service is as illustrated in Figure 5.6, FFS_C at that given time can then be evaluated as $p(a < a_{crit})$.

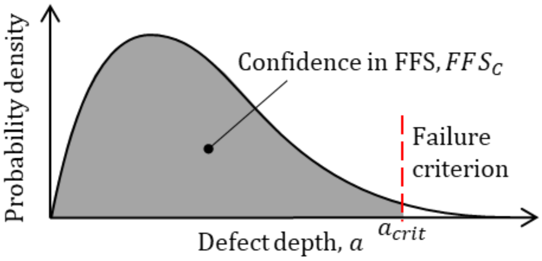

Figure 5.6 Schematic illustration of the definition of failure criterion and confidence in FFS.

Defects that may be present in the component are anticipated to propagate according to the assumed defect growth model. An important aspect of the analysis is to forecast the evolution of the postulated defect size distribution and thus FFS_C with time (or number of loading cycles for fatigue). The solid blue line in Figure 5.7 schematically plots of how FFS_C would typically evolve; as postulated defects are anticipated to propagate with time, FFS_C would subsequently decrease. When the evaluated FFS_C reaches a predefined target value, FFS_{limit}, there is no longer sufficient confidence in the FFS of the component. An inspection would then have to be conducted before FFS_C reaches FFS_{limit} to update $p(a)$. Should the inspection return a negative result, the possibility of a significant defect being present is eliminated and thus FFS_C is improved. In Figure 5.7, an inspection is conducted at time τ_2 to update the FFS_C.

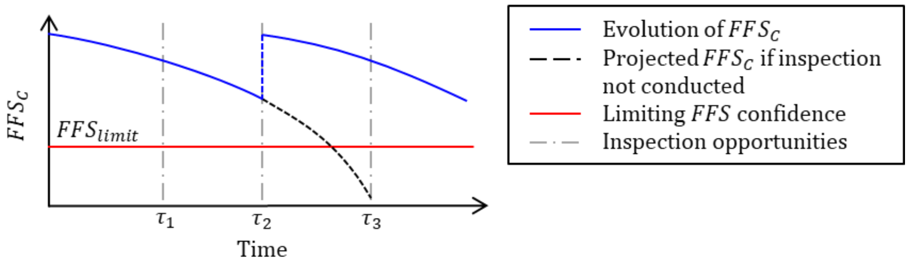

Figure 5.7 Schematic plot of how FFS_C typically evolves with time and updated with inspections.

In reality, it is extremely rare that one gets to inspect the component when FFS_C reaches FFS_{limit} exactly. Typical opportunities to inspect the component are governed by a calendar-based maintenance scheme of the structure. In Figure 5.7, arbitrary opportunities for inspection, τ_1, τ_2 and τ_3, are shown and represented as dot-dash grey lines. Together with the aim of minimising the number of inspections required, the decision to inspect a component would be evaluated based on whether it is necessary to conduct an NDE inspection to ensure FFS_C remains greater than FFS_{limit} before another inspection opportunity arises. Using

Figure 5.7 as an example, at τ_1, the projected FFS_C would remain above FFS_{limit} until the next available inspection opportunity, τ_2. It is therefore not necessary to inspect at τ_1 as there is sufficient confidence in the FFS of the component. However at τ_2, the projected FFS_C of the managed component will fall below FFS_{limit} before τ_3 as illustrated by the dotted black line. It is therefore necessary to inspect at τ_2 in order to be sufficiently confident in the FFS of the component until the next inspection opportunity. The dotted blue line represents the update in FFS_C following an inspection which returns a negative result.

In the example problem used in this study, the pipe is designed to leak-before-break, so the failure criterion is defined as having a through-wall crack in the component while in operation (i.e. $a_{crit} = t$). FFS_{target} is said to be 99.9% in this study. It is assumed that there is an opportunity to inspect the managed component every 10^5 loading cycles. The values chosen here are arbitrary and may be substituted to suit the specific application studied. For instance, inspection opportunities may not occur at regular loading cycle intervals, but rather at specific times regardless of how many loading cycles the component of interest has experienced.

5.3 Updating of defect size distribution and fitness-for-service analysis

In the context of this study, the role of inspections and PIMS is to screen for the presence of defects; the absence of a detectable defect provides assurance on the FFS of the component and consequently the confidence required to continue operation of the component for a period of time. The process of updating the confidence in FFS given results from inspection and/or PIMS proposed for this study is divided into two stages:

1. Updating the defect size distribution using inspection and/or monitoring results
2. Updating the confidence in fitness-for-service using the updated defect size distribution and the probabilistic defect growth model

5.3.1 Updating the defect size distribution using inspection and/or monitoring results

The main aim of this stage is to use single or multiple negative results (i.e. no defects detected) from inspection and/or monitoring to infer what sized defect, a, might be present in the component.

5.3.1.1 Bayesian inference for a single measurement result

We begin by looking into the problem where only a single measurement result is considered. This can be simply evaluated using Bayes' theorem, which in the context of defect size updating would be,

$$p(a|X \leq X_{th}) \propto p(a) \times p(X \leq X_{th}|a) \quad \text{Eq. 5.2}$$

The distribution $p(a)$ is the prior distribution, which describes the estimate of defect size distribution prior to any measurements being made. This may come from sources such as manufacturing standards or previous inspections, or simply a naïve uniform distribution if there is no prior knowledge.

The distribution $p(X \leq X_{th}|a)$ is the likelihood function, which describes the likelihood of the negative result given a defect size. Importantly, this may be expressed in terms of the POD curve, $POD(a)$, of the inspection or monitoring system used as also done in [133]. $POD(a)$ was defined earlier in Eq. 3.1 as the probability of $X > X_{th}$ for a given defect size, a. Thus, the likelihood function for a negative inspection or monitoring result maybe expressed as,

$$p(X \leq X_{th}|a) = 1 - p(X > X_{th}|a) = 1 - POD(a) \quad \text{Eq. 5.3}$$

Finally, the distribution $p(a|X \leq X_{th})$ is the posterior distribution, which is what we want to obtain from the analysis. This gives an updated estimation of defect size distribution based on the inspection or monitoring result.

5.3.1.2 Recursive updating of defect size distribution: a particle filtering approach

The previous section outlined the use of the POD curve to infer possible defect sizes from a single measurement. In practise, multiple inspections are performed, and if PIMS are used, measurements are frequently collected throughout the service life of the component. Each new measurement should inform the possible defect sizes. The process of updating the distribution of defect sizes is not as straightforward as recursively applying Bayes' theorem and using the previously evaluated posterior distribution as the prior distribution for the latest measurement. This is because the size of any potential defect in the component would evolve with time.

As a result, a dynamic state-space modelling approach is required. Particle filtering methods (also known as sequential Monte Carlo methods) are of growing popularity for probabilistic damage prognosis in multiple applications given their flexibility and ease of implementation and will be used in this study [145]–[147]. The theory of particle filtering methods is widely discussed in existing literature; a summary of the method is given here in the context of managing the life cycle of engineering components. The aim is to evaluate the defect size distribution after every N loading cycles given all available inspection and monitoring results. This is expressed as,

$$p\left(a_j|\boldsymbol{M}_{\boldsymbol{0}:\boldsymbol{j}}\right) \quad \text{Eq. 5.4}$$

a_j = Size of defect at the most recent, j-th inspection or monitoring result, where the component has experienced N_j loading cycles.

$\boldsymbol{M}_{\boldsymbol{0}:\boldsymbol{j}}$ = Vector of results of the zeroth to j-th measurement from inspection or monitoring, the zeroth being the initial measurement prior to service (i.e. at $N = 0$). A binary result is considered; either no defect is detected (i.e. $X \leq X_{th}$) or a defect is detected (i.e. $X > X_{th}$).

Step 1: Specify the prior

To initiate the process, a distribution of initial defect size, $p(a_0)$, would have to be defined. In numerous studies on probabilistic damage prognosis using defect growth models, the assumption that a macroscopic defect is already present and detected is often made [148], [149]. Under such conditions, the initial defect size distribution would simply be the measured defect size together with its quantified uncertainty. However, there are also cases where the component of interest is nominally “defect-free”. For such cases, a postulated defect size distribution would have to be used.

There are numerous approaches to postulating the initial defect size distribution. One approach is the use of an equivalent initial flaw size; this approach uses the defect growth model to backward-extrapolate the equivalent initial flaw size such that the evaluated component life matches that evaluated using the stress-life approach; further discussion of this can be found in [150]. Alternatively, the initial defect size distribution can be defined in view of knowledge from “service experience, the manufacturing process, resolution limits of a NDE technique” [17].

In this study, it is assumed that regardless whether monitoring is used to manage the life cycle of the component, an inspection is conducted prior to its service. Therefore, the detection capability of the inspection technique is used to define the postulated initial defect size distribution. Assuming no prior knowledge other than a negative result from the initial inspection, the initial distribution of defect size is evaluated using Eq. 5.2 and Eq. 5.3. This results in,

$$p(a_0|M_0) \propto 1 - POD(a) \qquad \text{Eq. 5.5}$$

where M_0 is the negative result of the initial inspection. Using the POD curve of the eddy current sensor defined in Section 5.2.2.1, $p(a_0|M_0)$ is obtained by normalising the function $1 - POD(a)$ for $a \geq 0$ such that it integrates to unity; the resulting distribution is shown in Figure 5.8. This figure shows the distribution of the size of a postulated defect that may be present in the component given the negative result of the initial inspection. In this example, since it is very likely that the inspection would detect any defect greater than approximately 1.25 mm in depth, a negative result would effectively eliminate the possibility of a defect greater than this size. Conversely, there is little chance the inspection would detect a defect smaller than approximately 0.5 mm in depth, so the inspection provides negligible information on the likelihood of such a defect being present. Thus, the distribution at small defect sizes remain flat since a naïve uniform distribution was used as the prior, $p(a)$. Should a POD curve of a certain confidence bound be used, a level of conservatism in the estimated postulated defect size is introduced. For instance, the 95% confidence POD curve would result in an estimate that is conservative for 95% of the of the combinations of systematic uncertainty realisations.

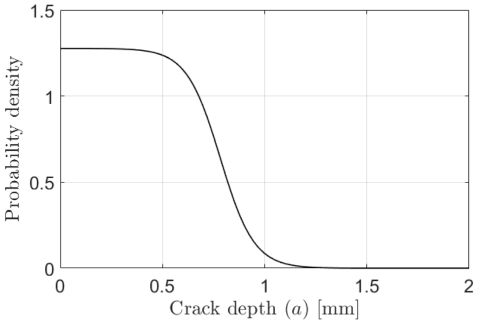

Figure 5.8 Plot of $p(a_0|M_0)$ for the example problem after the initial inspection without any other prior knowledge.

Step 2: Time dependence of defect evolution

Between successive measurements, the postulated defects are assumed to evolve based on the defined defect growth model. As a result, it is necessary to evaluate the evolved distribution of defect size based on the previous measurements before taking into account the most recent measurement.

At the instance where the j-th measurement is made, the previous measurement would be the $(j-1)$-th measurement, and the previously-evaluated defect size distribution would be

$p(a_{j-1}|\boldsymbol{M}_{\boldsymbol{0}:\boldsymbol{j-1}})$. The aim of this step is to evaluate the distribution $p(a_j|\boldsymbol{M}_{\boldsymbol{0}:\boldsymbol{j-1}})$ with the defect growth model. This distribution would act as the prior distribution in the following step when the defect size is updated with the latest measurement results.

A Monte Carlo approach is used to evaluate the evolved defect size distribution. An appropriate sampling method such as the Latin hypercube sampling method [151] used in this study is used to draw $i = 1, \dots, U$ samples from the distribution $p(a_{j-1}|\boldsymbol{M}_{\boldsymbol{0}:\boldsymbol{j-1}})$ and other parameters with uncertainties of the defect growth model (i.e. Paris' constant, C, and stress range, ΔS, in the example problem). Each sample of defect size, $a_{j-1}^{(i)}$, and a set of probabilistic parameters of the defect growth model is then used to evaluate each corresponding $a_j^{(i)}$. This can then be represented as a histogram of evolved defect sizes which approximates the distribution $p(a_j|\boldsymbol{M}_{\boldsymbol{0}:\boldsymbol{j-1}})$. An illustration of evaluating the defect size distribution after 2×10^5 loading cycles for the example problem is shown in Figure 4.9. The prior distribution used is the distribution defined in the previous step. In this example, 2×10^6 samples were drawn from the distributions of defect size and crack growth parameters. From the results, it is clear that a significant portion of the postulated defects have grown in size. Note that a portion of smaller defects did not evolve; this is due to the fact that the combination of defect size and defect growth parameter results in stress intensity is below the growth threshold (see Eq. 5.1).

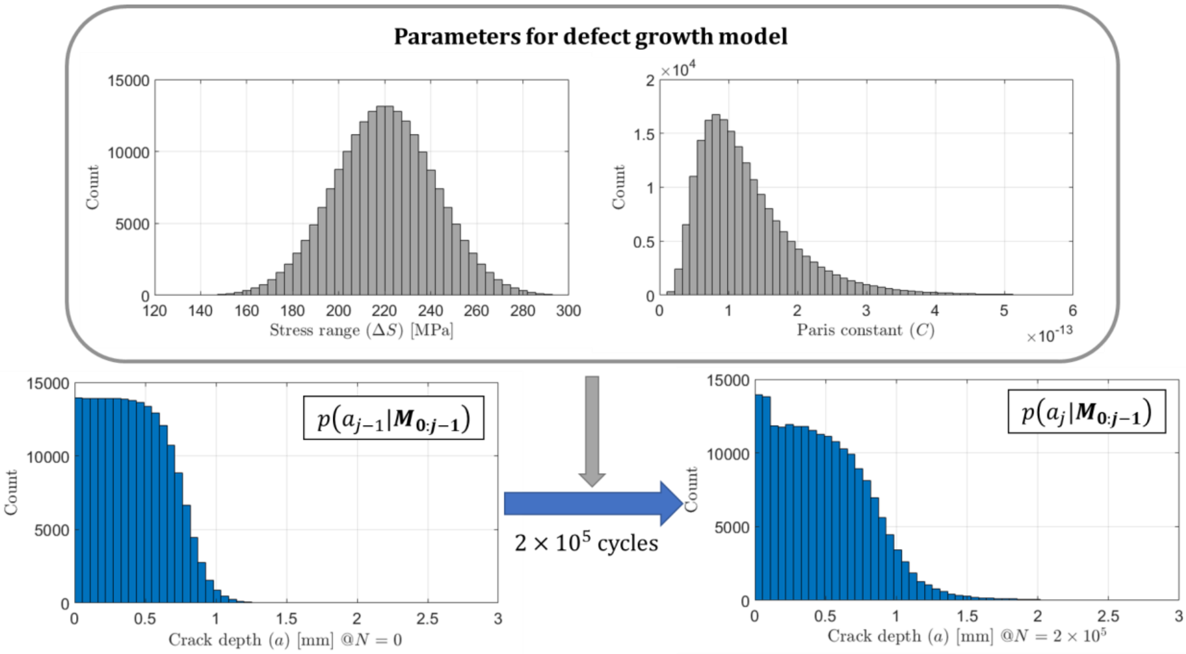

Figure 5.9 Illustration of the process of evaluating the evolution of the histogram of defect sizes sampled from the prior defect size distribution.

Step 3: Particle filtering using the POD curve

With the distribution $p\left(a_j|\boldsymbol{M}_{\boldsymbol{0}:\boldsymbol{j}-\boldsymbol{1}}\right)$ evaluated, the next step is to incorporate the latest measurement result, M_j, and thus obtain the distribution $p\left(a_j|\boldsymbol{M}_{\boldsymbol{0}:\boldsymbol{j}}\right)$. To do so, each sample of $a_j^{(i)}$ is assigned a weight, $w_j^{(i)}$, evaluated as

$$\widetilde{w}_j^{(i)} = w_{j-1}^{(i)} \times p\left(M_j\middle|a_j^{(i)}\right)$$

$$w_j^{(i)} = \frac{\widetilde{w}_j^{(i)}}{\left(\sum_{p=1}^{X} \widetilde{w}_j^{(p)}\right)} \qquad \text{Eq. 5.6}$$

where $w_{j-1}^{(i)}$ is the previously evaluated weight of the particle, and $p\left(M_j\middle|a_j^{(i)}\right)$ is the likelihood function as derived in Eq. 5.3 with the POD curve of the latest measurement. This describes the likelihood of obtaining the latest measurement result if a defect of size $a_j^{(i)}$ is indeed present. With this, the final posterior distribution, $p\left(a_j|\boldsymbol{M}_{\boldsymbol{0}:\boldsymbol{j}}\right)$, that describes the updated postulated defect size given all previous inspections and the current inspection can be approximated as,

$$p\left(a_j|\boldsymbol{M}_{\boldsymbol{0}:\boldsymbol{j}}\right) = \sum_{i=1}^{U} w_j^{(i)} \times \delta\left(a_j - a_j^{(i)}\right) \qquad \text{Eq. 5.7}$$

where $\delta(\cdot)$ is the Dirac delta function.

Following the example in the previous step, suppose an inspection is carried out after $N = 2 \times 10^5$ loading cycles, and thus the POD curve of the eddy current sensor is used for the likelihood function. Illustration of the process for the example is shown in Figure 5.10. A negative result from the inspection filters the probability of a defect that is much larger than the detection capability being present, otherwise the test result is likely to be positive. As seen from the example figure, the likelihood of a negative result becomes negligibly small above around $a = 1.25$ mm. The negative result from the inspection therefore effectively eliminates the largest defect sizes from the prior distribution, $p\left(a_j|\boldsymbol{M}_{\boldsymbol{0}:\boldsymbol{j}-\boldsymbol{1}}\right)$, to produce the updated posterior distribution, $p\left(a_j|\boldsymbol{M}_{\boldsymbol{0}:\boldsymbol{j}}\right)$.

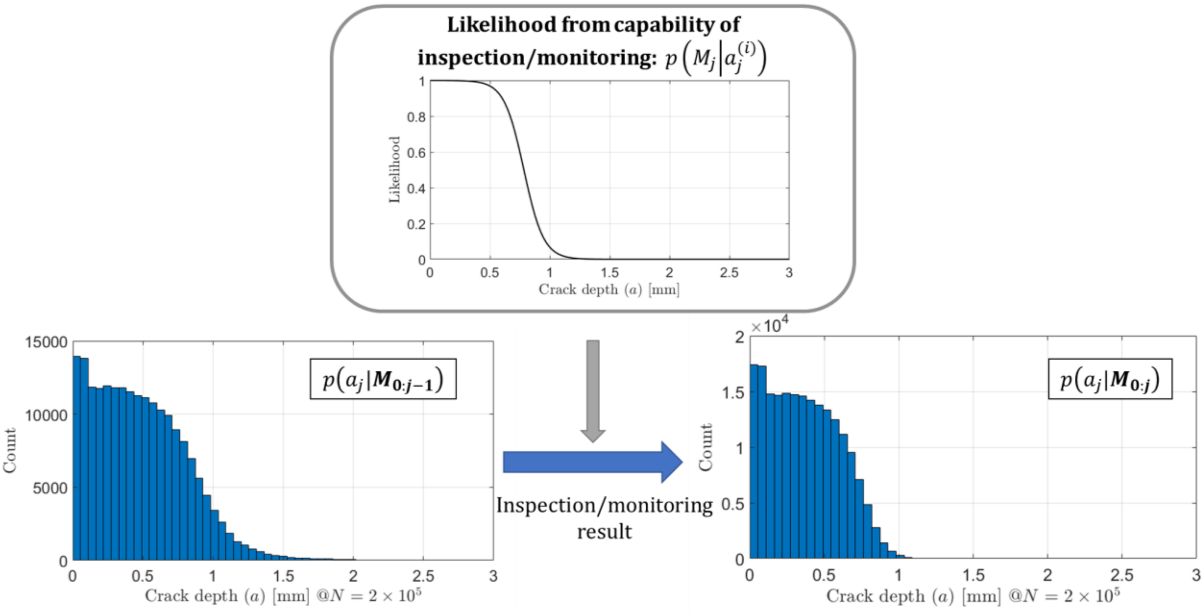

Figure 5.10 Illustration of the process of updating the histogram of postulate defect sizes with the most recent inspection/monitoring result.

Step 4: Resampling (optional) and updating

Typically when performing particle filtering, resampling is performed using the evaluated posterior distribution, $p(a_j|\boldsymbol{M}_{0:j})$; methods to conduct resampling can be found in [152]. This process is to avoid sample degeneracy where more and more samples have a weight of zero, resulting in fewer useful samples. However, it is known that standard methods of resampling would reduce the variance in samples as explained in [153]; the effect is known as sample impoverishment. This is particularly undesired for this specific application since the extreme cases are of great importance when evaluating the FFS of components. With reduced variance in samples, postulated defects of significant sizes are likely to be removed, resulting in a non-conservative estimate in FFS.

Therefore, resampling is not done in this study; an appropriate number of samples is used to ensure that there are sufficiently many non-zero weight samples throughout the evaluation process to provide accurate results. An alternative is to use more advanced resampling techniques such as deterministic resampling which are designed to minimise the effect of sample impoverishment [154].

Finally, the weighted (or resampled) samples from $p(a_j|\boldsymbol{M}_{0:j})$ are then used in the next iteration of the process when a new data point from inspection or monitoring is obtained (i.e. $j = j + 1$).

Overall, the process of recursively updating the defect size distribution using a particle filtering approach is summarised in Figure 5.11. The resulting $p\left(a_j|\boldsymbol{M}_{0:j}\right)$ will be used to evaluate the confidence in FFS of the component as described in the following section.

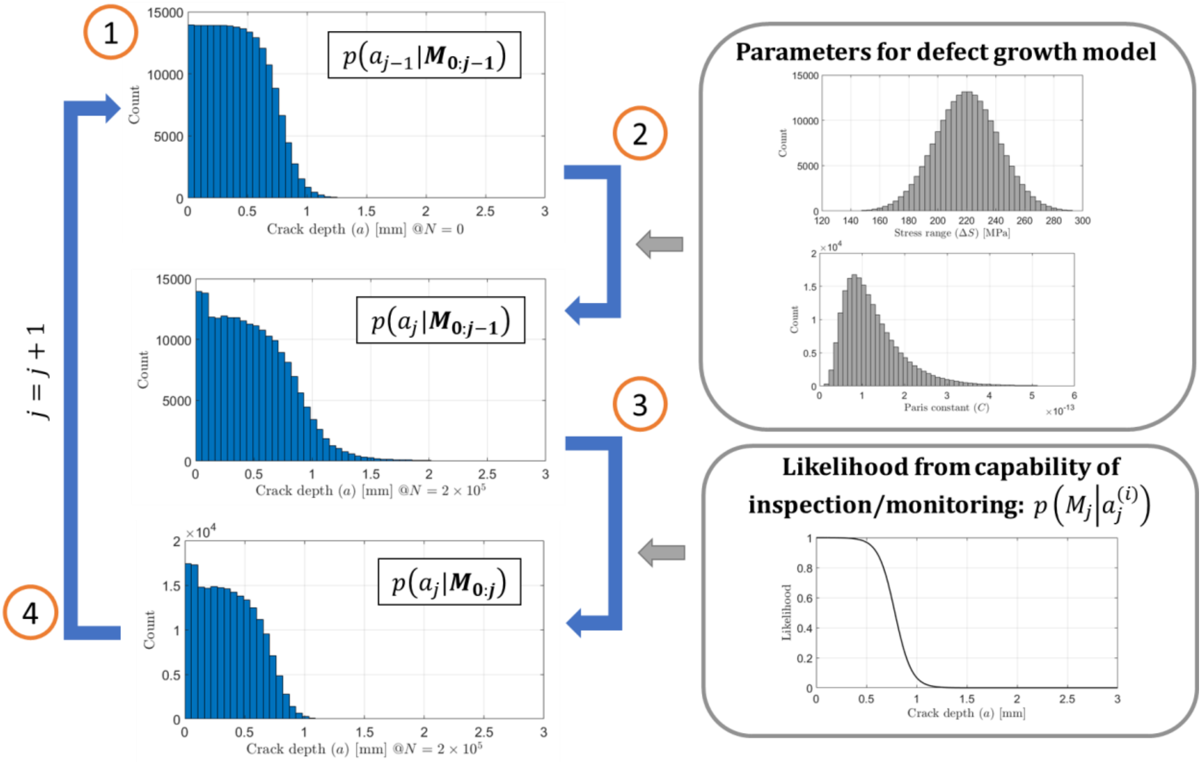

Figure 5.11 Illustration of the particle filtering approach to recursively update the defect size distribution given inspection or monitoring results. Numbers in orange circles represent the corresponding steps. Larger figures can be found in Figure 5.9 and Figure 5.10.

5.3.2 Updating the confidence in fitness-for-service

With the updated defect size distribution, a distribution of the number of loading cycles before the defined failure criterion (i.e. a through-wall crack in the example problem) is reached, denoted as N_f, can be evaluated. This in turn can be used to produce a plot of FFS_C as a function of loading cycles. The process is summarised in Figure 5.12. Samples of postulated defect sizes from the updated distribution and probabilistic defect growth parameters are drawn from their respective distributions, and N_f for each sample is evaluated. Subsequently, the probability density function of N_f can be produced as shown in the top right of Figure 5.12. This in turn can be used to evaluate the confidence in not failing (i.e. FFS_C) as a function of loading cycles, evaluated as one minus the cumulative distribution function of N_f; this is shown as the solid blue line in the top right of Figure 5.12. Note that the evaluation of N_f shown here is truncated at 2.5×10^6 cycles. The results at higher number of cycles are not relevant as the required FFS_{target} is typically a very large value, thus only the lower tail of the distribution of N_f is of interest.

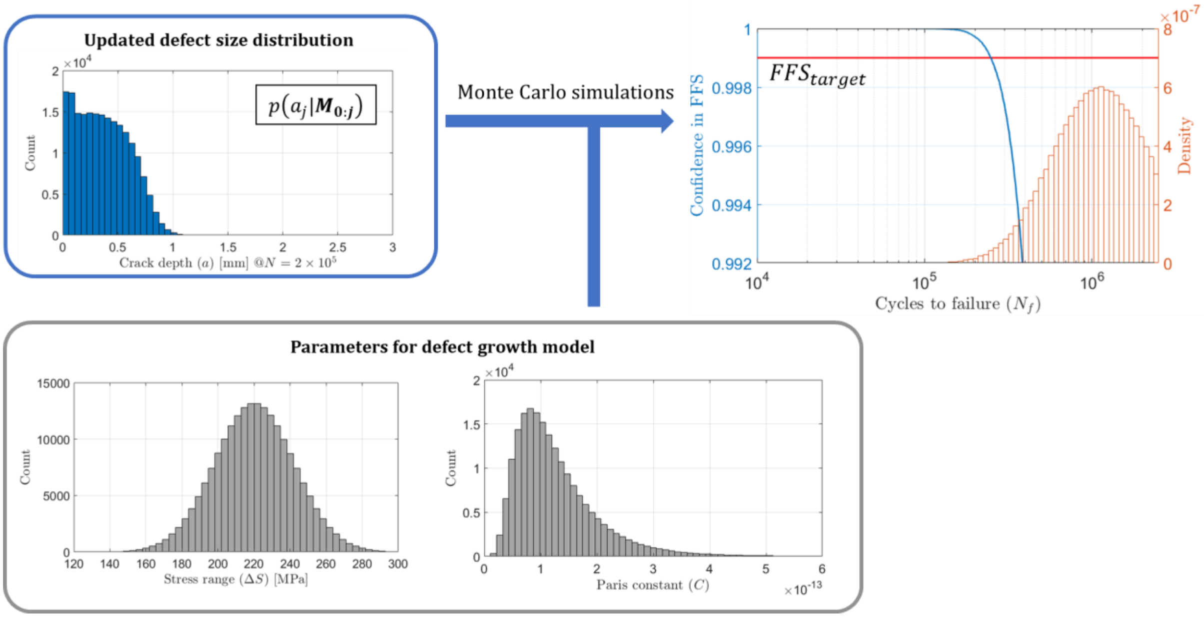

Figure 5.12 Illustration demonstrated the process of obtaining a prediction in when FFS_{target} is reached.

5.4 Results for the example problem

The previous sections detailed the process of updating the distribution of possible defect sizes and evaluating the FFS of the component. Using the process detailed, simulations can be conducted to illustrate how the confidence in FFS evolves over time when managed by inspection only or a combination of inspection and monitoring. To recall, the failure criterion of the pipe is defined as having a through-wall crack at the weld of the pipe while in operation. The limiting FFS is set at 99.9%. It is assumed that there is an opportunity to inspect at regular intervals every 10^5 cycles. Evaluation on the required number of inspections required is conducted for the first 2×10^6 loading cycles. The case where all inspections and data from PIMS return a negative result is considered, which is reasonably likely to occur since the median loading cycles to failure of the component evaluated using the initial postulated defect size distribution in Section 5.3.1 is estimated to be 2.2×10^6 cycles. The aim is to minimise the required number of inspections. Two management schemes are considered: first is when only periodic inspections are used; second is when a combination of inspections and monitoring is used.

5.4.1 Life-cycle management with inspections only

We begin by looking at the scenario where only in-service inspections are used to manage the welded pipe. The plot of confidence in FFS, FFS_C, against the number of loading cycles, N, is shown in Figure 5.13; this is equivalent to the schematic illustration shown earlier in Figure 5.7. It can be seen that for the first 6×10^5 cycles, an inspection is required every 2×10^5 cycles as indicated by the dashed blue lines. However, with successive negative inspection results the possibility that significant defects that would have grown to a detectable size are filtered out. Equally, the probability that there are only small defects below the crack growth threshold (see Section 5.2.1) increases. Thus, an inspection is only required every 3×10^5 cycles after the third in-service inspection and every 4×10^5 cycles after the fifth in-service inspection. Overall, in this specific scenario, a total of six in-service inspections is required for the managed component to safely operate for 2×10^6 cycles assuming all inspections return a negative result.

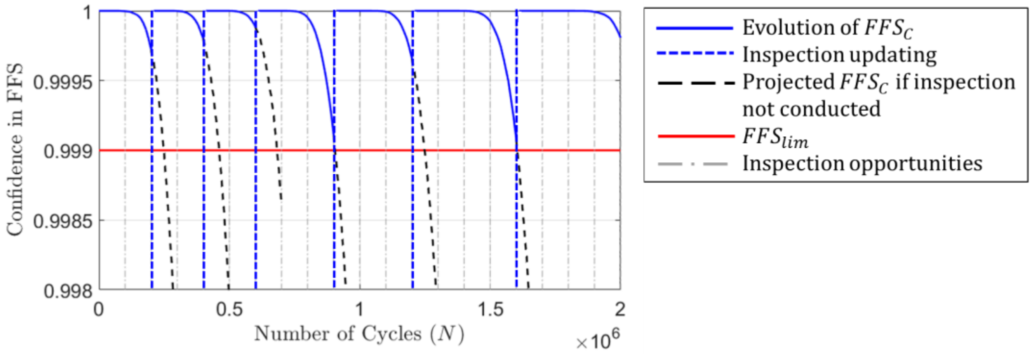

Figure 5.13 Evolution of confidence in FFS (FFS_C) throughout the life cycle of the managed component using only periodic inspections. A total of six in-service inspections are required for the component to last 2×10^6 cycles.

Another way of representing the results is to plot the projected remaining cycles until FFS_{lim} is reached as a function of number of cycles experienced by the component as shown in Figure 5.14. The dotted red line represents the interval between inspection opportunities. When the projected remaining cycles to FFS_{lim} falls below this line, the component would need to be inspected at the next available opportunity. Similar observations can be made with this figure as with Figure 5.13. This plot will become more informative when comparing to the results with the case where monitoring is incorporated.

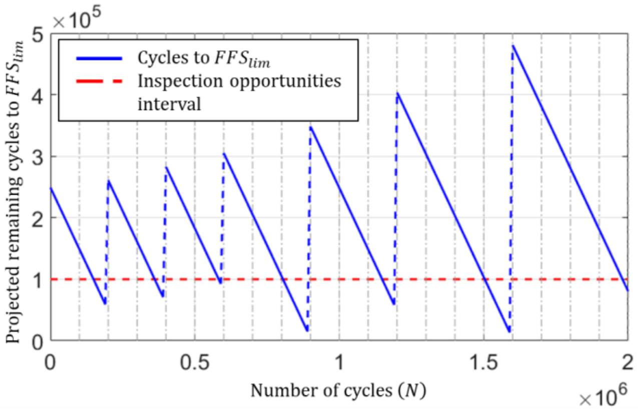

Figure 5.14 Plot of remaining number of cycles until FFS_{lim} is reached against number of cycles experienced by the component with inspections only.

5.4.2 Life-cycle management with inspections and monitoring

We now proceed to consider the scenario where a PIMS is installed on the welded pipe. It is assumed that monitoring data is collected every 10^4 cycles, which translates to 10 measurements between each inspection opportunity. The frequency of measurement chosen here is arbitrary and more frequent measurements can be made as long as the measurements does not become serially correlated as discussed earlier in Section 3.4.2.

The plot of FFS_C against N for the case where a monitoring system is incorporated is shown in Figure 5.15. Given that the PIMS has a POD of unity for a defect of the critical size (i.e. $POD(a_{crit}) = 1$), confidence in FFS immediately after a negative result from the PIMS would always be unity. Therefore, since the reduction in confidence between the frequent measurements made by the PIMS is negligible, FFS_C effectively remains constant at unity throughout if all monitoring results are negative.

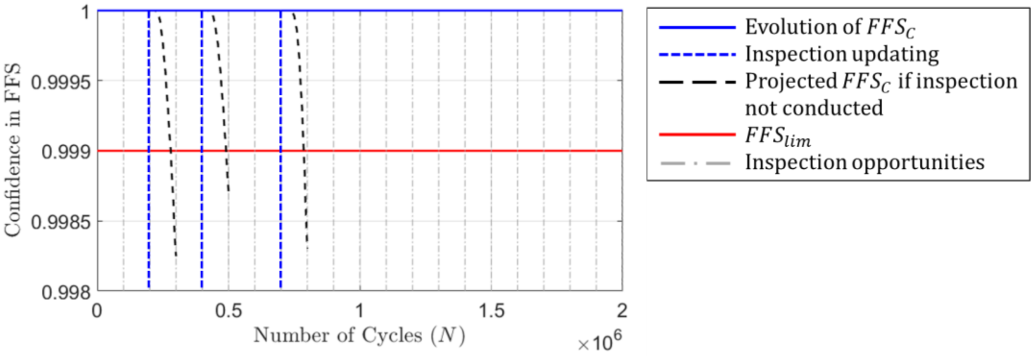

Figure 5.15 Evolution of confidence in FFS (FFS_C) throughout the life cycle of the managed component using inspections and monitoring. A total of three in-service inspections are required for the component to last 2×10^6 cycles.

However, it can be seen that the projected FFS_C until the next inspection opportunity may still fall below FFS_{lim}; this occurs after 2, 4, and 7×10^5 cycles in this specific scenario as indicated by the dash blue lines in Figure 5.15. To illustrate, the moment where $N = 2 \times 10^5$ cycles is used as an example. Using the process discussed in Section 5.3.2, the current postulated defect size distribution can be projected up to the next available inspection opportunity (i.e. at $N = 3 \times 10^5$ cycles). Subsequently, the confidence in not having a defect greater than a_{crit} (i.e. FFS_C) as a function of number of cycles from $N = 2 \times 10^5$ to 3×10^5 cycles can be evaluated; this is plotted as the dash black line in Figure 5.15. The results show that FFS_C will fall below the target confidence of $FFS_{lim} = 99.9\%$ before $N = 3 \times 10^5$ cycles. Hence, an inspection is required to ensure that FFS_C will stay above FFS_{lim} during operation.

This is also illustrated using the plot of the projected remaining cycles until FFS_{lim} against the number of cycles experienced by the component as shown in Figure 5.16. Comparing this to the same plot for inspection only in Figure 5.14, the most evident difference with the use of PIMS is that FFS_C and subsequently the projected remaining cycles to FFS_{lim} may be updated with each successive result from the monitoring system. This is evident from the gradual curvatures of the plot in Figure 5.16 as opposed to the straight lines as shown in Figure 5.14 with inspections only.

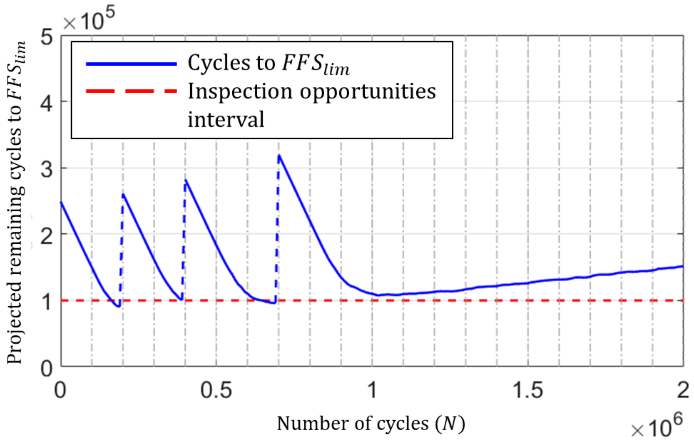

Figure 5.16 Plot of remaining number of cycles until FFS_{lim} is reached against number of cycles experienced by the component when monitoring is incorporated.

It can be seen from the results that the value of having a monitoring system installed is relatively limited during the early stages of component life. Recall that the detection capability of the monitoring system is inferior compared to the inspection technique (POD = 90% at a = 3.5 mm and 0.95 mm respectively). As a result, there is insufficient information to completely eliminate the possibility of significant defects being present and to keep the FFS above the desired level. This means that an inspection is required after 2, 4, and 7×10^5 loading cycles, which is nearly identical to the case where only inspection is used.

As more measurements with negative results are obtained, there is greater confidence in the FFS of the component, and thus an inspection is no longer required from 7×10^5 cycles onwards. It is observed that the projected remaining cycles to FFS_{lim} gradual increases with the number of loading cycles. While this may be non-intuitive, this is a result of the increase in probability of there being only small defects that will not propagate or propagate very slowly as evaluated from the defect growth model. This gradual increase in confidence is also present, though not as pronounced, in the case where only inspections are conducted; the gradual increase in inspection intervals is the result of the same effect. This effect is also observed in the example analysis of existing standards for probabilistic inspection planning (i.e. DNV-GL-C210 [14]) where a simple Bayesian updating is used.

Overall, the results show that three instead of six inspections are required in this specific scenario. If PIMS of better detection capabilities is used, it is possible that FFS_C will never fall below FFS_{lim}, thus eliminating the need to inspect while maintaining confidence in the structural integrity of the monitored component. This demonstrates the potential of using PIMS to filter the extreme cases in order to maintain sufficient confidence in its FFS. In terms of managing the life cycle of engineering components, this can translate to fewer inspection required or possibly eliminating the need for inspections. This would therefore reduce the risk and cost of maintenance of the monitored component.

5.4.3 PIMS with insufficient coverage

As discussed in the previous chapter, the detection capability of PIMS is not only governed by its sensitivity to defects, but also its spatial coverage. The POD curve of the monitoring system used in this study only considers the effect of random signal noise. Earlier discussion in Section 5.2.2.3 considered how the 95% confidence POD curve may be used to add conservatism to account for the influence of spatial coverage on the detection capability of PIMS. For PIMS that have insufficient coverage, using a 95% confidence POD curve can significantly reduce its assured detection capability as demonstrated in the previous chapter.

To demonstrate the limited capabilities of a monitoring system with insufficient coverage, a simulated POD curve is produced and used to repeat the study in order to mimic the effect of using a monitoring system with insufficient coverage. The simulated POD curve is shown in Figure 5.17. The POD curve is modified from that of the guided wave sensor used in the study. The POD curve is offset by 1 mm in terms detection capabilities as a function of defect depth and scaled by a factor of 0.9 in POD, indicating that 10% of defects would not be detected, regardless of size, due to insufficient area coverage. The values chosen here are arbitrary; a study on spatial coverage as discussed in the previous chapter would be required to fully capture the effect of insufficient coverage in practical applications.

Figure 5.18 and Figure 5.19 show the plots of FFS_C against N and plot of projected remaining cycles until FFS_{lim} against N when using the simulated POD curve to mimic insufficient coverage. Looking at the results, it can be seen that although the monitoring system is capable of filtering the extreme cases to some degree, its filtering effect is insufficient to achieve a reduction in the number of inspections required. This highlights the importance of evaluating the capabilities of PIMS from a life-cycle management point of view to quantify the value of using PIMS for each specific scenario.

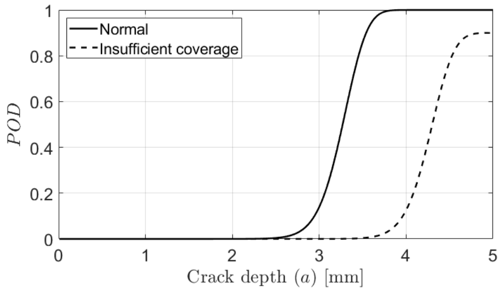

Figure 5.17 POD curve of the PIMS used in the example problem (solid black line), and a simulated PIMS with insufficient coverage (dotted black line).

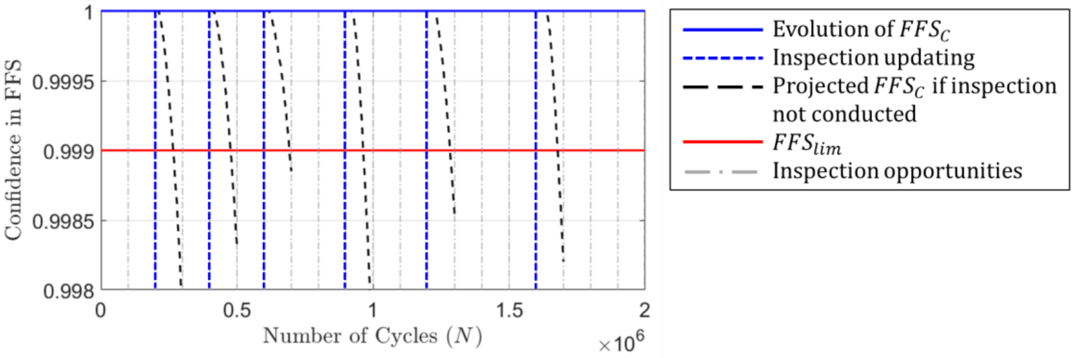

Figure 5.18 Evolution of confidence in FFS (FFS_C) throughout the life cycle of the managed component using inspection and monitoring with insufficient coverage. A total of six in-service inspections are required for the component to last 2×10^6 cycles; this is the same as using inspection only.

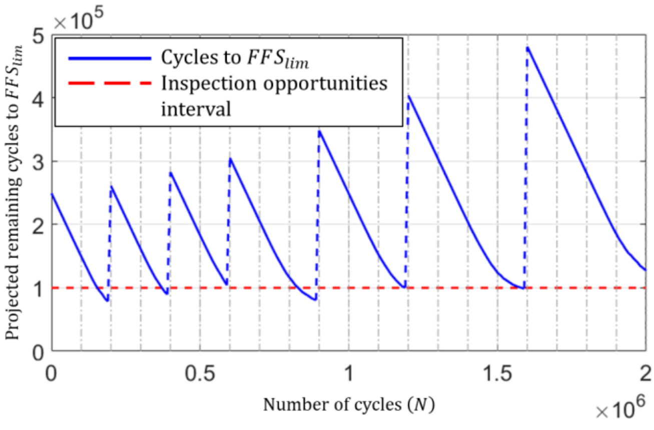

Figure 5.19 Plot of remaining number of cycles until FFS_{lim} is reached against number of cycles experienced by the component when monitoring with insufficient coverage is incorporated.

5.5 Discussion of results

The use of PIMS is only valuable when it translates into quantifiable benefits in managing the life cycle of engineering components and structures. The framework proposed in this chapter uses particle filtering methods to integrate the uncertainty quantified detection capabilities of PIMS and probabilistic defect growth models for fitness-for-service analysis. With successive negative results from the monitoring system, the less probable defect growth paths are filtered based on the results, thus recursively updating our confidence in the FFS of the monitored component.

The proposed approach simply treats the output of PIMS as binary detection/no detection results as similarly done in [133], [155], rather than converting the actual signal output into defect sizes as done in most studies using particle filtering for SHM applications [146], [147], [156]. The key advantages of doing so is that the analysis does not need to be conducted in real-time while the component is in operation; the confidence in FFS of the monitored component is known as long as the monitoring system returns a negative result. This is especially useful when a large number of components is being monitored at the same time. This also means that the potential benefits of PIMS can be easily quantified prior to deployment by assuming a presumed sequence of measurement results (i.e. all negative results for the first 2×10^6 cycles in this study). This will be useful when determining the optimal life-cycle management strategy for specific scenarios.

Using the successive negative results from PIMS to filter the possibility of substantial damage can be a very effective way of maintaining confidence in the FFS of engineering components. The FFS of an engineering component is typically governed by the extreme cases. As a result, even though the monitoring system used in this study is inferior compared to the inspection technique, the ability to constantly eliminate these extreme cases assures that failure of the component is not imminent. This in turn provides confidence in its FFS while reducing the need for in-service inspections.

Managing the life cycle of an engineering component with PIMS is conceptually different compared to the conventional approach where only in-service inspections are used. With the conventional inspection-based approach, the presence of defects that are much smaller than the critical defect size would need to be eliminated to ensure no defects would evolve to the critical size in between the inspections. Therefore, improvement in the detection capabilities of inspection techniques will need to be complemented with the advancement in predicting the growth of smaller defects in order there to benefit in terms of managing the life-cycle management of components. As discussed earlier in Section 2.1.2.5, this is challenging for fatigue damage due to its dependence on microstructure. This would inevitably result in substantial uncertainty in defect growth, consequently hindering the value of an improved inspection system from a life-cycle management perspective. In comparison, this complexity in modelling the growth of small defects can potentially be avoided with the use of PIMS. Given the ability for PIMS to make frequent measurements, only the growth of more substantial damage is of interest when evaluating the FFS of the monitored component.

The proposed approach can also be used to demonstrate how measurements from PIMS may justify for life extension of a monitored component. A sequence of negative detection results can provide confidence that no substantial damage has incurred during its operation. Provided that the component is continuously monitored, there may be sufficient confidence that the component would not fail imminently and thus the component is safe for continued operation.

Nevertheless, the effectiveness of using PIMS is greatly dependent on many parameters for each specific application, some of which include the detection capabilities of the monitoring system, operating conditions, the failure criterion, and the number of opportunities to inspect. For instance, PIMS may not be as effective for cases where the maximum tolerated defect size is small since this would demand a monitoring system that has both great sensitivity and spatial coverage. Under such considerations, the use of PIMS may not be a viable solution from both a technical and economical point of view.

It is believed that further additions can be made to develop the proposed framework. Firstly, the implementation of cost analysis as done in [133], [157] would be of great value to justify the business case for implementing PIMS to manage the life cycle of engineering components. Also, rather than using a single, potentially conservative POD curve for the analysis, a Monte Carlo approach to sample POD curves for a more accurate evaluation of FFS can be done as mentioned earlier in Section 5.2.2.3. This would however require significantly more computational power and thus tools to allow for efficient running of simulations would have to be developed and implemented.

5.6 Conclusions

A framework that integrates uncertainty quantified PIMS data into evaluating the fitness-for-service of engineering components is proposed. Using particle filtering methods, frequent measurements from PIMS may be used to recursively update the distribution of possible defect sizes in the component, consequently updating our confidence in its FFS. The framework can be used to quantify the benefits of using PIMS from the perspective of managing the life cycle of engineering components.

An illustrative example of managing the life cycle of a welded pipe undergoing three-point fatigue bending is used to demonstrate the value of the proposed framework. The pipe was managed by either periodic inspections only or a combination of inspection and monitoring. Results of the study show that the ability of PIMS to filter cases of substantial damage is an effective way of maintaining confidence in FFS of engineering components. This translates to fewer in-service inspections required that maybe costly and hazardous to conduct.

The effectiveness of using PIMS is dependent on multiple factors such as the sensitivity and spatial coverage of the monitoring system, operating conditions and the failure criterion. It is proposed that the framework can be used for a quantitative comparison between the use of in-service inspections and PIMS in specific engineering applications, as well as a comparison between PIMS of different configurations. This framework will therefore be a useful tool for promoting the adoption of PIMS for damage detection in suitable engineering applications.

6 Remnant life predictions using rate measurements from permanently installed monitoring systems

6.1 Introduction

The previous three chapters focused on the use of PIMS to detect the presence of a defect. Once a defect is found, measurements taken from PIMS can also be used to characterise and track the growth of a detected defect and to perform remnant life predictions as the component nears final failure. Most research focuses on using PIMS as an extension to the conventional inspection approach of using empirical crack growth laws as discussed in Section 2.1.2 to perform remnant life predictions. The use of PIMS makes it possible to measure in-situ operating conditions [158] and perform crack detection and sizing in real-time [159] to produce frequently updated estimates of remnant life.

Despite the interest in using PIMS to predict the remnant life predictions of engineering components, little research has been conducted to utilise the continuity of data that monitoring can provide. One of the main benefits of using PIMS is that measurements may be taken much more frequently than periodic inspections. This is illustrated in Figure 6.1, which plots the measured crack length of a fatigue experiment against the number of loading cycles. The red crosses are analogous to data obtained via regular in-service inspections, while the blue dots represent data that can be obtained with monitoring. Frequent data collection enables the possibility of obtaining rate of change estimates and identification of trends in the data. It is proposed that rate of change information obtained from PIMS may be exploited for improved fatigue remnant life predictions.

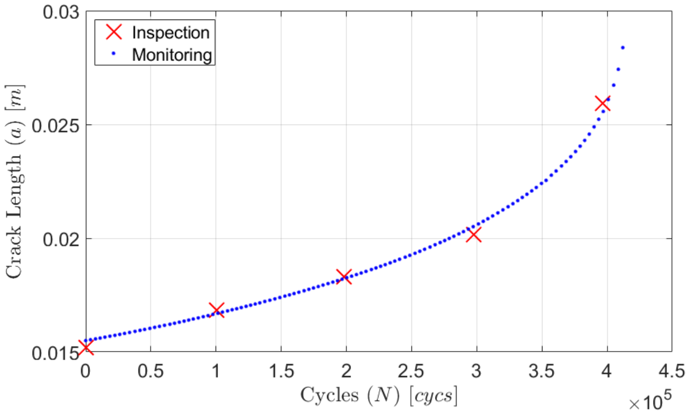

Figure 6.1 Plot of crack length against number of loading cycles for the fatigue experiment. The red crosses are analogous to data obtained via regular in-service inspections, while the blue dots represent what a PIMS can obtain.

Fatigue damage is an example of a positive feedback mechanism [19]; an increase in damage leads to an increase in the rate of damage accumulation. This positive feedback behaviour leads to a characteristic form of the temporal evolution of damage accumulation as seen in Figure 6.1. This characteristic form of damage accumulation was first noted by Voight [160], who subsequently developed the Failure Forecast Method (FFM), which utilises this characteristic form to perform remnant life predictions. The FFM has been adopted to evaluate various forms of failure, including volcanic eruptions [161], power-law creep damage [94], and fatigue damage [19]. Compared to conventional damage assessment methods, the FFM does not rely on assumptions of material properties, geometry, or operating conditions, but rather the observed response of the component. This reduces the number of sources of uncertainty and potentially provides more confident remnant life predictions.

This chapter aims to perform a statistical analysis to evaluate the efficacy of using the FFM to perform fatigue remnant life predictions, and also to further develop its use for more complex loading conditions. The performance of the FFM, which relies on near-continuous monitoring data will be compared to the conventional inspection-based approach where crack length measurements are interpreted in isolation. The findings presented in this chapter are also published in [149].

This chapter begins by detailing the methodology of the conventional inspection approach and the monitoring approach using the FFM in Section 6.2 and 6.3 respectively. The two approaches are then used to analyse an example fatigue experiment in Section 6.4, where the accuracy and confidence in the predictions made by the two methods are then compared and discussed. Section 6.5 proposes, validates and discusses strategies to use the rate-based monitoring approach for non-constant amplitude loading. Finally, conclusions are presented in Section 6.6.

6.2 Inspection approach to remnant life predictions

6.2.1 Review of methodology

Using the conventional inspection approach, when defects are found with NDE inspections and sufficient information on the operating conditions, material properties and geometry of the component is available, empirical crack growth laws can be used to perform fatigue life predictions. There are many empirical crack growth laws available, again the commonly adopted Paris' law will be used here as defined in the previous chapter in Eq. 5.1. By numerically integrating Paris' law, the predicted remnant life, N_f, would be the number of loading cycles until a critical defect size, a_{crit}, is reached.

As with many other modes of material failure, fatigue damage accumulation is by nature probabilistic, hence probabilistic methodologies are needed to quantify uncertainties and determine the level of conservatism required [162], [163]. As discussed in the previous chapter, a regularly inspected component is deemed safe for continued operation if there is sufficient confidence that any detected defect will not propagate and reach the critical defect size. A reconstructed schematic of how inspections update our estimates of probability of failure from DNVGL-RP-C210 is shown in Figure 6.2 [14]. If the probability of failure exceeds a critical value prior to the next scheduled inspection, there is no longer sufficient confidence in the integrity of the component, and actions will need to be taken to repair or replace the component. The critical probability of failure of the component is specific to each engineering application, mainly dictated by the risks and consequences involved should a failure occur. Therefore, confidence in life predictions is crucial to minimise conservatism and hence make it possible to safely operate the component closer to its actual failure time.

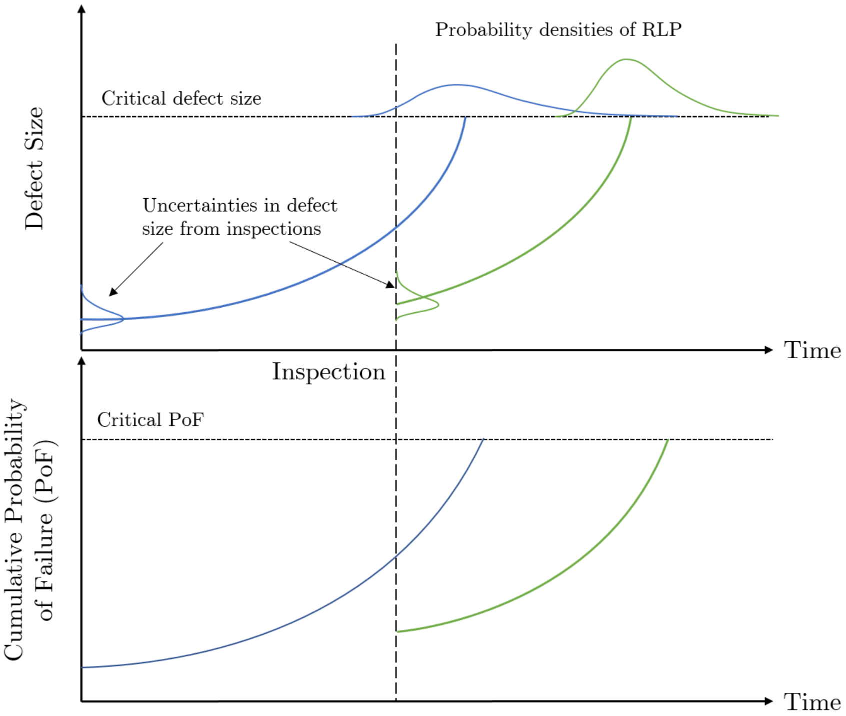

Figure 6.2 Schematic reconstructed from the DNVGL Recommended Practice C210 showing how the probability of failure updates with an inspection [14].

To demonstrate the inspection approach to performing fatigue life predictions, and to later compare with the proposed rate-based monitoring approach, a statistical analysis on a set of fatigue experimental data was conducted to establish the confidence of fatigue life predictions. The experiment uses a standard 316 stainless steel compact tension specimen; the geometry and loading parameters are given in Figure 6.3 and Table 6.1. The crack is electrical discharge machined (EDM) and fatigue precracked. This is to minimise the effect of the crack growth mechanism being different during initial cycles of fatigue where the fatigue crack initiates from the EDM "crack". The crack propagation is monitored using a potential drop measurement system, but only one data point every 10^5 cycles are used to imitate the infrequent data available from inspections.

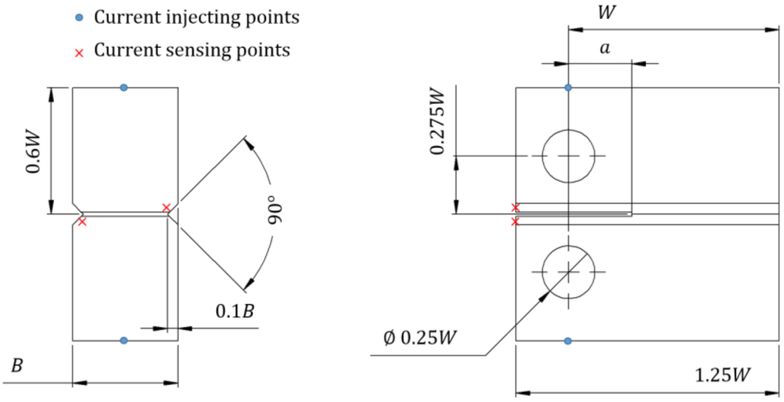

Figure 6.3 Geometry of the specimen used in the experiment

Table 6.1 Geometry and loading parameters of the specimen in accordance to ASTM 647-15e1 [91] shown in Figure 6.3.

Parameter	Value
W (mm)	50
B (mm)	25
a (mm)	15.5
Maximum load, P_{max} (kN)	11
Load ratio, R	0.1

To evaluate the confidence in the remnant life predictions, the uncertainties for all individual parameters will have to be quantified for the statistical analysis as detailed in Table 6.2. A discussion on quantifying these values is given below. It is fully recognised that the assumptions made on the statistical variation of the input parameters are hugely simplistic; the uncertainties of the parameters are assumed to be independent, and the effect of uncertainty in geometry is not considered. However, it is believed that these assumptions are sufficient to illustrate how uncertainties of each input parameter aggregate to result in the overall uncertainties in remnant life predictions. The assumptions made here are optimistic and greater uncertainties are to be expected in industrial applications. This method offers a framework that may be used for the analysis of more specific examples.

Table 6.2 Table showing the quantified uncertainties for each input parameter of the empirical crack growth law used in the statistical analysis.

Parameter	**Mean value**	**Standard error**
Measured crack length (a_0) [mm]	Updates with each inspection	1
Critical crack length (a_{crit}) [mm]	39.3	Not considered
Paris' constant ($\ln(C)$)	-25.5	0.264
Paris' exponent (m)	2.88	Not considered
Maximum load (P_{max}) [kN]	35	3.5
Load ratio (R)	0.1	Not considered
Geometry factor	Evaluated from standards	Not considered

Since crack growth in only one direction is considered in this analysis, the geometry of the defect can be characterised by a single crack length measurement, a_0. This measurement is updated every time an inspection is conducted. The error in defect size measured from NDE is assumed to be normally distributed with a standard deviation of 1 mm and no bias; this is approximated with the nominal capabilities of a state-of-the-art NDE system [164]. In practice, this would greatly depend on the NDE technique used as well as positioning and geometry of the defect. Other than the capabilities of the NDE technique, there are also other sources of uncertainties, such as the placement of measurement probes as well as calibration error [165]. Overall, the assumption made here are likely optimistic.

The critical crack length, a_{crit}, is often conservatively estimated from the plane strain fracture toughness of the component using linear elastic fracture mechanics. The uncertainty in this is not considered for the analysis as the final crack length has a relatively small effect on the final estimated failure cycle.

The Paris constant, C, and exponent, m, of a specific component are very rarely known with accuracy as they can vary even with the same material under nominally identical conditions as demonstrated by Virkler [137]. The constants are typically fitted retrospectively to fatigue test data to capture the stochastic nature and material variability, and hence exact values are unavailable when making life predictions. Standardised values and standard deviations of the Paris' constants from the British Standards 7910 [16] as shown in Table 2 are therefore used to simulate how analyses are typically done in industrial applications.

Finally, the operating conditions of the specimen include loading cycles experienced, temperature of the environment and the effect of aggressive environments, all of which could have an effect on the crack growth characteristics. Only the nominal stress range, $\Delta\sigma$, is considered in this analysis. The error in loading is assumed to be normally distributed with a standard error of 3.5 kN (10% of the maximum load) and no bias. The error in load ratio, R, is not considered. Again, an optimistic assumption is made here as the uncertainty in loading is highly dependent on the application and whether design load or loading data based on structural health monitoring is used.

6.2.2 Statistical analysis on remnant life predictions

Incorporating all these uncertainties, a 10^4 trial Monte Carlo simulation was performed to evaluate the probability density function (PDF) of the remnant life of the component described earlier. All the input parameters are sampled randomly from their statistical distributions defined in Table 6.2 and kept constant for each trial, and the predicted N_f is evaluated using the Paris' crack growth law as defined in Eq. 5.1. A log-normal distribution was then fitted to the simulation results to obtain statistical properties of the prediction [137].

The PDF of the predicted N_f prior to the experiment ($N = 0$, where N is the number of loading cycles the component has experienced) is plotted in Figure 6.4. The point at which failure occurred during the experiment is shown with a dotted black line, which is at

$N_f = 4.24 \times 10^5$. From the results of the analysis the confidence in the predicting remnant life can be quantified. The 3σ lower and upper confidence bounds at the beginning of the experiment were 2.1×10^5 and 2.26×10^6 respectively, showing that the confidence in the predicted N_f is rather low, with a confidence interval that spans over an order of magnitude. As previously discussed, it is necessary to adopt the lower bound estimate as the final prediction to ensure safe operation; large uncertainty therefore requires extreme conservatism.

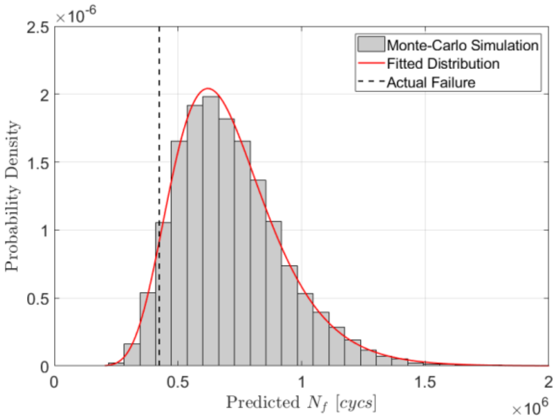

Figure 6.4 Results of the Monte Carlo simulation used to obtain the probability density function of the failure cycle at $N = 0$. The solid line shows the fitted log-normal distribution, and the dash line indicates the actual failure time of the experiment, $N_f = 4.24 \times 10^5$.

6.2.3 Inspection updating

With each inspection where a new crack length is obtained, the estimates of the variables $\Delta\sigma$ and C can also be updated using Bayesian updating. As also described earlier in Eq. 5.2, Bayes' theorem states that,

$$P(A|B) \propto P(A) \times P(B|A) \qquad \text{Eq. 6.1}$$

where $P(A)$ is the prior distribution, $P(B|A)$ is the likelihood, and $P(A|B)$ is the posterior distribution. In the context of this analysis, A is our estimate of the variables $\Delta\sigma$ and C, and B is the event of an inspection result. The likelihood function is obtained numerically by considering the probability of the resulting measurement given each combination of $\Delta\sigma$ and C. Together with the prior knowledge on the distribution of the variables as detailed in Table 2, an updated estimate of the distribution of the variables can be obtained using Bayes' theorem. This process is done recursively with each inspection as the posterior distribution from the inspection becomes the prior distribution during the analysis of the next inspection.

The probability of failure after each new inspection is shown in Figure 6.5, assuming that an inspection was performed every 10^5 cycles. As seen from the results in this particular case, the inspection-based approach is initially overestimating N_f, gradually converging to the actual N_f with each inspection being closer to failure. Further discussion is given in Section 6.4, where the inspection approach is compared with the monitoring approach.

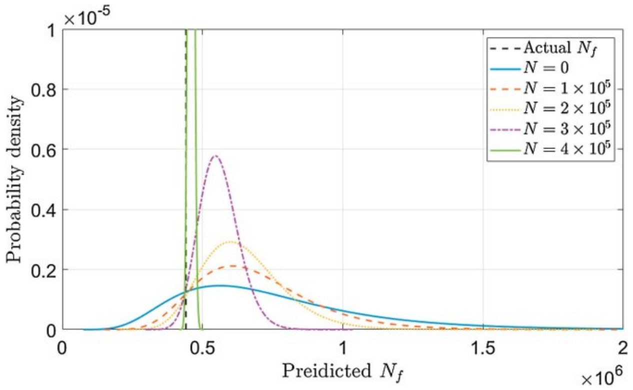

Figure 6.5 Fitted log-normal distribution of the predicted failure cycle at every inspection made at intervals of 10^5 cycles.

6.3 Monitoring approach to remnant life predictions

An alternative way of performing remnant life predictions is the rate-based monitoring approach. Instead of conducting periodic in-service inspections, a PIMS can be installed to monitor the rate at which the damage accumulates. Remnant life predictions can then be performed in real-time while the component is in operation using the Failure Forecast Method (FFM).

6.3.1 Review of methodology

Voight observed that the empirical relationship shown in Eq. 6.2 can be used to describe a wide range of rate-dependent mechanisms of material failure [166], which are also known as positive feedback mechanisms [19].

$$\left(\frac{d\Omega}{dt}\right)^{-\alpha}\left(\frac{d^2\Omega}{dt^2}\right) - A = 0 \qquad \text{Eq. 6.2}$$

$\Omega =$ an observable metric of damage
A and $\alpha =$ material constants

Voight proceeds to state that the equation can be integrated for $\alpha > 1$ to give,

$$\left(\frac{d\Omega}{dt}\right)^{1-\alpha} = A(\alpha - 1)(t_f - t) + \left(\left.\frac{d\Omega}{dt}\right|_f\right)^{1-\alpha} \qquad \text{Eq. 6.3}$$

Where t_f is the failure time and $\left.\frac{d\Omega}{dt}\right|_f$ is the rate of damage accumulation at failure.

The rate of damage accumulation at failure is often orders of magnitude greater than accumulation rates early on in fatigue life. It is therefore reasonable to assume that the rate of damage accumulation at failure to be infinite. Hence, by rearranging Eq. 6.3, life estimates of a damage mechanism conforming to this empirical relationship can be made,

$$t_f = t + \frac{1}{A(\alpha - 1)}\left(\frac{d\Omega}{dt}\right)^{\alpha-1} \tag{Eq. 6.4}$$

It has been shown that the Paris' crack growth law conforms to this empirical relationship. Corcoran [19] demonstrated that in order for a positive feedback mechanism to adhere to Voight's empirical relationship, it must satisfy the following,

$$\frac{df(\Omega)}{d\Omega} = Af(\Omega)^{\alpha-1} \tag{Eq. 6.5}$$

Corcoran proceeds to provide several generic forms of damage mechanism that would satisfy Eq. 6.5, one of this being,

$$\frac{d\Omega}{dt} = k\Omega^n \tag{Eq. 6.6}$$

This closely resembles that of the Paris' crack growth law, with time replaced by number of loading cycles, N, and Ω being a quantity that resembles crack length. Furthermore, it is empirically observed that $\alpha \approx 2$ for many cases, including fatigue crack growth. A more detailed derivation and discussion on the appropriateness of Voight and the assumption of $\alpha \approx 2$ can be found in [19].

Hence, for fatigue crack growth, Eq. 6.4 may be rewritten as,

$$\left(\frac{d\Omega}{dN}\right)^{-1} = A\left(N_f - N\right) \tag{Eq. 6.7}$$

so,

$$N_f = N + \frac{1}{A}\left(\frac{d\Omega}{dN}\right)^{-1} \tag{Eq. 6.8}$$

where Ω now becomes a generic sensor output of a monitoring system that changes with crack growth. This highlights one of the benefits of the FFM, which is the flexibility that is afforded to the monitoring technique. As the absolute crack length is not interpreted directly, but rather the relative change in rate, generic sensor outputs which are symptomatic of damage may be used as a proxy. In the examples used in this paper, resistance measurements from a potential drop technique are used as a metric of crack growth. A more comprehensive discussion on the requirements of the measurement and monitoring system can be found in [19].

Using Eq. 6.7, the failure cycle, N_f, can be estimated by performing a regression analysis on the inverse damage accumulation rate, $\left(\frac{d\Omega}{dN}\right)^{-1}$, against the number of loading cycles, then extrapolating the regression fit and finding the x-axis intercept where crack growth rate is infinite as schematically demonstrated in Figure 6. By assuming α = 2 such that the regression becomes linear, the prediction made would be the negative ratio between the intercept and slope of the regression fit. This method of performing remnant life predictions is known as the Failure Forecast Method (FFM).

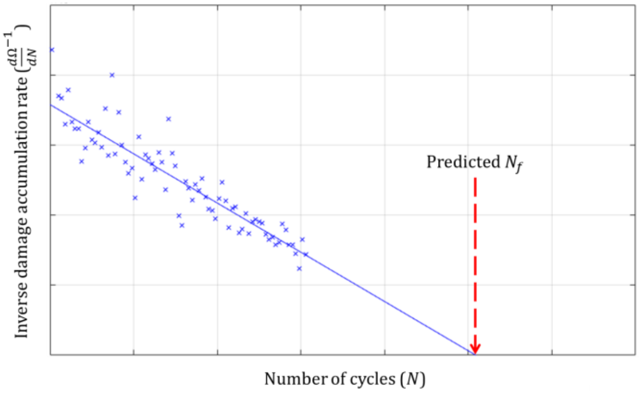

Figure 6.6 Schematic illustration of the inverse damage accumulation rate $\left(\frac{d\Omega}{dN}\right)^{-1}$ against number of cycles for a set of fatigue testing data to demonstrate the use of the FFM for remnant life predictions.

To demonstrate the use of the FFM for remnant life predictions, the experimental results were analysed using the method, simulating a monitoring system being installed on a defective component while it continues operation. The rate of change in signal, in this case the resistance measurement, R, from the potential drop measurement system, is calculated to perform the FFM analysis without converting to crack length measurements as with typical analysis of potential drop measurement results. This is obtained from the slope of the linear regression fit performed on every 5 resistance measurements. The number of data points chosen are based on the precision of the measurement data; less precise data would require more points to obtain accurate rate measurements at the expense of fewer rate data points and vice versa.

With this, the inverse of the rate of change in resistance, $\left(\frac{dR}{dN}\right)^{-1}$, can be obtained, and a linear regression analysis of the data is performed to evaluate the predicted N_f. Figure 6.7 plots the results in intervals of 10^5 cycles. The dashed black line indicates the actual failure cycle. In this analysis, a maximum of the most recent 100 $\frac{dR}{dN}$ data points were used as indicated on the plot by the two solid red lines; this chosen number of points is a balance between having sufficient data points to minimise uncertainty in the regression analysis, while limiting the effect of historical data where the damage growth mechanism may be different.

These predictions can be made in real time as the component is fatigued, and the resulting predicted N_f against number of fatigue cycles is plotted in Figure 6.8. Again, the dotted black line is where actual failure occurred.

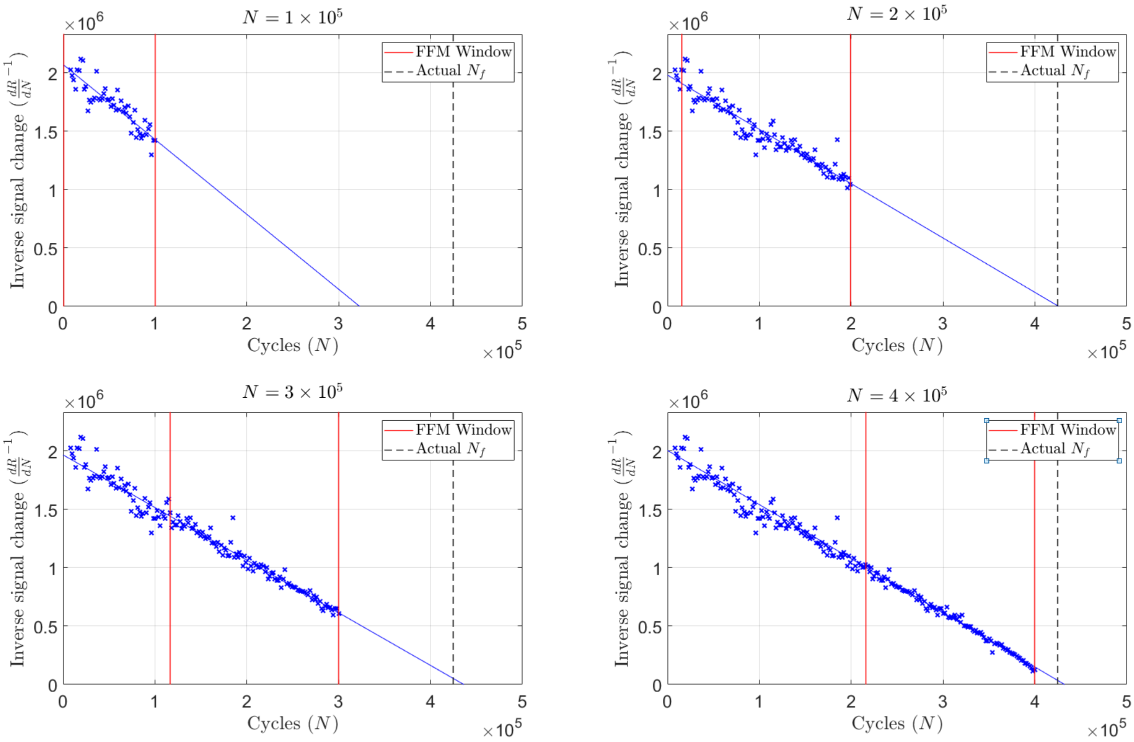

Figure 6.7 Remnant life predictions made using the FFM at intervals of 10^5 cycles. The vertical solid lines indicate the window of $\frac{dR}{dN}$ data used for the FFM, and the dash line indicates the actual failure cycle.

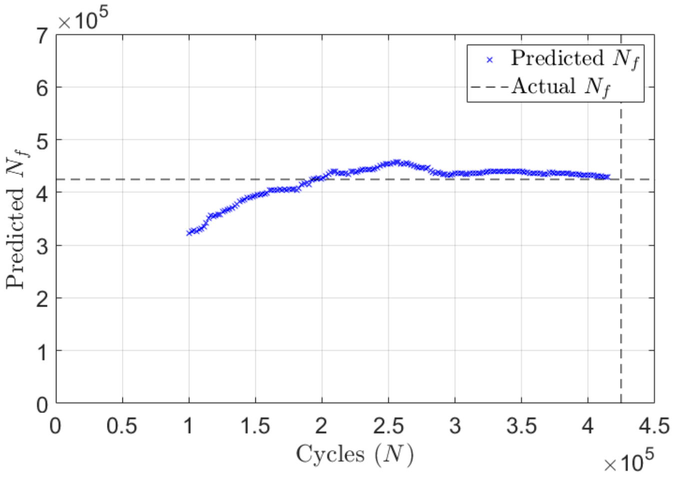

Figure 6.8 Plot of predicted N_f against number of loading cycles for the fatigue experiment. Dash lines indicate the actual failure cycle.

Utilising PIMS that take frequent measurements and hence provide continuous rate estimates, the predicted N_f can be continuously updated as more damage accumulation rate data is obtained in-service to provide real-time life predictions. The major advantage of using the FFM for life predictions is that minimal knowledge on the operating conditions is required. As opposed to predictions made with inspection results, parameters including loading conditions, material properties, geometry of the component and actual crack length measurements are not required. Assuming that all operating conditions remain constant, the only input required for the FFM is any input signal that can be used to measure the rate of damage accumulation.

6.3.2 Statistical analysis of remnant life predictions

As opposed to the inspection approach where empirical crack growth laws are used, the FFM simply uses the extrapolated point of infinite damage accumulation rate as the predicted failure time. Therefore, the only source of uncertainty for the FFM would be uncertainties in the damage accumulation rate measurements, which in turn results in uncertainties in the regression fit and the extrapolated x-axis intercept.

The distribution of the predicted failure cycle, $p(\widehat{N}_f)$ can be analytically evaluated as demonstrated by Todd et al. [167]. The analytical solution is,

$$p(\widehat{N}_f) = \frac{\sqrt{1-\rho^2}\sigma_0\sigma_1 e^{\frac{\mu_1^2\sigma_0^2+2\rho\mu_0\mu_1\sigma_0\sigma_1-\mu_0^2\sigma_1^2}{2\sigma_0^2\sigma_1^2(1-\rho^2)}}}{\pi\left(\sigma_0^2+2\rho\sigma_0\sigma_1\widehat{N}_f+\sigma_1^2\widehat{N}_f^2\right)}$$
$$+\frac{e^{\frac{\left(\mu_0+\mu_1\widehat{N}_f\right)^2}{2\left(\sigma_0^2+2\rho\sigma_0\sigma_1\widehat{N}_f+\sigma_1^2\widehat{N}_f^2\right)}}\operatorname{erf}\left[\frac{\mu_0\sigma_1\left(\rho\sigma_0+\sigma_1\widehat{N}_f\right)-\mu_1\sigma_0\left(\sigma_0+\rho\sigma_1\widehat{N}_f\right)}{\sqrt{2-2\rho^2}\sigma_0\sigma_1\sqrt{\sigma_0^2+2\rho\sigma_0\sigma_1\widehat{N}_f+\sigma_1^2\widehat{N}_f^2}}\right]\left[\mu_0\sigma_1\left(\rho\sigma_0+\sigma_1\widehat{N}_f\right)-\mu_1\sigma_0\left(\sigma_0+\rho\sigma_1\widehat{N}_f\right)\right]}{\sqrt{2\pi}\left(\sigma_0^2+2\rho\sigma_0\sigma_1\widehat{N}_f+\sigma_1^2\widehat{N}_f^2\right)^{\frac{3}{2}}} \qquad \text{Eq. 6.9}$$

$\operatorname{erf}(*)$ = the error function
$\widehat{N}_f$ = variable for the predicted failure cycle
μ_j = mean estimate of the intercept and slope, denoted with subscript 0 and 1 respectively
σ_j = estimated standard deviation of the intercept and slope
ρ = correlation coefficient of the intercept and slope of the linear regression

The PDF can be obtained in real time to estimate the confidence in the predictions made using the FFM and updated when new data points are obtained while the component is in operation. The results were verified with a Monte Carlo simulation using synthetic data with random measurement uncertainties characterised by the actual data set from the experiment. The results at $N = 2 \times 10^5$ for both the analytical and 10^4 trial Monte Carlo simulation is shown in Figure 6.9.

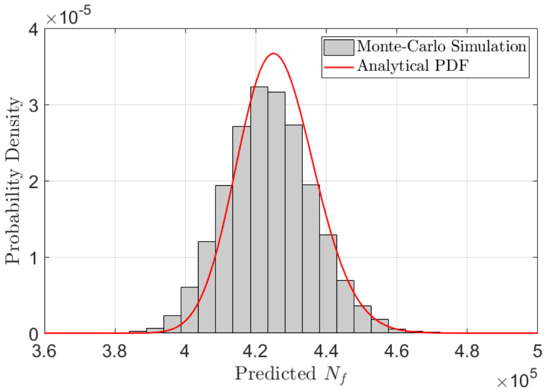

Figure 6.9 Plot of the PDF of the predicted failure cycle at $N = 2 \times 10^5$ using the FFM. The histogram represents the results of the Monte Carlo simulation, the line graph represents the analytical solution.

6.4 Comparison of the two approaches to remnant life predictions

6.4.1 Statistical comparison between inspection and monitoring

Using the above methods, a comparison between the inspection and monitoring approach to fatigue life predictions can be made. Figure 6.10 plots the median life predictions of the inspection and monitoring results. This shows that the predictions made using the monitoring approach converges much more quickly to the actual failure cycle. From $N = 2 \times 10^5$ onwards, approximately half the life of the component, all predictions made using the monitoring approach were within 10% the actual failure cycle. Conversely with the inspection approach, there is no way of adapting or correcting for the actual operation conditions. Therefore, the predictions made converge slowly to the actual failure time as the end of life of the component approaches.

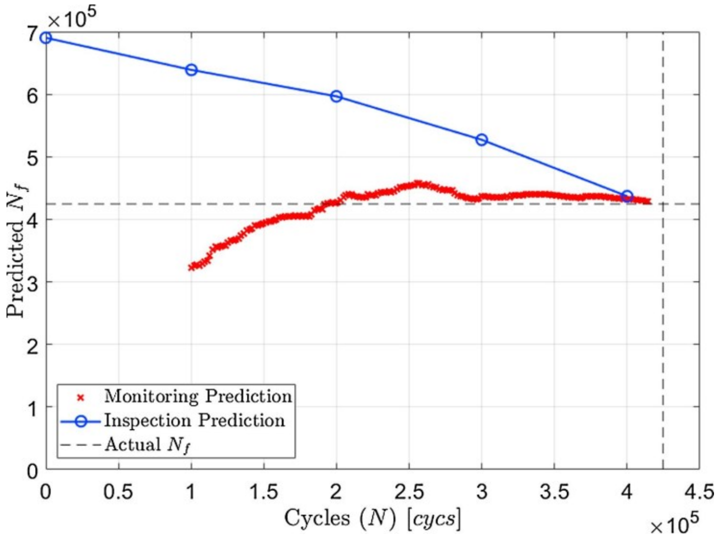

Figure 6.10 Plot of the median life predictions against number of loading cycles using the inspection and monitoring approach.

Not only are the predictions more accurate with the monitoring approach, the confidence in the predictions made is significantly greater as shown in Figure 6.11. Consider the predictions made with both methods at $N = 2 \times 10^5$. Assuming that the target level of confidence in the integrity of the component is 99.7% (3σ), the conservative remnant life prediction made using the inspection and monitoring approach would be $N = 2.8 \times 10^5$ and $N = 3.5 \times 10^5$ respectively. At this point, the estimated remnant useful life of the component would be 0.8×10^5 cycles should the inspection-based approach be used, while with the use of the monitoring-based approach, the component would have an estimated remnant useful life of 1.5×10^5 cycles. Given that an inspection is only performed every 10^5 cycles, the component would fail to meet the required threshold of confidence in integrity before the next inspection. In comparison, due to significantly greater confidence, the conservative predictions made with the monitoring approach are much closer to the actual failure cycle.

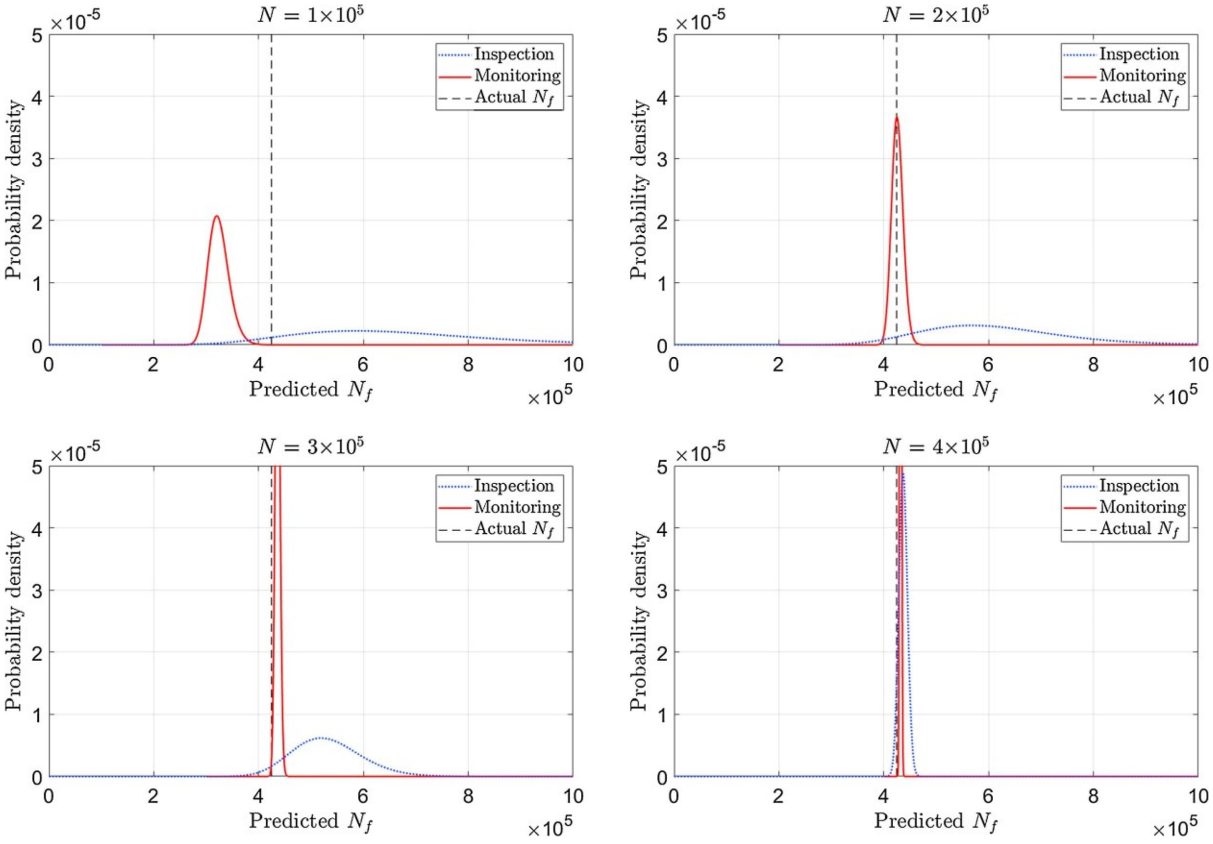

Figure 6.11 Plots of the PDFs of the predicted failure cycle at intervals of 10^5 cycles. The dotted graph represents the results from the inspection approach, the solid graph represents the results of the monitoring approach, the dash line indicates when the component actually failed.

While the choices of target confidence and inspection interval here are arbitrary, the study demonstrates how estimations with greater confidence via the monitoring approach make it possible to safely operate the component closer to its actual failure time. These predictions, including the confidence bounds, can be made in real-time while the component is in operation. Thus, the use of monitoring can provide improved awareness of the damage state of the component without the need of inspections, potentially reducing the duration or even the frequency of costly planned outages.

6.4.2 Validity of using the FFM for fatigue life predictions

Despite the life predictions made using the FFM having lower uncertainty, systematic errors resulting in bias in the predictions are also apparent at various stages of the experiment. From Figure 6.10 and Figure 6.11, it is evident that the remnant life is initially underestimated (even falling outside the confidence bounds initially), followed by a near-constant overestimation for the remaining life. These discrepancies are due to a known epistemic error in the method as the fatigue damage passes through different phases of crack growth. Figure 6.12(a) shows a typical schematic plot of crack growth rate against stress intensity factor, which is a function of stress, crack length and geometry of a fatigued component. Figure 6.12(b) schematically shows how the subsequent plot of inverse crack growth rate against number of cycles would appear. This non-linear relationship between the inverse crack growth rate and number of cycles is the major cause of the systematic error in the predictions made by the FFM. The systematic error in this experiment is however not very significant as the specimen of this test spends most of its fatigue life within the Stage II crack growth regime. However, in practice, the validity of the FFM would have to be considered based on the expected portion of fatigue life of the monitored component that will be spent within the Stage II crack growth regime.

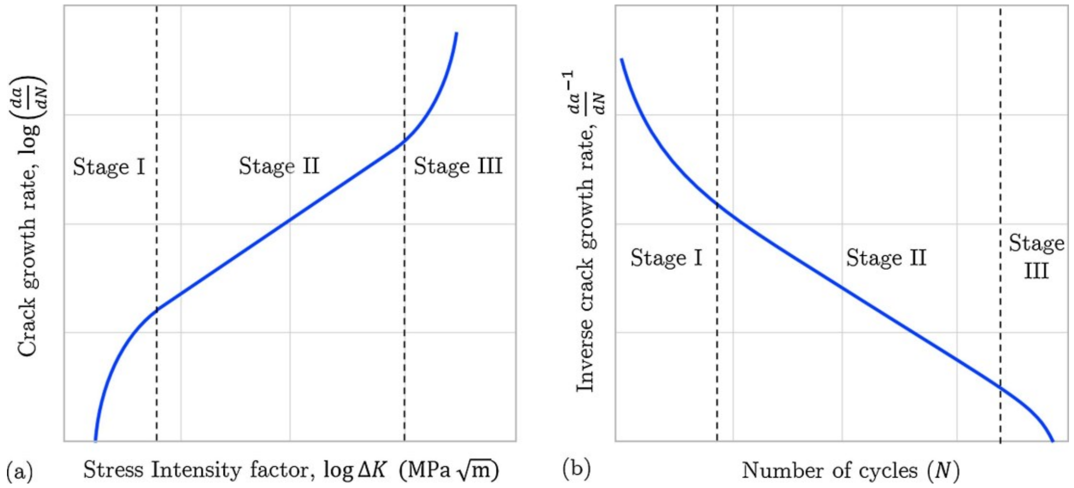

Figure 6.12 (a) Illustration of a typical plot of crack growth rate against stress intensity factor, which is a function of stress, crack length and geometry of a fatigued component; (b) resulting plot of inverse crack growth rate against number of cycles.

The crack growth mechanism is different during initial cycles of fatigue, since the radius of a fatigue crack tip is orders of magnitude smaller than the "crack" that was electrical discharge machined (EDM). Therefore, a fatigue crack would have to "initiate" from the EDM crack. This would have crack growth characteristics that in some ways resemble the Stage I crack growth region; remnant life is thus underestimated as the slope of the regression fit of inverse crack growth rate against number of cycles is greater in Stage I than in Stage II crack growth.

The subsequent overestimation of remnant life can also be explained similarly. During the terminal stages (Stage III) of crack growth, the crack growth rate accelerates and deviates from the linear relationship between crack growth rate and stress intensity factor. This is also reflected in the plot of inverse crack growth rate against number of cycles as demonstrated in Figure 6.13, resulting in the component failing earlier than predicted by the FFM. A linear fit is plotted to better illustrate the acceleration in crack growth, which can be seen at around $N = 4 \times 10^5$. However, since this terminal stage of fatigue crack growth is only a very small portion of the overall life of the component, the resulting overestimation is minimal.

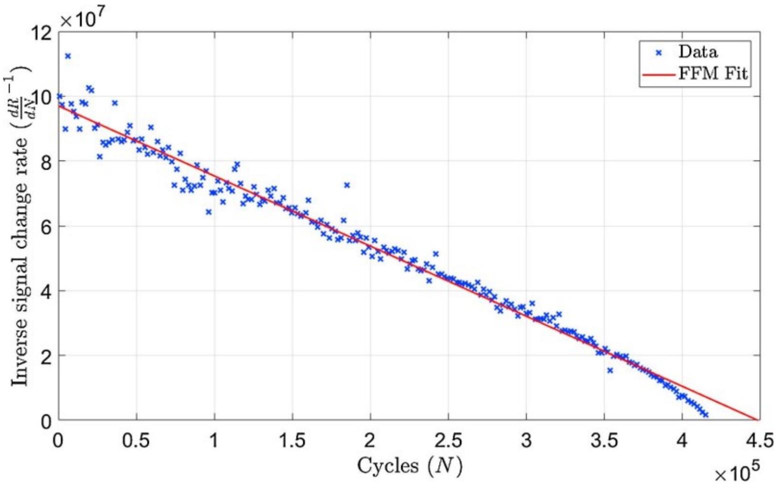

Figure 6.13 Plot of inverse signal change rate against number of cycles from the fatigue experiment, highlighting how the change in crack growth rate deviates from the linear relation at terminal stages of fatigue crack growth.

It is therefore clear that for the FFM to provide accurate fatigue life predictions, the remnant fatigue life of the component must be dominated by a single damage accumulation mechanism. In the case of this experiment, a majority of the fatigue life of the component is spent at Stage II, Paris law crack growth. Thus, the predictions made in this region were accurate with relatively small systematic error. Such an error also exists with the inspection approach, but since there are such great uncertainties in the predictions, its effect becomes negligible. More advanced empirical crack growth laws such as the Forman equation [168] or the NASGRO equation [38] can be used to better model the crack growth behaviour across multiple stages of fatigue crack growth. However, more input parameters, each with an associated uncertainty, is required for these crack growth laws, resulting in significant uncertainties in the prediction despite the crack growth model being more accurate.

6.4.3 Failure criterion of the FFM

As shown earlier in Eq. 6.7 and Eq. 6.8, it was assumed that the damage accumulation rate at failure is infinite, hence the x-axis intercept of the plot of inverse growth rate against number of cycles is the estimated point of failure. This proves to be a valid assumption as shown in Figure 6.13 where the last data point is very close to the x-axis. The validity of this assumption is determined by the requirement that the period of monitoring would need to cover a significant fraction of the crack propagation life of the component such that the range of crack growth rates measured is sufficiently large.

In industrial engineering applications, there are numerous cases where the failure criterion is instead determined by the ability of the component to withstand a critical load as discussed in Section 2.1.2.4. In these cases, failure under nominal loading conditions is no longer the failure criterion for the fitness of service of the component, as assumed with the FFM.

One potential way to accommodate this while using the FFM to perform life predictions is to introduce a finite critical crack growth rate failure criterion. With knowledge of the material properties of the component under its operating conditions as well as the correlation between stress intensity and crack growth rate, a maximum allowable crack growth rate using empirical crack growth laws can be obtained, as schematically demonstrated in Figure 6.14. The failure is then estimated to occur at the point where the linear regression of the FFM crosses a specific value of inverse crack growth rate instead of the x-axis intercept. However, this process requires more information on the materials properties and operating conditions, as well as a calibrated conversion between signal change and crack growth rate. This means that the advantage of using the FFM is significantly reduced as more information and thus uncertainties are introduced.

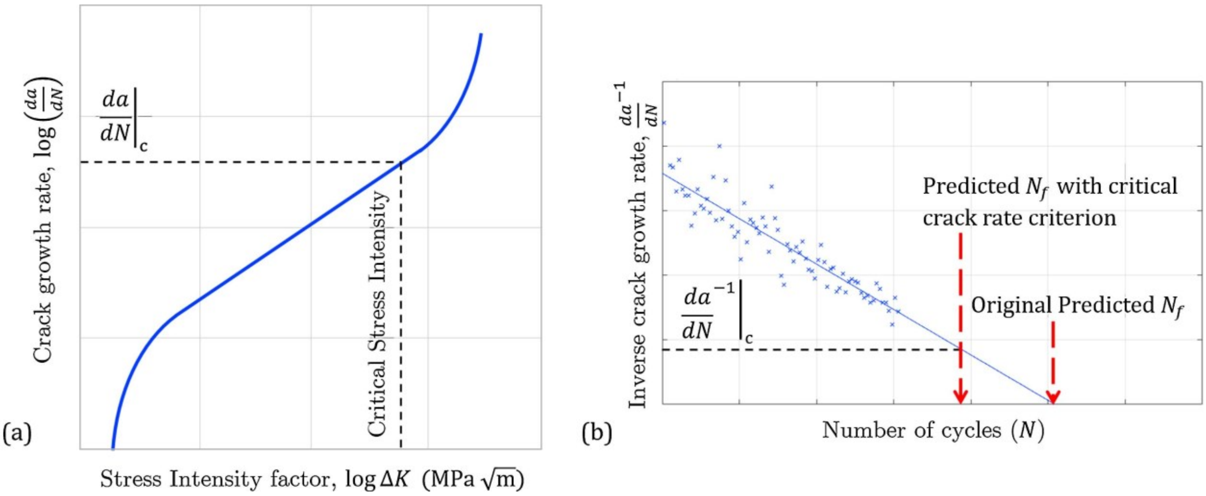

Figure 6.14 Schematic demonstration of how a finite critical crack growth rate can be introduced in the FFM. (a) illustration of how a critical crack growth rate can be defined from the plot of crack growth rate against stress intensity factor; (b) graph demonstrating how this can be implemented while using the FFM.

6.5 FFM for non-constant amplitude loading

Real-life engineering components are often subjected to varying loading conditions that cannot be simplified to a constant amplitude fatigue problem. It is therefore important to understand the capabilities of the FFM for fatigue damage monitoring under non-constant amplitude loading. Three cases of loading are considered and evaluated via experiments in this section: a step change in loading condition, single overloads, and variable amplitude loading.

6.5.1 Step change in loading condition

The first case of non-constant amplitude loading considered is a step change in loading conditions. This might occur, for example, when a defect is found in a power station component, where it is common to derate the unit to reduce the stresses and so extend the component life. A method of compensating for a change in loading conditions while using the FFM is proposed.

Voight briefly outlined an expanded version of the integrated form of his equation to account for variable stresses at failure [166]. For α > 1,

$$\frac{d\Omega}{dt} = \left[A(\alpha-1)(t_f - t) + \left(\left.\frac{d\Omega}{dt}\right|_f \left(\frac{\sigma}{\sigma'}\right)^n\right)^{1-\alpha}\right]^{\frac{1}{1-\alpha}} \qquad \text{Eq. 6.10}$$

where σ' is some reference stress, σ is the estimated stress level at failure, which in the case of a step change in loading condition would be the new load, and n is an empirical constant.

It is proposed that the above equation can be expressed in a more useful form by introducing the variables,

$$t_{eq} = t \times \left(\frac{\sigma}{\sigma'}\right)^{n(\alpha-1)}, \qquad t_{eq,f} = t_f \times \left(\frac{\sigma}{\sigma'}\right)^{n(\alpha-1)}, \qquad \text{Eq. 6.11}$$

Substituting Eq. 6.11 into Eq. 6.10, rearranging and assuming infinite growth rate at failure,

$$\frac{d\Omega}{dt_{eq}} = \left[A(\alpha-1)\left(t_{eq,f} - t_{eq}\right)\left(\frac{\sigma}{\sigma'}\right)^{n(\alpha-1)(\alpha-2)}\right]^{\frac{1}{1-\alpha}} \qquad \text{Eq. 6.12}$$

Putting this in the context of fatigue crack propagation,

$$\frac{d\mathrm{a}}{dN_{eq}} = \left[A(\alpha-1)\left(N_{eq,f} - N_{eq}\right)\left(\frac{\Delta\sigma}{\Delta\sigma'}\right)^{n(\alpha-1)(\alpha-2)}\right]^{\frac{1}{1-\alpha}} \qquad \text{Eq. 6.13}$$

where,

$$N_{eq} = N \times \left(\frac{\Delta\sigma}{\Delta\sigma'}\right)^{n(\alpha-1)}, \qquad N_{eq,f} = N_f \times \left(\frac{\Delta\sigma}{\Delta\sigma'}\right)^{n(\alpha-1)} \qquad \text{Eq. 6.14}$$

This definition of equivalent cycles is similar to Basquin law as mentioned in Section 2.1.2.1, which states that there is a power law relationship between the fatigue life of a component and the loading amplitude the component experiences. What is shown here is that a similar relation can be used in crack growth monitoring and FFM to compensate for the effect of change in loading. It is also observed that the empirical constant n should equate to the Paris' exponent m. Recall the Paris' law is expressed as,

$$\frac{da}{dN} = C(\Delta K)^m = C\left(Y(a)\Delta\sigma(\sqrt{a}\right)^m \qquad \text{Eq. 6.15}$$

It can be seen that the crack growth rate is proportional to the stress range raised to the power of m, hence it would be reasonable to assume that the two empirical constants are equal.

As mentioned earlier, it is reasonable to assume α = 2. Therefore, Eq. 6.13 simplifies to,

$$\frac{d\mathrm{a}}{dN_{eq}} = A\left(N_{eq,f} - N_{eq}\right) \qquad \text{Eq. 6.16}$$

This is identical to Eq. 6.7, that was used for the FFM analysis in previous sections, but with equivalent cycles replacing the actual cycles of loading. This shows that by introducing the definition of equivalent cycles N_{eq}, continuity of relation between the crack growth rate and number of cycles can be retained despite changes in loading amplitudes. Thus, the same method as discussed in Section 6.3 can be used to perform fatigue life predictions while considering the change in operating conditions, given that the relative change in loading, $\left(\frac{\Delta\sigma}{\Delta\sigma'}\right)$, and the Paris' exponent, m are both known.

To validate the equivalent cycles method for compensating step changes in loading conditions, a fatigue experiment using a CT specimen made of S275 steel with parameters shown in Table 6.3 was conducted while crack growth was monitored using the front-face compliance method using clip gauges. The experiment simulates the case where it is proposed that a defective engineering component is to be operated at derated conditions to limit the crack growth rate and it is necessary to predict the remnant life given the new loading. In this example, the maximum load is reduced by 20% while the load ratio remains constant. The experiment compares the accuracy and confidence in the predictions made in the following two cases. The first case is where no monitoring system was used, so an inspection to measure the crack length is conducted immediately prior to the derating to estimate the remnant life of the component. The second case is where a monitoring system was installed on the component long before the derating, hence the FFM with the equivalent cycles method can be used to estimate the remnant life of the component using data collected previously.

Table 6.3 Geometry and loading parameters of the specimen in accordance to ASTM 647-15e1 [91] shown earlier in Figure 6.3.

Parameter	Value
W [mm]	80
B [mm]	20
a [mm]	16
Maximum load, P_{max} [kN]	35 for the first 4×10^4 cycles, then 28 until failure
Load ratio, R	0.1

A plot of crack length against the number of cycles of the experiment is shown in Figure 6.15(a). The data points represented as crosses and circles are data collected before and after the change in loading respectively; the data collected prior to the change in loading is used for the FFM prediction. Figure 6.15(c) and (d) show the inverse crack growth rate against number of cycles and equivalent inverse crack growth rate against equivalent number of cycles respectively. The use of the equivalent cycles method in Figure 6.15 restores the continuity of the plot of inverse crack growth rate against cycles, allowing for the use of FFM for fatigue failure analysis where the loading is not at constant amplitude. The FFM regression fits shown on the graphs were obtained using data collected from the first 4×10^4 cycles before the reduction in loading. Note that inverse crack growth rate is used only because calibrated measurements of crack length were readily accessible with this monitoring system. Should a different monitoring system that satisfies the requirements detailed in [19] is used, conversion from signal change to growth rate is not necessary.

To quantify the accuracy and confidence in the use of the FFM for remnant life predictions with load changes using the equivalent cycles method, a statistical analysis similar to that discussed previously was performed. In addition to the uncertainties in damage growth rate measurement, the uncertainties in the loading conditions and Paris exponent now have to be considered. The relative change in loading is assumed to have a mean of 20% and a standard error of 2%. The uncertainty in the Paris exponent is not considered in BS7910. Therefore, in this analysis, the Paris exponent is assumed to have a mean of $m = 2.88$ and a coefficient of variation, $COV = 0.0582$. The mean value is from the BS7910, while the COV was obtained from the statistical analysis by Gobbato [140] of the Virkler fatigue test data [137]. For comparison, a statistical analysis was also performed for the periodic inspection case with the same uncertainties shown earlier in Table 6.2.

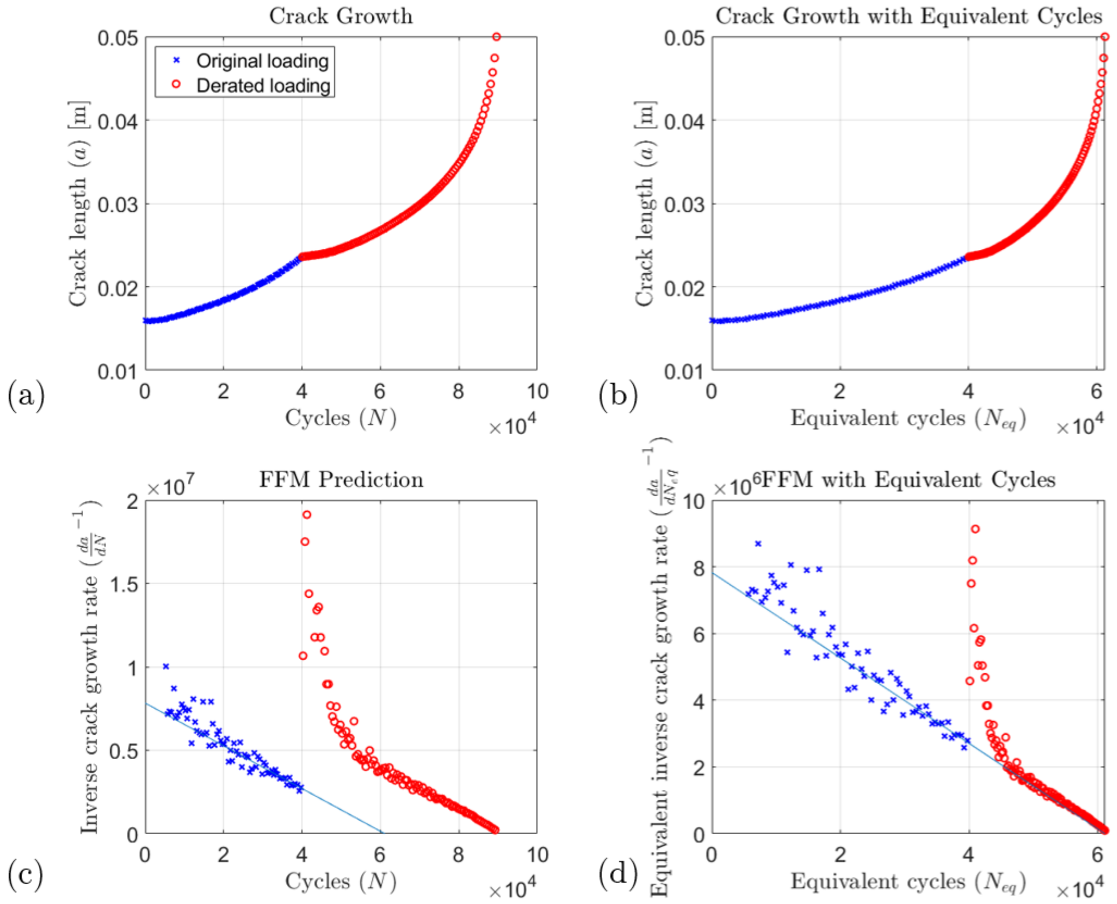

Figure 6.15 Plot of (a) crack length against number of cycles; (b) crack length against number of equivalent cycles; (c) inverse crack growth rate against number of cycles; (d) equivalent inverse crack growth rate against number of equivalent cycles for the fatigue experiment with a change in loading conditions. Crosses and circles represent data points prior to and after the change in loading conditions.

Figure 6.16 shows the results of the analysis. The dotted lines show the probability density functions of the remnant life estimation assuming the original loading conditions; of course these predictions underestimate the failure time as the true remnant life was extended by the derating. The corrected remnant life estimates based on the assumed change in load is shown in Figure 6.16 with solid lines. As with the constant load results of Figure 6.11, the uncertainty in the life prediction made with the FFM is lower than that from the inspection based approach. However, the improvement is not as large as the constant amplitude loading results. In order to account for the change in loading, the FFM now relies on the relative change in loading conditions and the Paris exponent, each with associated uncertainty, which translates to less confident predictions. Overall, it is demonstrated that by using this equivalent cycle method for FFM, more confident predictions in remnant life can be made prior to changes in operating conditions than conducting an inspection immediately before the change.

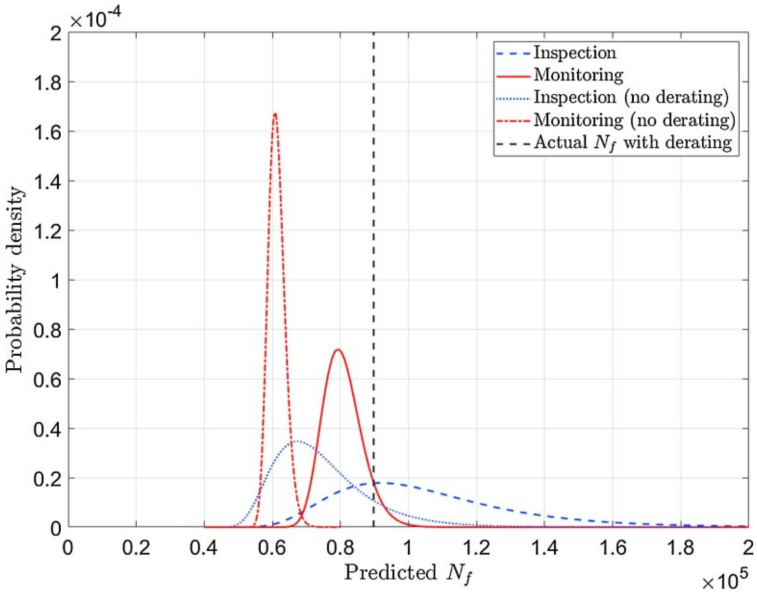

Figure 6.16 Plots of the fitted PDF for the predicted failure prior to the change in loading. Both the predictions made with and without considering the change in loading are plotted. The vertical dash line represents when the component actually failed.

It can be seen from Figure 6.16 that the FFM underestimates the remnant life after the change in loading. This underestimation is caused by crack growth retardation as a result of local plastic deformation at the crack tip, similar to the effect of an overload as discussed in Section 2.1.2.3. Figure 6.15(c) shows a sudden increase in inverse crack growth rate (i.e. decrease in crack growth rate) for an appreciable period after the load decreases. The initial cycles at high load create a comparatively larger plastic zone in front of the crack tip, which the initial cycles of the low load have to propagate through. This results in a decrease in crack growth rate and subsequently extends the life of the component beyond what would be predicted before derating, effectively shifting the actual failure time into the future, thus the discrepancy. For the inspection approach, empirical compensations have been developed to account for the effect [169], [170], but again more input parameters with uncertainties would have to be introduced, resulting in greater uncertainties in the predictions made.

The retardation following a derating illustrates that it is important to understand how the use of the FFM is affected by the effect of such loading interaction effects, namely crack growth behaviour that is dependent on load history. This is a key step to implementing fatigue monitoring in industrial applications where loading is often non-constant.

6.5.2 Isolated overloads

To illustrate and evaluate the effect of isolated overloads on predictions made using the FFM, an experiment identical to the one detailed in Section 6.2 is conducted, except that two single-cycle overloads with maximum loads 40% and 60% greater than a normal cycle were introduced during the tests at around $N = 2 \times 10^5$ and 3×10^5 respectively. Figure 6.17 plots (a) the crack length and (b) inverse signal change rate against number of cycles. Initial cycles after the overload are affected by the plastic zone generated by the overload, and then resumes as normal as the crack tip exits the overload plastic zone. As a result, an overload would effectively translate the plot of inverse signal change rate against number of cycles to the right. From Figure 6.17, it is evident that starting from approximately 5×10^4 cycles after an overload, the linear relation between inverse damage accumulation rate and number of cycles is restored and subsequent data can be used to perform life predictions using the standard FFM.

In industrial applications, this means that once the component has operated for a period of time after the overload, it is always possible to restart the FFM prediction with only the data collected afterwards. It is also believed to be possible to use the gradient of the initial FFM fitting as a prior estimation of the slope for the FFM fitting of the data collected after the overload. Moreover, monitoring data can clearly indicate when an overload has occurred, and so is beneficial in understanding the damage state of the component.

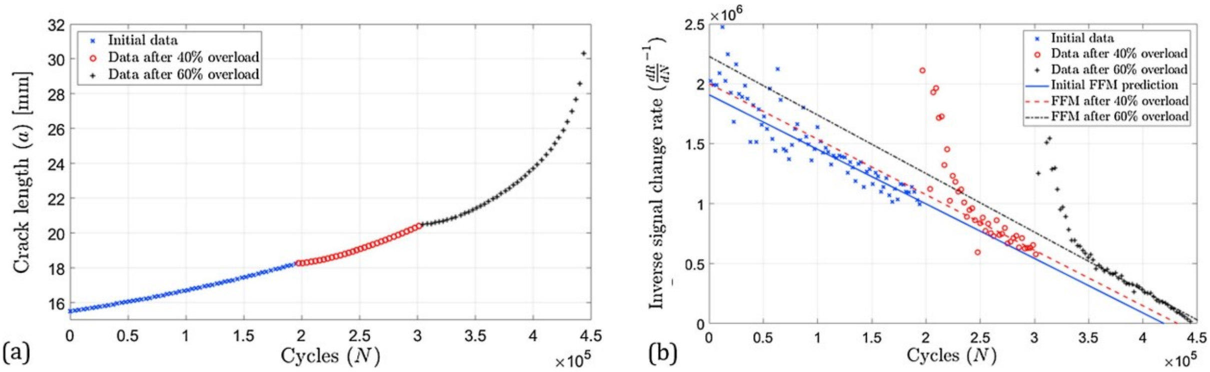

Figure 6.17 Plot of crack length (a) and inverse signal change rate (b) against number of cycles for the overload test.

6.5.3 Variable amplitude loading

Other than isolated overloads, there are also cases where overloads and underloads occur periodically during the life cycle of a component. These components may be subjected to variable amplitude loadings that can be described by a probability distribution [171]. The combination of high and low loads result in retardation and acceleration effects as the sequence of these loadings affect the state of the local stress-strain field ahead of the crack tip [172].

In order to investigate these effects, a fatigue experiment with variable amplitude loading was conducted. The specimen geometry was as described in Table 6.1, but with initial crack length of 25.5 mm. The component was loaded at a constant mean load of 4.125 kN and load range following a log-normal distribution where $\mu = 1.9$ and $\sigma = 0.1$, which translates to a mean load range of 6.75 kN and a coefficient of variation of 0.1. Figure 6.18 shows (a) a small sample of the loading and (b) a plot of the distribution of load ranges; the results are shown in Figure 6.19.

It can be seen that the linear relationship between inverse crack growth rate and number of cycles as postulated by the FFM still holds with variable amplitude loading that is statistically stationary. In cases where the loading of a component remains statistically stationary and monitoring data is collected over a significant period of time, predictions made using the FFM would still be valid. While individual rate data points may be skewed by load interaction effects, it is believed that with sufficient data points covering a long enough period of time, the overall prediction made by the FFM would remain accurate. This conceptually demonstrates how FFM can be capable of performing remnant life predictions with variable amplitude loading. However, it is believed that more research should be conducted with a wider range of distributions, particularly those of relevance in industrial applications, and loadings of greater variability should be tested to better understand and quantify the capabilities and limitations of using the FFM under variable amplitude loading conditions.

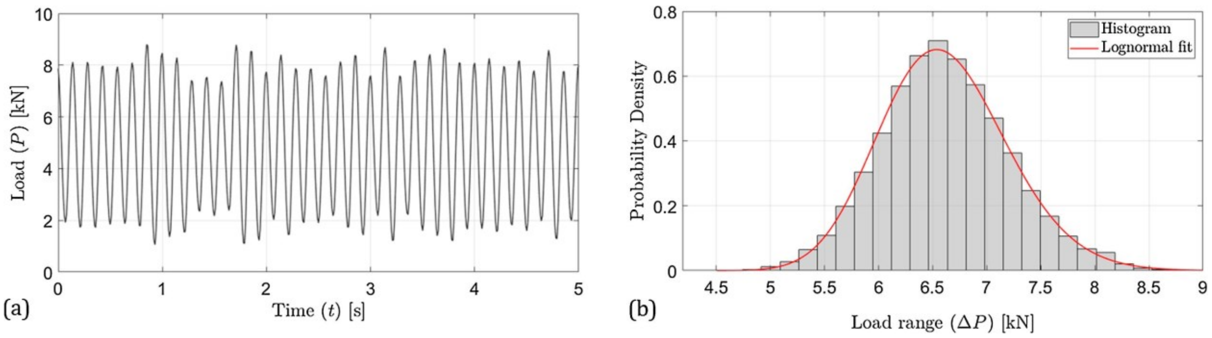

Figure 6.18 Plot of (a) a small sample section of the loading and (b) distribution of load ranges measured from the experiment.

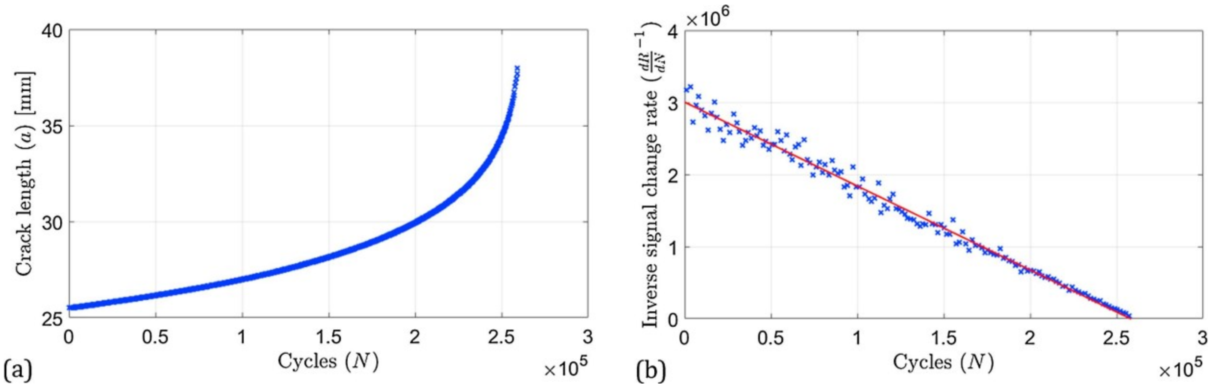

Figure 6.19 Plot of (a) crack length and (b) inverse signal change rate against number of cycles for the random loading test.

6.6 Conclusions

Compared to manual inspections, PIMS can obtain far more frequent and repeatable measurements, consequently enabling the possibility of attaining accurate rate of change measurements. In this chapter, a statistical analysis using experimental fatigue data is performed to compare the rate-based FFM approach and the conventional inspection-based approach in performing remnant fatigue life predictions. Using a combination of analytical methods and Monte Carlo simulations, the progression of the estimated probability distribution of failure cycle with the two approaches is evaluated. The results show that more accurate and confident estimates of remnant life can be made using the FFM approach; with the fatigue data set in this study, the predictions converge to within 10% of the actual failure cycle when 50% of the fatigue life is reached. The FFM approach is based simply on the rate of increase of the damage-related signal without the need for knowledge of the loading or material constants. On the contrary, remnant life predictions made using the conventional approach relies on assumptions of material properties, loading conditions, and having accurate defect size measurements. Each of these parameters would have an associated uncertainty that subsequently aggregates to significant uncertainties in the predicted failure cycle.

A method for using the FFM under non-constant amplitude loading conditions was also developed and validated. A modification made to the FFM can be used to accommodate step changes in loading, but the load change and the sensitivity to load change must be assumed, which may potentially increase the uncertainty. The effect of load interaction on the use of the FFM was also demonstrated using experimental data of a fatigue test with isolated overloads and random variable amplitude loading. Experimental results demonstrate that the FFM remains valid for random variable amplitude loading that is statistically stationary, while isolated overloads can be easily detected and accounted for by restarting the process.

Overall, it is demonstrated that rate measurements obtained from PIMS can be used to provide remnant life predictions with greater accuracy and confidence compared to using the conventional, inspection-based approach. This allows for a more accurate understanding of the structural integrity of components with identified defects, thus aiding the decision on what remedial actions would be appropriate to undertake.

7 Conclusions

7.1 Thesis review

The motivations and aim of the research were introduced in Chapter 1. With an increasing interest in probabilistic structural integrity assessments and the use of permanently installed monitoring systems (PIMS) in various engineering applications, the thesis aims to develop strategies for integrating frequent onload data obtained from PIMS with probabilistic structural integrity methods in order to produce real-time, uncertainty-quantified diagnostics and prognostics for fatigue damage.

In Chapter 2, a review of the current knowledge of the mechanisms and modelling of fatigue damage, as well as the state-of-the-art of NDE and SHM systems was given. This provides the fundamental understanding required to develop models for probabilistic structural integrity assessments and remnant life predictions.

In Chapter 3, a framework for evaluating the detection capabilities for PIMS was developed. The framework builds upon existing methodologies for evaluating the detection capabilities of NDE techniques, which include the ROC analysis and MAPOD studies. The framework makes an important distinction between sources of random and systematic uncertainties, and incorporates statistical distributions of systematic factors when evaluating the confidence in the detection capabilities of PIMS.

In Chapter 4, the spatial aspect of the detection capabilities of PIMS was addressed by building on the framework developed in Chapter 3. Illustrative examples of components with varying degrees of confidence in defect location were combined with PIMS with differing area coverage and sensitivity. A probabilistic structural integrity method was used to inform the likely damage location of the components. This was then combined with a spatial map of sensitivity of the PIMS to quantify and compare the detection capability of each sensor-component combination using key performance parameters such as POD_{exp}, POD_{95} and $a_{90|95}$.

In Chapter 5, a framework was proposed to integrate PIMS data into probabilistic structural integrity assessments of engineering components. With the use of particle filtering methods, frequent measurements from PIMS are used to recursively update the distribution of possible defect size in the component to continuously update the confidence in its fitness-for-service. An illustrative example was used to demonstrate the benefits of implementing PIMS for life-cycle management as opposed to using periodic inspections only.

In Chapter 6, the use of PIMS data to perform remnant life predictions for defective components towards the end of life was investigated. The Failure Forecast Method (FFM) which utilises rate measurements obtained from PIMS to perform remnant life predictions was evaluated and further developed. A statistical analysis using experimental fatigue data was conducted to compare the rate-based FFM approach and the conventional inspection-based approach in performing remnant fatigue life predictions. The results demonstrated that more accurate and confident estimates of remnant life can be made using the rate-based FFM approach. Additionally, a method for using the FFM under non-constant amplitude loading conditions was also developed and validated using experimental fatigue data, thus expanding the use of the FFM for remnant life predictions to more complex loading conditions.

7.2 Summary of main contributions

Throughout the research project, a number of novel academic and industrial contributions were made as summarised below.

Developed a framework for evaluating the detection capabilities of PIMS

Building upon existing methodologies for evaluating the detection capabilities of NDE systems, a framework to systematically evaluate the detection capabilities of PIMS has been proposed. Assessing the detection capabilities is an essential part of qualifying PIMS that will be necessary for their industrial exploitation and use for structural integrity assessments. The proposed framework highlights the importance of separating sources of random and systematic uncertainties and how they should be treated appropriately to evaluate the detection capabilities of PIMS.

Addressed the compromise between area coverage and sensitivity of PIMS

Using the developed framework as described above, a method of evaluating the compromise between area coverage and sensitivity of PIMS is proposed. With the proposed method, key performance parameters to quantify the detection capability for a specific sensor-component combination can be produced. This offers a means of optimising the long-standing problem of compromising between area coverage and sensitivity of PIMS, tailoring the monitoring system to the specific structural integrity concerns of the component. This research demonstrates how important it is to evaluate the spatial sensitivity of PIMS in conjunction with the spatial uncertainty of defect location.

This work has been submitted as a journal paper to the Proceedings of the Royal Society A for review.

Developed a framework to incorporate data from PIMS for structural integrity assessment

A novel approach using particle filtering methods and POD curves of PIMS to recursively update the fitness-for-service of a monitored component has been developed. The approach utilises the ability of PIMS to obtain frequent measurements to continuously update the confidence in structural integrity of the component. Given a sequence of negative detection results from PIMS, the possibility of substantial damage can be constantly filtered out, providing confidence that failure of the monitored component is not imminent. Results from this research demonstrates that this is an effective way of maintaining confidence in the fitness-for-service of engineering components while reducing the number of in-service inspections required.

The established framework will be a useful tool for assessing and promoting the benefits of using PIMS for damage detection in terms of life-cycle management and also life extension. The framework may be applied to evaluate the use of PIMS for a wide range of engineering problems. This will thus aid the implementation of PIMS for appropriate real-life applications.

This work is being prepared for submission as a journal paper.

Evaluated and further extended the use of the Failure Forecast Method for probabilistic remnant fatigue life predictions

A statistical analysis using experimental fatigue data was conducted to demonstrate and quantify the benefits of using the rate-based FFM approach as opposed to the conventional inspection-based approach. A novel technique to apply the FFM in non-constant amplitude loading conditions was also developed and validated. This enables the use of the FFM in more complex loading conditions, thus advancing its potential use in real-life applications. This work has been published as a journal paper [149].

7.3 Suggested future work

There are multiple opportunities for further research work following the findings of this thesis.

Firstly, all example problems used to demonstrate and evaluate the use of PIMS are based on either simulated examples or data from laboratory experiments. While these are useful at earlier stages of development for proof of concept and illustration purposes, evaluation of more realistic engineering applications will be needed to fully recognize the capability of using the proposed strategies to integrate results of PIMS for probabilistic structural integrity assessment. Considerations should be taken when choosing an appropriate application that favours the use of monitoring. As discussed, cases where inspection is ineffective (e.g. limited accessibility or disruptive) and those where defect growth is rapid such that frequent inspections are required would favour the use of PIMS. Examples of this may include applications in nuclear power stations or offshore structures, where access to critical components may be costly and hazardous.

Application in real-life engineering applications would require a combination of computational studies, accelerated experimental tests and field studies to comprehensively evaluate the benefits and practical implications of using PIMS. Careful consideration and optimisation to minimise the amount of experimental and field studies would be required, as these can be costly and time-consuming to conduct.

When using model-assisted methods to evaluate the detection capabilities of PIMS, only a limited number of parameters were investigated in the example problems used. In practise, consideration of many more parameters are likely needed, increasing the dimensionality of the problem and therefore exponentially increasing the computational effort. As a result, advanced methods for more efficient computation would be needed. This include both an efficient evaluation of how various systematic factors affect the detection capabilities of PIMS, and also efficient sampling and resampling techniques when using particle filtering methods to evaluate the confidence in fitness-for-service of monitored components.

The research in this thesis focused on SHM systems that are used for localised damage detection and monitoring. SHM systems that obtain real-time measurements of operating conditions can also be of great value to assessing the structural integrity of engineering components [158]. Development of a framework that incorporates information obtained from SHM systems for both operating conditions monitoring and localised damage detection would be valuable to enable better-informed decisions on developing an optimised strategy for component life-cycle management.

The implementation of cost analysis would also be greatly beneficial in developing a stronger business case for using PIMS for localised defect detection and monitoring. A wide range of research has already been done on methods to evaluate the cost of using SHM systems in various engineering applications [116], [133], [173]. A review and implementation of appropriate methods for cost analysis would further strengthen the justification of adopting PIMS for the management of engineering components and structures.

With regards to the use of the FFM for remnant life predictions, only the evaluation of Stage II Paris crack growth is being studied in this thesis. Further development and evaluation of using the FFM for earlier stages of crack growth can be done to add versatility to the method and enable remnant life predictions to be made at an earlier stage in component life. Continued research on the FFM has been carried out with collaborators in parallel to this thesis, and a draft paper titled “A Bayesian Implementation of the Failure Forecast Method for Fatigue Prediction” has been submitted for review.

Finally, this thesis has only focussed on the problem of fatigue damage. Many of the methodologies developed in this thesis may be adapted to other modes of failure. Further research can be carried out on how the proposed strategies can be used to quantitatively evaluate the benefit of PIMS for detection of damage from other modes of failure.

8 References

[1] R. Weck, 'Failure of Steel Structures: Causes and Remedies', *Proceedings of the Royal Society of London A: Mathematical, Physical and Engineering Sciences*, vol. 285, no. 1400, pp. 3–9, 1965, doi: 10.1098/rspa.1965.0084.

[2] S. J. Findlay and N. D. Harrison, 'Why aircraft fail', *Materials Today*, vol. 5, no. 11, pp. 18–25, Nov. 2002, doi: 10.1016/s1369-7021(02)01138-0.

[3] P. A. Withey, 'Fatigue failure of the de Havilland comet I', *Engineering Failure Analysis*, vol. 4, no. 2, pp. 147–154, Jun. 1997, doi: 10.1016/S1350-6307(97)00005-8.

[4] M. F. Cipière and J. A. Le Duff, 'Thermal Fatigue Experience in French Piping: Influence of Surface Condition and Weld Local Geometry', *Weld World*, vol. 46, no. 1–2, pp. 23–27, Jan. 2002, doi: 10.1007/BF03266362.

[5] R. A. Smith and S. Hillmansen, 'A brief historical overview of the fatigue of railway axles', *Proceedings of the Institution of Mechanical Engineers, Part F: Journal of Rail and Rapid Transit*, vol. 218, no. 4, pp. 267–277, Jul. 2004, doi: 10.1243/0954409043125932.

[6] W. Stinchcomb and K. Reifsnider, 'Fatigue Damage Mechanisms in Composite Materials: A Review', in *Fatigue Mechanisms*, J. Fong, Ed. 100 Barr Harbor Drive, PO Box C700, West Conshohocken, PA 19428-2959: ASTM International, 1979, pp. 762-762–26.

[7] P. P. Milella, *Fatigue and Corrosion in Metals*. Springer-Verlag Mailand, 2013.

[8] E. Santecchia *et al.*, ‘A Review on Fatigue Life Prediction Methods for Metals’, *Advances in Materials Science and Engineering*, vol. 2016, pp. 1–26, 2016, doi: 10.1155/2016/9573524.

[9] K. Rege and H. G. Lemu, ‘A review of fatigue crack propagation modelling techniques using FEM and XFEM’, *IOP Conf. Ser.: Mater. Sci. Eng.*, vol. 276, p. 012027, Dec. 2017, doi: 10.1088/1757-899X/276/1/012027.

[10] C. E. Jaske and W. J. O’Donnell, ‘Fatigue Design Criteria for Pressure Vessel Alloys’, *Journal of Pressure Vessel Technology*, vol. 99, no. 4, pp. 584–592, Nov. 1977, doi: 10.1115/1.3454577.

[11] ‘Fatigue design of offshore steel structures’, DNVGL-RP-C203, Oct. 2011.

[12] O. Chopra and G. L. Stevens, ‘Effect of LWR Water Environments on the Fatigue Life of Reactor Materials: NUREG/CR-6909’, U.S. Nuclear Regulatory Commission, Charlotte, 2018.

[13] BOMEL Limited, ‘Probabilistic methods: uses and abuses in structural integrity’, Health and Safety Executive, Sudbury, HSE RR398/2001, 2001. Accessed: Feb. 20, 2020. [Online].

[14] ‘Probabilistic methods for planning of inspection for fatigue cracks in offshore structures’, DNVGL, Recommended Practice RP-C210, 2015.

[15] M. Martins and R. Marshall, ‘Nuclear Structural Integrity Probabilistic Working Principles’, UK Forum for Engineering Structural Integrity, Apr. 2019. Accessed: Jan. 06, 2020. [Online]. Available: https://www.fesi.org.uk/wp-content/uploads/2019/05/nuclear_SI_probabilistic_working_principlesat.pdf.

[16] ‘Guide to methods for assessing the acceptability of flaws in metallic structures’, British Standards Institution, BS 7910:2019. Accessed: Jan. 09, 2020. [Online]. Available: https://bsol.bsigroup.com/Bibliographic/BibliographicInfoData/000000000030369478.

[17] M. Koçak, ‘European Fitness for Service Network: Final Technical report’, GTC-2001-43049, 2007.

[18] 'Fitness-for-Service', The American Society of Mechanical Engineers, API 579-1/ASME FFS-1. Accessed: Dec. 17, 2019. [Online]. Available: https://www.asme.org/learning-development/find-course/api-579-1-asme-ffs-1-fitness-service.

[19] J. Corcoran, 'Rate-based structural health monitoring using permanently installed sensors', *Proceedings of the Royal Society of London A: Mathematical, Physical and Engineering Sciences*, vol. 473, no. 2205, 2017, doi: 10.1098/rspa.2017.0270.

[20] F. Braithwaite, 'On the Fatigue and consequent Fracture of Metals', *ICE Minutes Proceedings*, vol. 13, no. 1854, pp. 463–474, 1854, doi: 10.1680/imotp.1854.23960.

[21] S. Suresh, *Fatigue of Materials*, 2nd ed. Cambridge University Press, 1998.

[22] H. Mughrabi, 'Microstructural mechanisms of cyclic deformation, fatigue crack initiation and early crack growth', *Phil. Trans. R. Soc. A*, vol. 373, no. 2038, p. 20140132, Mar. 2015, doi: 10.1098/rsta.2014.0132.

[23] R. I. Stephens and H. O. Fuchs, Eds., *Metal fatigue in engineering*, 2nd ed. New York: Wiley, 2001.

[24] L. P. Pook, *Metal Fatigue: What It Is, Why It Matters*, vol. 145. Dordrecht: Springer Netherlands, 2007.

[25] M. Bao-Tong and C. Laird, 'Overview of fatigue behavior in copper single crystals—I. Surface morphology and stage I crack initiation sites for tests at constant strain amplitude', *Acta Metallurgica*, vol. 37, no. 2, pp. 325–336, 1989.

[26] R. Jones, L. Molent, and S. Pitt, 'Similitude and the Paris crack growth law', *International Journal of Fatigue*, vol. 30, no. 10–11, pp. 1873–1880, Oct. 2008, doi: 10.1016/j.ijfatigue.2008.01.016.

[27] A. Fatemi, 'Chapter 6 - Fundamentals of LEFM and Applications to Fatigue Crack Growth', *eFatigue Training and Seminars*. https://www.efatigue.com/training/Chapter_6.pdf.

[28] R. Pippan and A. Hohenwarter, 'Fatigue crack closure: a review of the physical phenomena', *Fatigue Fract Engng Mater Struct*, vol. 40, no. 4, pp. 471–495, Apr. 2017, doi: 10.1111/ffe.12578.

[29] J. C. Newman, ‘The merging of fatigue and fracture mechanics concepts: a historical perspective’, *Progress in Aerospace Sciences*, vol. 34, no. 5–6, pp. 347–390, Jul. 1998, doi: 10.1016/S0376-0421(98)00006-2.

[30] M. Ibrahim and K. Miller, ‘Determination of fatigue crack initiation life’, *Fatigue & Fracture of Engineering Materials & Structures*, vol. 2, no. 4, pp. 351–360, 1979.

[31] C. Wang, D. Wagner, and C. Bathias, ‘Investigations on the Fatigue Crack Propagation Threshold in Very High Cycle Fatigue’, *AMR*, vol. 891–892, pp. 357–362, Mar. 2014, doi: 10.4028/www.scientific.net/AMR.891-892.357.

[32] A. Fernández-Canteli, S. Blasón, B. Pyttel, M. Muniz-Calvente, and E. Castillo, ‘Considerations about the existence or non-existence of the fatigue limit: implications on practical design’, *Int J Fract*, Jan. 2020, doi: 10.1007/s10704-019-00413-6.

[33] H. O. Basquin, ‘The Exponential Law of Endurance Tests’, 1910, vol. 10, pp. 625–630.

[34] L. F. J. Coffin, ‘A Study of the Effects of Cycle Thermal Stresses on a Ductile Material’, Knolls Atomic Power Lab., KAPL-853, Jun. 1953. Accessed: Feb. 12, 2020. [Online]. Available: https://www.osti.gov/biblio/4363016-study-effects-cyclic-thermal-stresses-ductile-metal.

[35] S. S. Manson, ‘Behavior of Materials Under Conditions of Thermal Stress’, Jan. 1954, Accessed: Feb. 12, 2020. [Online]. Available: http://ntrs.nasa.gov/search.jsp?R=19930092197.

[36] J. F. Barbosa, J. A. Correia, R. Freire Júnior, S.-P. Zhu, and A. M. De Jesus, ‘Probabilistic S-N fields based on statistical distributions applied to metallic and composite materials: State of the art’, *Advances in Mechanical Engineering*, vol. 11, no. 8, p. 168781401987039, Aug. 2019, doi: 10.1177/1687814019870395.

[37] P. Paris and F. Erdogan, ‘A Critical Analysis of Crack Propagation Laws’, *Journal of Basic Engineering*, vol. 85, no. 4, pp. 528–533, Dec. 1963, doi: 10.1115/1.3656900.

[38] ‘Fatigue crack growth computer program NASGRO® version 3.0. user manual’, NASA Johnson Space Center, Houston, Texas, JSC-22267B, 1999.

[39] K. B. Broberg, *Cracks and Fracture*. Elsevier, 1999.

[40] J. R. Rice, ‘A Path Independent Integral and the Approximate Analysis of Strain Concentration by Notches and Cracks’, *Journal of Applied Mechanics*, vol. 35, no. 2, pp. 379–386, 1968, doi: 10.1115/1.3601206.

[41] N. E. Dowling and J. A. Begley, ‘Fatigue Crack Growth During Gross Plasticity and the J-Integral’, *Mechanics of Crack Growth*, pp. 82–103, 1976.

[42] M. Miner and others, ‘Cumulative fatigue damage’, *Journal of applied mechanics*, vol. 12, no. 3, pp. A159–A164, 1945.

[43] T. Endo, K. Mitsunaga, K. Takahashi, K. Kobayashi, and M. Matsuishi, ‘Damage Evaluation of Metals for Random or Varying Loading - Three Aspects of Rainflow Method’, in *Proceedings of the 1974 Symposium on the Mechanical Behaviour of Materials*, Japan, 1974, pp. 371–380.

[44] L. L. Schluter, ‘Programmer’s guide for LIFE2’s rainflow counting algorithm’, SAND-90-2260, 6236281, Jan. 1991. doi: 10.2172/6236281.

[45] M. Musallam and C. M. Johnson, ‘An Efficient Implementation of the Rainflow Counting Algorithm for Life Consumption Estimation’, *IEEE Transactions on Reliability*, vol. 61, no. 4, pp. 978–986, Dec. 2012, doi: 10.1109/tr.2012.2221040.

[46] S. Marco and W. Starkey, ‘A concept of fatigue damage’, *Trans. Asme*, vol. 76, no. 4, pp. 627–632, 1954.

[47] A. Fatemi and L. Yang, ‘Cumulative fatigue damage and life prediction theories: a survey of the state of the art for homogeneous materials’, *International Journal of Fatigue*, vol. 20, no. 1, pp. 9–34, Jan. 1998, doi: 10.1016/S0142-1123(97)00081-9.

[48] A. Ray and R. Patankar, ‘Fatigue crack growth under variable-amplitude loading: Part I - Model formulation in state-space setting’, *Applied Mathematical Modelling*, vol. 25, no. 11, pp. 979–994, 2001.

[49] W. Elber, ‘Fatigue crack closure under cyclic tension’, *Engineering Fracture Mechanics*, vol. 2, no. 1, pp. 37–45, 1970.

[50] H. J. Sutherland, ‘Fatiuge Case Study and Loading Spectra for Wind Turbines’, Apr. 1994, pp. 77–87.

[51] W. Elber, ‘Equivalent Constant-Amplitude Concept for Crack Growth Under Spectrum Loading’, in *Fatigue Crack Growth Under Spectrum Loads*, R. Wei and R. Stephens, Eds. 100 Barr Harbor Drive, PO Box C700, West Conshohocken, PA 19428-2959: ASTM International, 1976, pp. 236-236–15.

[52] Y. Xiang and Y. Liu, ‘Equivalent Stress Transformation for Efficient Probabilistic Fatigue-Crack Growth Analysis under Variable Amplitude Loadings’, *J. Aerosp. Eng.*, vol. 29, no. 2, p. 04015052, Mar. 2016, doi: 10.1061/(ASCE)AS.1943-5525.0000489.

[53] ‘Assessment of the integrty of structures containing defects’, British Energy Generation Ltd, R6 rev. 3, May 1999.

[54] S. Butterfield, W. Musial, J. Jonkman, and P. Sclavounos, ‘Engineering Challenges for Floating Offshore Wind Turbines’, presented at the 2005 Copenhagen Offshore Wind Conference, Copenhagen, Denmark, Oct. 2005.

[55] M. H. El Haddad, T. H. Topper, and K. N. Smith, ‘Prediction of non propagating cracks’, *Engineering Fracture Mechanics*, vol. 11, no. 3, pp. 573–584, Jan. 1979, doi: 10.1016/0013-7944(79)90081-X.

[56] J. Maierhofer, H.-P. Gänser, and R. Pippan, ‘Modified Kitagawa–Takahashi diagram accounting for finite notch depths’, *International Journal of Fatigue*, vol. 70, pp. 503–509, Jan. 2015, doi: 10.1016/j.ijfatigue.2014.07.007.

[57] J. Hou, K. Tang, and H. Wu, ‘Short review on multiscale short fatigue crack growth model’, *Mat Design & Process Comms*, vol. 2, no. 1, Feb. 2020, doi: 10.1002/mdp2.93.

[58] Wei Fan and Pizhong Qiao, ‘Vibration-based Damage Identification Methods: A Review and Comparative Study’, *Structural Health Monitoring*, vol. 10, no. 1, pp. 83–111, Jan. 2011, doi: 10.1177/1475921710365419.

[59] R. D. Nayeri, S. F. Masri, R. G. Ghanem, and R. L. Nigbor, ‘A novel approach for the structural identification and monitoring of a full-scale 17-story building based on ambient vibration measurements’, *Smart Materials and Structures*, vol. 17, no. 2, p. 025006, 2008.

[60] C. R. Farrar and D. A. Jauregui, ‘Comparative study of damage identification algorithms applied to a bridge: I. Experiment’, *Smart Materials and Structures*, vol. 7, no. 5, pp. 704–719, Oct. 1998, doi: 10.1088/0964-1726/7/5/013.

[61] P. Cawley, ‘Structural health monitoring: Closing the gap between research and industrial deployment’, *Structural Health Monitoring*, Jan. 2018, doi: 10.1177/1475921717750047.

[62] C. R. Farrar and D. A. Jauregui, ‘Comparative study of damage identification algorithms applied to a bridge: II. Numerical study’, *Smart materials and structures*, vol. 7, no. 5, p. 720, 1998.

[63] P. Cawley, ‘Non-destructive testing of mass produced components by natural frequency measurements’, *Proceedings of the Institution of Mechanical Engineers, Part B: Management and engineering manufacture*, vol. 199, no. 3, pp. 161–168, 1985.

[64] J. C. Radon and A. A. Pollock, ‘Acoustic emissions and energy transfer during crack propagation’, *Engineering Fracture Mechanics*, vol. 4, no. 2, pp. 295–310, Jun. 1972, doi: 10.1016/0013-7944(72)90043-4.

[65] C. B. Scruby, ‘An introduction to acoustic emission’, *Journal of Physics E: Scientific Instruments*, vol. 20, no. 8, pp. 946–953, Aug. 1987, doi: 10.1088/0022-3735/20/8/001.

[66] L. M. Rogers and K. Stambaugh, ‘Application of Acoustic Emission Technology for Health Monitoring of Ship Structures’, Maryland, 2014.

[67] A. F. Almeida, ‘Neural network detection of fatigue crack growth in riveted joints using acoustic emission’, Embry-Riddle Aeronautical University, Daytona Beach, Florida, 1994.

[68] J. Tang, S. Soua, C. Mares, and T.-H. Gan, ‘A Pattern Recognition Approach to Acoustic Emission Data Originating from Fatigue of Wind Turbine Blades’, *Sensors*, vol. 17, no. 11, p. 2507, Nov. 2017, doi: 10.3390/s17112507.

[69] T. J. Fowler, J. A. Blessing, P. J. Conlisk, and T. L. Swanson, ‘The MONPAC System’, *Journal of Acoustic Emission*, vol. 8, no. 3, pp. 1–8, Mar. 1989.

[70] ‘Acoustic Emission Examination of Metallic Vessels During Pressure Testing’, in *Boiler and Pressure Vessel Code*, American Society of Mechanical Engineers, 1988.

[71] A. Ebrahimkhanlou *et al.*, ‘Acoustic emission monitoring of strengthened steel bridges: Inferring the mechanical behavior of post-installed shear connectors’, in *Nondestructive Characterization and Monitoring of Advanced Materials, Aerospace, Civil Infrastructure, and Transportation XIII*, Denver, United States, Apr. 2019, p. 16, doi: 10.1117/12.2514231.

[72] N. I. Tziavos, H. Hemida, S. Dirar, M. Papaelias, N. Metje, and C. Baniotopoulos, ‘Structural health monitoring of grouted connections for offshore wind turbines by means of acoustic emission: An experimental study’, *Renewable Energy*, vol. 147, pp. 130–140, Mar. 2020, doi: 10.1016/j.renene.2019.08.114.

[73] K. M. Holford *et al.*, ‘A new methodology for automating acoustic emission detection of metallic fatigue fractures in highly demanding aerospace environments: An overview’, *Progress in Aerospace Sciences*, vol. 90, pp. 1–11, Apr. 2017, doi: 10.1016/j.paerosci.2016.11.003.

[74] S. Sengupta, A. K. Datta, and P. Topdar, ‘Structural damage localisation by acoustic emission technique: A state of the art review’, *Lat. Am. j. solids struct.*, vol. 12, no. 8, pp. 1565–1582, Aug. 2015, doi: 10.1590/1679-78251722.

[75] F. A. Firestone, ‘The supersonic reflectoscope, an instrument for inspecting the interior of solid parts by means of sound waves’, *The Journal of the Acoustical Society of America*, vol. 17, no. 3, pp. 287–299, 1946.

[76] J. M. Coffey and M. J. Whittle, ‘Non-Destructive Testing: Its Relation to Fracture Mechanics and Component Design’, *Philosophical Transactions of the Royal Society of London. Series A, Mathematical and Physical Sciences*, vol. 299, no. 1446, pp. 93–110, 1981.

[77] R. B. Thompson and D. O. Thompson, ‘Ultrasonics in nondestructive evaluation’, *Proc. IEEE*, vol. 73, no. 12, pp. 1716–1755, 1985, doi: 10.1109/PROC.1985.13367.

[78] M. V. Felice and Z. Fan, ‘Sizing of flaws using ultrasonic bulk wave testing: A review’, *Ultrasonics*, vol. 88, pp. 26–42, Aug. 2018, doi: 10.1016/j.ultras.2018.03.003.

[79] F. B. Cegla, P. Cawley, J. Allin, and J. Davies, ‘High-temperature (>500°c) wall thickness monitoring using dry-coupled ultrasonic waveguide transducers’, *IEEE Trans. Ultrason., Ferroelect., Freq. Contr.*, vol. 58, no. 1, pp. 156–167, Jan. 2011, doi: 10.1109/TUFFC.2011.1782.

[80] ‘Rosemount Wireless Corrosion & Erosion Monitoring’, *Emerson*. https://www.emerson.com/en-us/automation/measurement-instrumentation/corrosion-erosion-monitoring/about-rosemount-wireless-corrosion-erosion-monitoring.

[81] M. J. S. Lowe, ‘Guided Wave Testing’, in *Nondestructive Evaluation of Materials*, vol. 17, A. Ahmad and L. J. Bond, Eds. ASM International, 2018.

[82] ‘Plates and Shells’, *Guidedwave*. http://www.gwultrasonics.com/knowledge/plateshell/.

[83] S. Mariani, ‘Non-contact Ultrasonic Guided Wave Inspection of Rails : Next Generation Approach’, University of California, San Diego, 2015.

[84] M. J. S. Lowe, D. N. Alleyne, and P. Cawley, ‘Defect detection in pipes using guided waves’, *Ultrasonics*, vol. 36, no. 1–5, pp. 147–154, Feb. 1998, doi: 10.1016/S0041-624X(97)00038-3.

[85] P. Wilcox, M. Lowe, and P. Cawley, ‘Omnidirectional guided wave inspection of large metallic plate structures using an EMAT array’, *IEEE Trans. Ultrason., Ferroelect., Freq. Contr.*, vol. 52, no. 4, pp. 653–665, Apr. 2005, doi: 10.1109/TUFFC.2005.1428048.

[86] M. Mitra and S. Gopalakrishnan, ‘Guided wave based structural health monitoring: A review’, *Smart Mater. Struct.*, vol. 25, no. 5, p. 053001, May 2016, doi: 10.1088/0964-1726/25/5/053001.

[87] C. A. Chua, P. Cawley, and P. B. Nagy, ‘Scattering of fundamental shear guided waves from a surface-breaking crack in plate-like structures’, *IEEE Transactions on Ultrasonics, Ferroelectrics, and Frequency Control*, pp. 1–11, 2019, doi: 10.1109/TUFFC.2019.2932227.

[88] A. Hikata, B. B. Chick, and C. Elbaum, ‘Effect of Dislocations on Finite Amplitude Ultrasonic Waves in Aluminium’, *Appl. Phys. Lett.*, vol. 3, no. 11, pp. 195–197, Dec. 1963, doi: 10.1063/1.1753845.

[89] P. B. Nagy, ‘Fatigue damage assessment by nonlinear ultrasonic materials characterization’, *Ultrasonics*, vol. 36, no. 1–5, pp. 375–381, Feb. 1998, doi: 10.1016/S0041-624X(97)00040-1.

[90] J. H. Cantrell and W. T. Yost, ‘Nonlinear ultrasonic characterization of fatigue microstructures’, *International Journal of Fatigue*, vol. 23, pp. 487–490, 2001, doi: 10.1016/S0142-1123(01)00162-1.

[91] ‘Standard Test Method for Measurement of Fatigue Crack Growth Rates’, ASTM International, ASTM E647-15, 2016.

[92] ‘BiNDT: Potential drop flaw detection and sizing’, *BiNDT*, 2013. http://www.bindt.org/What-is-NDT/Potential-drop-flaw-detection-and-sizing/.

[93] J. Corcoran, ‘Creep Monitoring using Permanently Installed Potential Drop Sensors’, PhD Thesis, Imperial College London, 2015.

[94] J. Corcoran, P. B. Nagy, and P. Cawley, ‘Monitoring creep damage at a weld using a potential drop technique’, *International Journal of Pressure Vessels and Piping*, vol. 153, pp. 15–25, Jun. 2017, doi: 10.1016/j.ijpvp.2017.05.001.

[95] K. M. Tarnowski, ‘Measuring Crack Initiation and Growth in the Presence of Large Strains using the Potential Drop Technique’, PhD Thesis, Imperial College London, 2016.

[96] E. Glaessgen and D. Stargel, ‘The Digital Twin Paradigm for Future NASA and U.S. Air Force Vehicles’, Honolulu, Hawaii, Apr. 2012, doi: 10.2514/6.2012-1818.

[97] J. Corcoran and P. B. Nagy, ‘Compensation of the Skin Effect in Low-Frequency Potential Drop Measurements’, *J Nondestruct Eval*, vol. 35, no. 4, p. 58, Dec. 2016, doi: 10.1007/s10921-016-0374-4.

[98] G. A. Georgiou, ‘RR454: Probability of Detection (PoD) curves - Derivation, applications and limitations’, Health and Safety Executive UK, London, 2006.

[99] 'MIL-HDBK-1823A Nondestructive Evaluation System Reliability Assessment', United States Department of Defense, 2009.

[100] A. J. Croxford, J. Moll, P. D. Wilcox, and J. E. Michaels, 'Efficient temperature compensation strategies for guided wave structural health monitoring', *Ultrasonics*, vol. 50, no. 4–5, pp. 517–528, Apr. 2010, doi: 10.1016/j.ultras.2009.11.002.

[101] M. Salmanpour, Z. Sharif Khodaei, and M. Aliabadi, 'Guided wave temperature correction methods in structural health monitoring', *Journal of Intelligent Material Systems and Structures*, vol. 28, no. 5, pp. 604–618, Mar. 2017, doi: 10.1177/1045389X16651155.

[102] V. A. Attarian, F. B. Cegla, and P. Cawley, 'Long-term stability of guided wave structural health monitoring using distributed adhesively bonded piezoelectric transducers', *Structural Health Monitoring*, vol. 13, no. 3, pp. 265–280, May 2014, doi: 10.1177/1475921714522842.

[103] S. Mariani, S. Heinlein, and P. Cawley, 'Location specific temperature compensation of guided wave signals in structural health monitoring', *IEEE Trans Ultrason Ferroelectr Freq Control*, Sep. 2019, doi: 10.1109/TUFFC.2019.2940451.

[104] M. S. H. Leung, J. Corcoran, and P. Cawley, 'A Structural Integrity Informed Approach to Evaluating the Probability of Detection obtained with Permanently-Installed Sensors', presented at the 46th Annual Review of Progress in Quantitative Nondestructive Evaluation, Portland, OR, Jul. 2019.

[105] H. Wirdelius and E. Oesterberg, 'Study of defect characteristics essential for NDT testing methods ET, UT and RT', Swedish Nuclear Power Inspectorate, 2000.

[106] J. R. Pettit, A. E. Walker, and L. M. J. S, 'Improved Detection of Rough Defects for Ultrasonic Nondestructive Evaluation Inspections Based on Finite Element Modeling of Elastic Wave Scattering', *IEEE Transactions on Ultrasonics, Ferroelectrics, and Frequency Control*, vol. 62, pp. 1797–1808, 2015.

[107] A. Gajdacsi, 'High accuracy ultrasonic degradation monitoring', PhD Thesis, 2015.

[108] J. Corcoran, C. M. Davies, P. Cawley, and P. B. Nagy, 'A quasi-DC Potential Drop Measurement System for Materials Testing', *IEEE Transactions on Instrumentation and Measurement*, 2019.

[109] P. Calmon, 'The use of simulation in POD curves estimation: An overview of the IIW best practices proposal', Munich, 2016.

[110] F. Foucher, R. Fernandez, S. Leberre, and P. Calmon, 'New tools in CIVA for Model Assisted Probability of Detection (MAPOD) to support NDE reliability studies', Bridgeton, 2018.

[111] D. Heiserman, 'Arc Welding Positions', *Fundamentals of Professional Welding*. .

[112] X. Du, L. Leifsson, R. Grandin, W. Meeker, R. Roberts, and J. Song, 'Model-assisted probability of detection of flaws in aluminum blocks using polynomial chaos expansions', Provo, Utah, USA, 2018, p. 230010, doi: 10.1063/1.5031657.

[113] H.-P. Wan, W.-X. Ren, and M. D. Todd, 'Arbitrary polynomial chaos expansion method for uncertainty quantification and global sensitivity analysis in structural dynamics', *Mechanical Systems and Signal Processing*, vol. 142, p. 106732, Aug. 2020, doi: 10.1016/j.ymssp.2020.106732.

[114] R. Howard and F. Cegla, 'Detectability of corrosion damage with circumferential guided waves in reflection and transmission', *NDT & E International*, vol. 91, pp. 108–119, 2017, doi: https://doi.org/10.1016/j.ndteint.2017.07.004.

[115] R. Soman, P. Kudela, K. Balasubramaniam, S. K. Singh, and P. Malinowski, 'A Study of Sensor Placement Optimization Problem for Guided Wave-Based Damage Detection', *Sensors*, vol. 19, no. 8, p. 1856, 2019, doi: 10.3390/s19081856.

[116] E. B. Flynn and M. D. Todd, 'Optimal Placement of Piezoelectric Actuators and Sensors for Detecting Damage in Plate Structures', *Journal of Intelligent Material Systems and Structures*, vol. 21, no. 3, pp. 265–274, Feb. 2010, doi: 10.1177/1045389X09338080.

[117] I. Yalda, F. J. Margetan, and R. B. Thompson, 'Use of Rician distributions to predict the distributions of ultrasonic flaw signals in the presence of backscattered noise', in *Review of Progress in Quantitative Nondestructive Evaluation*, Springer, 1998, pp. 105–112.

[118] J. A. Ogilvy, ‘Model for predicting ultrasonic pulse-echo probability of detection’, *NDT & E International*, vol. 26, pp. 19–29, 1993.

[119] J. Daintith, E. Wright, and Oxford University Press, Eds., *A dictionary of computing*, 6th ed. Oxford ; New York: Oxford University Press, 2008.

[120] S. Tanaka, M. Ichikawa, and S. Akita, ‘A Probabilistic Investigation of Fatigue Life and Cumulative Cycle Ratio’, *Engineering Fracture Mechanics*, vol. 20, pp. 501–513, 1984.

[121] Doosan Babcock Energy Limited, ‘RR659: Evaluation of the effectiveness of non-destructive testing screening methods for in-service inspection’, UK Health and Safety Executive, Renfrew, 2009.

[122] P. Cawley, F. Cegla, and M. Stone, ‘Corrosion Monitoring Strategies—Choice Between Area and Point Measurements’, *J Nondestruct Eval*, vol. 32, no. 2, pp. 156–163, Jun. 2013, doi: 10.1007/s10921-012-0168-2.

[123] W. Weibull, *A Statistical Theory of the Strength of Materials*. Stockholm: Generalstabens Litografiska Anstalts Förlag, 1939.

[124] C. Przybilla, A. Fernandez-Canteli, and E. Castillo, ‘Deriving the primary cumulative distribution function of fracture stress for brittle materials from 3- and 4-point bending tests’, *Journal of the European Ceramic Society*, vol. 31, pp. 451–460, 2011.

[125] M. Muniz-Calvente, A. M. P. Jesus, J. A. F. O. Correia, and A. Fernandez-Canteli, ‘A methodology for probabilistic prediction of fatigue crack initiation taking into account the scale effect’, *Engineering Fracture Mechanics*, vol. 185, pp. 101–113, 2017.

[126] A. Wormsen, B. Sjodin, G. Harkegard, and A. Fjeldstad, ‘Non-local stress approach for fatigue assessment based on weakest-link theory and statistics of extremes’, *Fatigue & Fracture of Engineering Materials & Structures*, vol. 3, pp. 1214–1227, 2007.

[127] P. Maincon, ‘FEM post-processor for fatigue analysis: P-FAT, SN analysis and Crack growth analysis’, *SINTEF*, [Online]. Available: https://www.sintef.no/en/software/fem-post-processor-for-fatigue-analysis/.

[128] O. H. Basqiun, ‘The Exponential Law of Endurance Tests’, *American Society of Testing Materials*, vol. 10, pp. 625–630, 1910.

[129] S. Suresh, ‘Strain-based approach to total life’, in *Fatigue of Materials*, Cambridge: Cambridge University Press, 1998, p. 257.

[130] ‘E606/E606M-12 Standard Test Method for Strain-Controlled Fatigue Testing’, ASTM International, West Conshohocken, PA, 2012.

[131] N. Gagunashvili, ‘Weighted Histogram’, SFT CERN, 2017.

[132] H. Cothron, ‘Update on the Tools for Integrity Assessment Project - 1014756’, Electric Power Research Institute, California, 2007.

[133] E. Medina, J. Aldrin, J. Knopp, and D. Allwine, ‘Value Assessment Tools For Hybrid NDE-SHM Life Management Strategies (Preprint)’, 2006.

[134] P. Mudge, A. Haig, K. Thornicroft, and P. Jackson, ‘Non-Invasive monitoring strategies for engineering structures using guided waves’, presented at the 7th Middle East Nondestructive Testing Conference & Exhibition, Bahrain, Sep. 2015.

[135] C. A. Chua and P. Cawley, ‘Crack growth monitoring using fundamental shear horizontal guided waves’, *Structural Health Monitoring*, p. 147592171988233, Oct. 2019, doi: 10.1177/1475921719882330.

[136] T. Shibata and T. Takeyama, ‘Pitting corrosion as a stochastic process’, *Nature*, vol. 260, no. 5549, pp. 315–316, Mar. 1976, doi: 10.1038/260315a0.

[137] D. A. Virkler, B. M. Hillberry, and P. K. Goel, ‘The Statistical Nature of Fatigue Crack Propagation’, *J. Eng. Mater. Technol*, vol. 101, no. 2, pp. 148–153, Apr. 1979, doi: 10.1115/1.3443666.

[138] N. Roy, R. N. Ghosh, and S. C. Bose, ‘A stochastic model for evolution of creep damage in engineering materials’, *Transactions of the Indian Institute of Metals*, vol. 63, no. 2, pp. 665–669, Apr. 2010, doi: 10.1007/s12666-010-0101-2.

[139] Y. Appalanaidu, Y. Vyas, and S. Gupta, ‘Stochastic Creep Damage Growth Due to Random Thermal Fluctuations Using Continuum Damage Mechanics’, *Procedia Engineering*, vol. 55, pp. 805–811, 2013, doi: 10.1016/j.proeng.2013.03.335.

[140] M. Gobbato, J. P. Conte, and J. B. Kosmatka, ‘Statistical Performance Assessment of an NDE-Based SHM-DP Methodology for the Remaining Fatigue Life Prediction of

Monitored Structural Components and Systems', *Proc. IEEE*, vol. 104, no. 8, pp. 1575–1588, Aug. 2016, doi: 10.1109/JPROC.2015.2512979.

[141] P. Miedlar, 'Summary of Stress Intensity Factor Information', in *AFGROW Handbook for Damage Tolerant Design*, AFGROW, 2002.

[142] 'Eddy Current Testing (ECT)', *Eddyfi Technologies*. https://www.eddyfi.com/en/technology/eddy-current-testing-ect.

[143] E. Mohseni, H. Habibzadeh Boukani, D. Ramos França, and M. Viens, 'A Study of the Automated Eddy Current Detection of Cracks in Steel Plates', *J Nondestruct Eval*, vol. 39, no. 1, p. 6, Mar. 2020, doi: 10.1007/s10921-019-0647-9.

[144] B. Herdovics and F. Cegla, 'Long-term stability of guided wave electromagnetic acoustic transducer systems', *Structural Health Monitoring*, vol. 19, no. 1, pp. 3–11, Oct. 2018, doi: 10.1177/1475921718805733.

[145] M. S. Arulampalam, S. Maskell, N. Gordon, and T. Clapp, 'A tutorial on particle filters for online nonlinear/non-Gaussian Bayesian tracking', *IEEE Transactions on Signal Processing*, vol. 50, no. 2, pp. 174–188, Feb. 2002, doi: 10.1109/78.978374.

[146] F. Cadini, E. Zio, and D. Avram, 'Monte Carlo-based filtering for fatigue crack growth estimation', *Probabilistic Engineering Mechanics*, vol. 24, no. 3, pp. 367–373, Jul. 2009, doi: 10.1016/j.probengmech.2008.10.002.

[147] M. Corbetta, C. Sbarufatti, M. Giglio, and M. D. Todd, 'Optimization of nonlinear, non-Gaussian Bayesian filtering for diagnosis and prognosis of monotonic degradation processes', *Mechanical Systems and Signal Processing*, vol. 104, pp. 305–322, May 2018, doi: 10.1016/j.ymssp.2017.11.012.

[148] P. M. Karve, Y. Guo, B. Kapusuzoglu, S. Mahadevan, and M. A. Haile, 'Digital twin approach for damage-tolerant mission planning under uncertainty', *Engineering Fracture Mechanics*, vol. 225, p. 106766, Feb. 2020, doi: 10.1016/j.engfracmech.2019.106766.

[149] M. S. H. Leung, J. Corcoran, P. Cawley, and M. D. Todd, 'Evaluating the use of rate-based monitoring for improved fatigue remnant life predictions', *International Journal of Fatigue*, vol. 120, pp. 162–174, Mar. 2019, doi: 10.1016/j.ijfatigue.2018.11.012.

[150] W. S. Johnson, 'The history, logic and uses of the Equivalent Initial Flaw Size approach to total fatigue life prediction', *Procedia Engineering*, vol. 2, no. 1, pp. 47–58, Apr. 2010, doi: 10.1016/j.proeng.2010.03.005.

[151] M. D. McKay, R. J. Beckman, and W. J. Conover, 'A Comparison of Three Methods for Selecting Values of Input Variables in the Analysis of Output from a Computer Code', *Technometrics*, vol. 21, no. 2, p. 239, May 1979, doi: 10.2307/1268522.

[152] P. Kozierski, M. Lis, and J. Zietkiewicz, 'Resampling in Particle Filtering - Comparison'. Poznań Society of Friends of Learning, 2013.

[153] T. Li, M. Bolic, and P. M. Djuric, 'Resampling Methods for Particle Filtering: Classification, implementation, and strategies', *IEEE Signal Process. Mag.*, vol. 32, no. 3, pp. 70–86, May 2015, doi: 10.1109/MSP.2014.2330626.

[154] T. Li, T. P. Sattar, and S. Sun, 'Deterministic resampling: Unbiased sampling to avoid sample impoverishment in particle filters', *Signal Processing*, vol. 92, no. 7, pp. 1637–1645, Jul. 2012, doi: 10.1016/j.sigpro.2011.12.019.

[155] J. Stutzmann, L. Ziegler, and M. Muskulus, 'Fatigue Crack Detection for Lifetime Extension of Monopile-based Offshore Wind Turbines', *Energy Procedia*, vol. 137, pp. 143–151, Oct. 2017, doi: 10.1016/j.egypro.2017.10.341.

[156] J. Chen, S. Yuan, H. Wang, and W. Yang, 'On particle filter improvements for on-line crack growth prognosis with guided wave monitoring', *Smart Mater. Struct.*, vol. 28, no. 3, p. 035011, Mar. 2019, doi: 10.1088/1361-665X/aaf93e.

[157] E. B. Flynn and M. D. Todd, 'A Bayesian approach to optimal sensor placement for structural health monitoring with application to active sensing', *Mechanical Systems and Signal Processing*, vol. 24, no. 4, pp. 891–903, May 2010, doi: 10.1016/j.ymssp.2009.09.003.

[158] J. Rudolph and S. Bergholz, 'The AREVA Integrated and Sustainable Concept of Fatigue Design, Monitoring and Re-Assessment', in *Volume 1: Codes and Standards*, Chicago, Illinois, USA, Jan. 2008, pp. 115–125, doi: 10.1115/PVP2008-61897.

[159] S. Jiao, L. Cheng, X. Li, P. Li, and H. Ding, ‘Monitoring fatigue cracks of a metal structure using an eddy current sensor’, *J Wireless Com Network*, vol. 2016, no. 1, p. 188, Dec. 2016, doi: 10.1186/s13638-016-0689-y.

[160] B. Voight, ‘A Relation to Describe Rate-Dependent Material Failure’, *Science*, vol. 243, no. 4888, pp. 200–203, 1989, doi: 10.1126/science.243.4888.200.

[161] A. Boué, P. Lesage, G. Cortés, B. Valette, and G. Reyes-Dávila, ‘Real-time eruption forecasting using the material Failure Forecast Method with a Bayesian approach’, *J. Geophys. Res. Solid Earth*, vol. 120, no. 4, pp. 2143–2161, Apr. 2015, doi: 10.1002/2014JB011637.

[162] K. Ortiz and A. S. Kiremidjian, ‘Stochastic modeling of fatigue crack growth’, *Engineering Fracture Mechanics*, vol. 29, no. 3, pp. 317–334, Jan. 1988, doi: 10.1016/0013-7944(88)90020-3.

[163] N. A. Zentuti, J. D. Booker, R. A. W. Bradford, and C. E. Truman, ‘A review of probabilistic techniques: towards developing a probabilistic lifetime methodology in the creep regime’, *Materials at High Temperatures*, vol. 34, no. 5–6, pp. 333–341, Sep. 2017, doi: 10.1080/09603409.2017.1371933.

[164] M. Moles, L. Wesley, and T. Sinclair, ‘Accurate Defect Sizing using Phased Array and Signal Processing’, 2009.

[165] ‘Information for the Procurement and Conduct of NDT, Part 4: Ultrasonic Sizing Errors and Their Implication for Defect Assessment’, Health and Safety Executive, \, 2008.

[166] B. Voight, ‘A method for prediction of volcanic eruptions’, *Nature*, vol. 332, pp. 125–130, 1988, doi: 10.1038/332125a0.

[167] M. D. Todd, M. Leung, and J. Corcoran, ‘A Probability Density Function for Uncertainty Quantification in the Failure Forecast Method’, Jul. 2018.

[168] R. G. Forman, V. E. Kearney, and R. M. Engle, ‘Numerical Analysis of Crack Propagation in Cyclic-Loaded Structures’, *Journal of Basic Engineering*, vol. 89, no. 3, pp. 459–463, Sep. 1967, doi: 10.1115/1.3609637.

[169] O. E. Wheeler, ‘Spectrum Loading and Crack Growth’, *Journal of Basic Engineering*, vol. 94, no. 1, p. 181, 1972, doi: 10.1115/1.3425362.

[170] J. Willenborg, R. M. Engle, and H. A. Wood, ‘A Crack Growth Retardation Model Using an Effective Stress Concept’, Air Force Flight Dynamics Laboratory, AFFDL-TM-71-1-FBR, 1971.

[171] L. Ziegler, S. Schafhirt, M. Scheu, and M. Muskulus, ‘Effect of Load Sequence and Weather Seasonality on Fatigue Crack Growth for Monopile-based Offshore Wind Turbines’, *Energy Procedia*, vol. 94, pp. 115–123, Sep. 2016, doi: 10.1016/j.egypro.2016.09.204.

[172] W. J. Mills and R. W. Hertzberg, ‘Load interaction effects on fatigue crack propagation in 2024-T3 aluminum alloy’, *Engineering Fracture Mechanics*, vol. 8, no. 4, pp. 657–667, Jan. 1976, doi: 10.1016/0013-7944(76)90039-4.

[173] S. Thöns, *Workshop on Quantifying the Value of Structural Health Monitoring*. European Cooperation in Science and Technology, 2015.

[174] P. H. Wirsching, ‘The Application of Probabilistic Design Theory to High Temeprature Low Cycle Fatigue: NASA CR-165488’, NASA Lewis Research Centre, Cleveland, 1981.

[175] W. Weibull, ‘A Statistical Distribution Function of Wide Applicability’, *Journal of Applied Mechanics*, pp. 293–297, 1951.

[176] H. Li, D. Wen, Z. Lu, Y. Wang, and F. Deng, ‘Identifying the Probability Distribution of Fatigue Life Using the Maximum Entropy Principle’, *Entropy*, vol. 111, pp. 1–19, 2016.

9 Appendix A: The weakest-link theory for fatigue damage

The underlying concept of the weakest-link theory is that the larger the component, the more potential there is for the component to contain flaws or aberrant material where damage are likely to initiate.

Consider a reference specimen of standardized dimension with surface area A_{ref}. The probability of survival (no life-limiting damage initiating) of the reference specimen is $P_{s,ref}$. By dividing the surface of the reference specimen into elements of equal surface area, $A(i)$, $P_{s,ref}$ can be expressed as the probability of all the individual elements on the reference specimen surviving (no life-limiting damage initiating on any of the elements), $P_s(i)$. In mathematical terms,

$$P_{s,ref} = P_s(1) \times P_s(2) \times \ldots \times P_s(m_i) = \prod_{i=1}^{m_i} P_{s,i} = \left(P_{s,i}\right)^{\frac{A_{ref}}{A(i)}}, \qquad m_i = \frac{A_{ref}}{A(i)} \qquad \text{Eq. 9.1}$$

Rearranging gives,

$$P_s(i) = \left(P_{s,ref}\right)^{\frac{1}{m_i}} \qquad \text{Eq. 9.2}$$

The probability of failure (a life-limiting damage initiating) of element i, $P_{f,i}$, can therefore be defined as,

$$P_f(i) = 1 - P_s(i) = 1 - \left(P_{s,ref}\right)^{\frac{1}{m_i}} = 1 - \left(1 - P_{f,ref}\right)^{\frac{1}{m_i}} \qquad \text{Eq. 9.3}$$

The significance of this equation is that it can be used to evaluate the probability of failure of an arbitrary surface using the results of a reference specimen. For instance, results from laboratory tests using standardized specimens can be applied to any component with stress field obtained from finite element results, and $A(i)$ becomes the surface area of an element. This comes with the additional benefit of evaluating how likely is a life-limiting damage going to initiate for each of the element on the component.

For fatigue damage, the probability of failure is mainly dependent on the equivalent stress amplitude corrected for mean stress effects, S_a', and the number of loading cycles, N. As discussed in Section 2.1.2.1, the expected number of cycles to failure, $\overline{N_f}$, is given by the Basquin law [128]. Rearranging Eq. 2.3 and incorporating the mean stress effect in loading stress amplitude gives,

$$\overline{N_f} = \exp[C_1 - C_2 \ln(S_a')] \qquad \text{Eq. 9.4}$$

where C_1 and C_2 are material constants that are a function of the fatigue strength coefficient and exponent of the material as shown in Eq. 2.3. There is inevitably uncertainty in the actual cycles to failure, N_f, of a component. Assuming that N_f is lognormally distributed, we can express Eq. 9.4 as,

$$N_f = \exp[C_1 - C_2 \ln(S_a') + z\sigma] \qquad \text{Eq. 9.5}$$

where $z \sim Normal(0,1)$ and σ is the shape parameter of the lognormal distribution. There is a range of literature discussing the most appropriate distribution type for fatigue damage, such as lognormal [174], Weibull [175], or generalised extreme value distribution [176]. A lognormal distribution is used here as this is common practice and most applicable in engineering design with readily available data for common materials in standards [12], [174].

To evaluate the probability of failure for any given combination of S_a' and number of loading cycles, N, Eq. 9.5 can be rearranged to give,

$$z = \frac{1}{\sigma}[\ln(N) - C_1 + C_2 \ln(S_a')] \qquad \text{Eq. 9.6}$$

Here, z can be seen as a generalised parameter which follows the standard normal distribution that define the contour lines of equal probability of failure in the S_a'-N space as illustrated in Figure 9.1. The cumulative probability of failure of a standard specimen, $P_{f,ref}$, is thus simply the cumulative distribution function of the standard normal distribution, denoted as $\Phi(z)$. Substituting this into Eq. 9.6 gives,

$$P_f(i) = 1 - \big(1 - \Phi(z)\big)^{\frac{1}{m_i}} \qquad \text{Eq. 9.7}$$

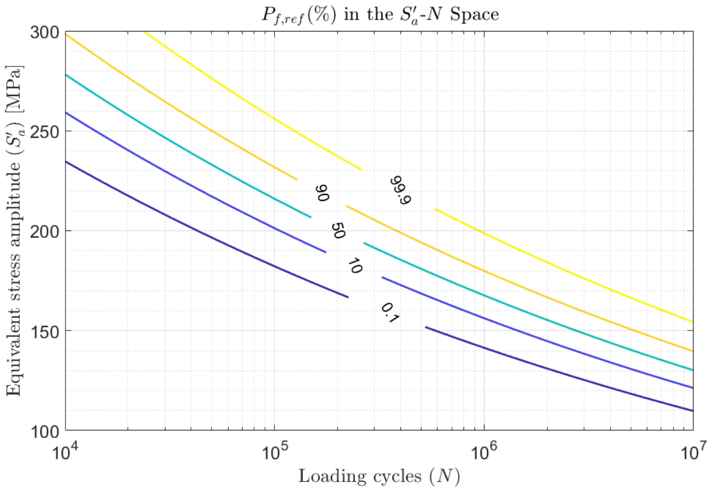

Figure 9.1 Plot of S_a' against N with selected contour lines of probability of failure, $P_{f,ref}$.

With this, the probability of failure of an arbitrary surface, i, can be evaluated with Eq. 9.7 if the following is known:

- Area of the surface, $A(i)$
- Material constants, C_1 and C_2 for Eq. 9.4 evaluated with a specimen of standardized geometry with surface area, A_{ref}
- Equivalent loading amplitude experienced by the surface, S_a'
- Number of loading cycles experienced by the surface, N

Several assumptions are made when applying the weakest-link theory to fatigue damage in this analysis. Firstly, as stated above, it is assumed that fatigue damage manifests at the surface of a component. This is a valid assumption if no significant voids are present within the material. This assumption is especially valid in the case of bending fatigue as the maximum stress amplitude experienced by the beam is at its bottom surface. In the case of other damage mechanisms, the volume of an element instead of surface area is usually considered [124]. It is also assumed that life-limiting damage initiating from the component does not interact. This is a valid assumption for high-cycle fatigue where the number of life-limiting damage is small and thus sparsely distributed [126].